Exploring the Threefold Invisible Universe:

Low-Frequency Spectropolarimetry with LOFAR as a Probe of Galactic Magnetism

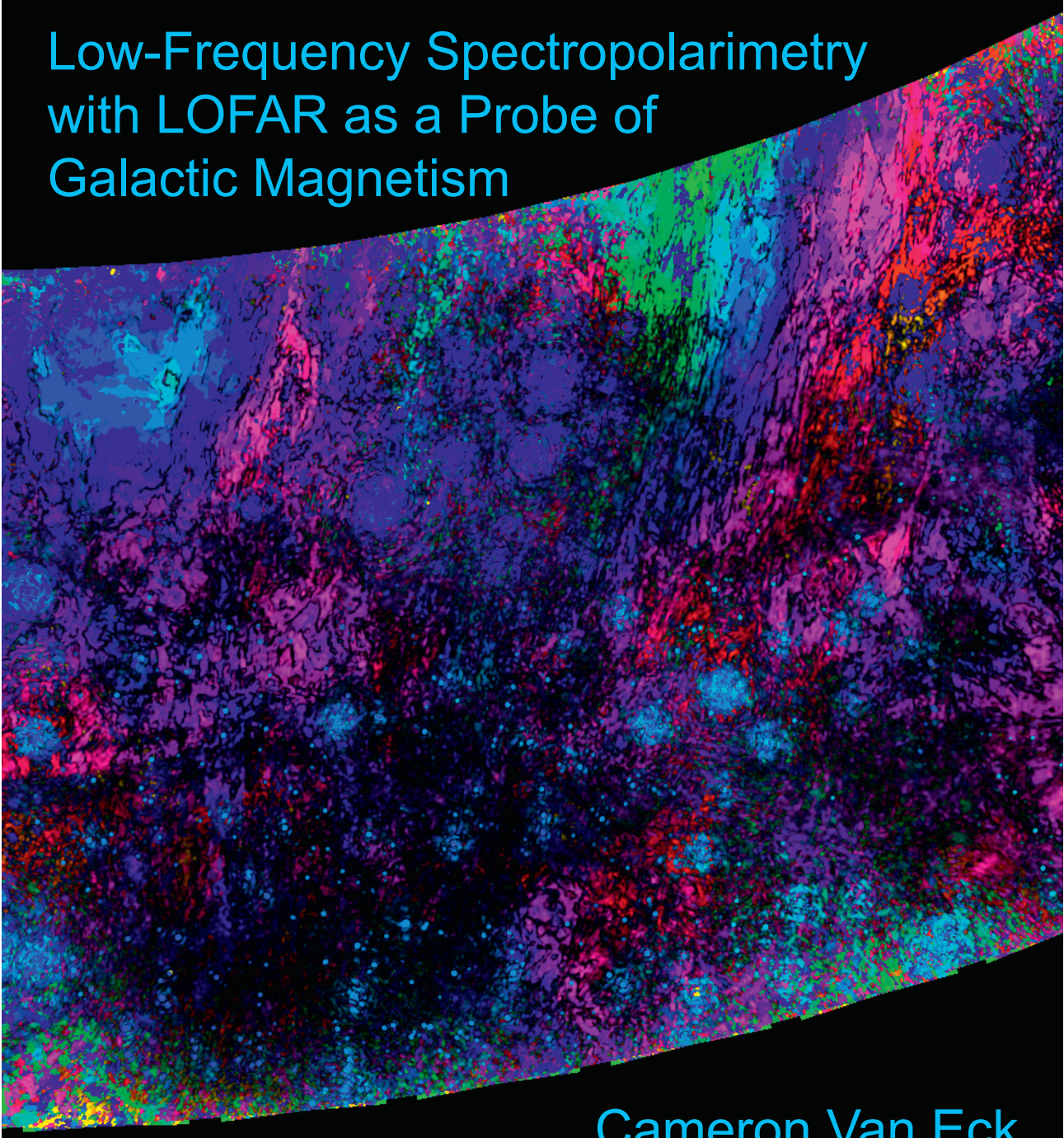

Cameron Van Eck

Exploring the Threefold Invisible Universe: Low-Frequency Spectropolarimetry with LOFAR as a Probe of Galactic Magnetism

Proefschrift

ter verkrijging van de graad van doctor
aan de Radboud Universiteit Nijmegen
op gezag van de rector magnificus prof. dr. J.H.J.M. van Krieken,
volgens besluit van het college van decanen
in het openbaar te verdedigen op
maandag 9 oktober 2017
om 12.30 uur precies

door

Cameron Lee Van Eck

geboren op 14 september 1987
te Lethbridge, Alberta, Canada

Promotoren:	Prof. dr. H.D.E. Falcke	
Copromotoren:	Dr. M. Haverkorn	
Manuscriptcommissie:	Prof. dr. N. de Groot	
	Prof dr. A. Achterberg	
	Dr. A. Fletcher	Newcastle University, Verenigd Koninkrijk
	Dr. G.H. Janssen	ASTRON, Dwingeloo
	Prof dr. R.-J. Dettmar	Ruhr-Universität Bochum, Duitsland

Exploring the Threefold Invisible Universe: Low-Frequency Spectropolarimetry with LOFAR as a Probe of Galactic Magnetism
Thesis, Radboud University Nijmegen
Illustrated; with bibliographic information and Dutch summary

ISBN: 978-94-028-0717-2

"The argument in the past has frequently been a process of elimination: one observed certain phenomena, and one investigated what part of the phenomena could be explained; then the unexplained part was taken to show the effects of the magnetic field. It is clear in this case that, the larger one's ignorance, the stronger the magnetic field."

— L. Woltjer, 1967.

Contents

Chapter 1

Introduction

For most of recorded history, astronomy was limited to observing what we could see in the sky with our eyes. However, with the scientific and technological advances of the past two centuries we now know that the light our eyes can see is only a small sliver of the full electromagnetic spectrum. Even though our eyes are sensitive to light spanning less than a factor of two in frequency, we now have the capability to observe the sky at frequencies (energies) spanning 25 orders of magnitude, from 3.5 kHz (10^{-11} eV) radio waves [Gurnett et al., 2004] to 10^{28} Hz (80 TeV) gamma rays [Aharonian et al., 2004]. We also have the capability to use non-electromagnetic tracers including gravitational waves, neutrinos, and cosmic rays, all of which are likewise undetectable to human senses. It is now the case that the majority of astronomy is done by looking at signals that are invisible to the human eye.

The 'threefold invisible universe' in the title of this thesis refers to the three physical phenomena that are critical to the research, each of which is undetectable, without technological intervention, to human senses: *magnetic fields* in the interstellar medium, which are measured through the *polarization properties* of low-frequency *radio waves*. In the pages that follow I introduce each of these invisible phenomena, to provide context for the research in the later chapters.

1.1 Interstellar magnetic fields

Magnetic fields[1] are present through interstellar space, with typical strengths ranging from a few microGauss in the Galactic halo [Mao et al., 2012] up to a few milliGauss in very dense molecular clouds [Crutcher, 2015]. These magnetic fields play a major role in many processes in the interstellar medium (ISM), including deflection of cosmic ray particles [Farrar, 2016], transporting angular momentum during cloud collapse in star formation [van Loo et al., 2012], and contributing to the pressure balance of the ISM [Boulares & Cox, 1990]. The energy density of the magnetic field is of similar magnitude to the turbulent motion kinetic energy density and much greater

[1] Strictly speaking, magnetic field should never be pluralized, as it is a single vector field which depends on position and time. Colloquially, it is common to decompose or divide the magnetic field into components, based on its position or source (e.g. the Earth's magnetic field, or the magnetic field in the Solar wind), or by specific properties (e.g. the large-scale component of the interstellar magnetic field).

than the thermal energy density [Beck, 2007]. This indicates that the plasma in the ISM is tied to the magnetic field lines and must either follow the field lines or drag them along, and that the magnetic field configuration and the turbulent motion can have strong influences on each other.

Magnetic fields in the ISM are thought to be generated and sustained by dynamo processes [Brandenburg, 2015]. Dynamo processes are magnetohydrodynamic (MHD) phenomena wherein interactions between an initial magnetic field and the motion of a conductive fluid (such as the plasma present throughout much of the ISM) cause the magnetic field to be amplified, producing a positive feedback loop that maintains the magnetic field. There are several different dynamo processes that can operate, depending on the magnetic field configuration and the motion of the fluid. In the ISM, two types of dynamo are usually considered: mean-field dynamos, which operate on large (kpc) physical scales and produce magnetic fields on those scales, and turbulent dynamos, which operate on smaller scales (100 pc and below).

For this reason, as well as observational limitations, magnetic fields in the ISM are typically divided into two or more components: the large-scale component, which defines the shape of the magnetic field across the Galaxy, and the small-scale/turbulent/random component, which includes all the fluctuations smaller than the large-scale component. In recent years, several papers have divided the small-scale component into two separate components: a isotropic random component, and an anisotropic component which is called ordered [Jaffe et al., 2010] or striated [Jansson & Farrar, 2012]. Observationally, the distinction is based on resolution when looking at the magnetic fields in nearby galaxies: features that are large enough to be resolved are large-scale, while features too small to be observed are small-scale.

1.1.1 Observing magnetic fields

The methods of observing astrophysical magnetic fields are necessarily indirect: magnetic fields do not produce electromagnetic radiation, so we must observe the effects that the magnetic fields have on the radiation from other sources. Most of these methods involve the polarization properties of light, which are altered by the presence of magnetic fields.

Zeeman splitting is a change in the energy levels of some atomic and molecular states when a magnetic field is present. This causes transitions involving those levels to have spectral lines at slightly different wavelengths, typically in groups of three. The separation between the lines is proportional to the magnetic field strength at the location of of the emitting matter, so the magnetic field strength can be inferred by measuring this separation. However, in many cases the magnetic field is weak so that this separation is smaller than the line width and cannot be reliably measured. The separated lines also have different polarization properties (one line is right-circularly polarized, the other left-circular), so in cases where the separation is too small to be directly measured it is sometimes possible to measure the distinctive polarized line profile that is produced and estimate the magnetic field strength.

Rotating, elongated, interstellar dust grains have the property that they tend to align their rotation (short) axis parallel to the magnetic field. This produces two observational signatures: polarized absorption of starlight in the optical and near infrared, and polarized radiation in the far infrared and microwave regimes. These elongated or asymmetric dust grains have the property of dichroism or diattenuation; they preferentially absorb light polarized perpendicular to the axis

of rotation, leaving a net linear polarization along the rotation axis, which corresponds to the magnetic field orientation (as projected in the plane of the sky). When light from an unpolarized source (such as a star) passes through interstellar dust, it picks up a net polarization parallel to the magnetic field component projected into the plane of the sky. The polarization of starlight can be measured, and used to infer the orientation of the magnetic field along the line of sight between the Earth and each star. The strength of this effect is still somewhat poorly constrained by models and is highly dependent on the distribution and properties of the dust, so while it is straightforward to estimate the orientation of the magnetic field it is much more difficult to estimate the strength of the magnetic field.

Interstellar dust grains also produce thermal emission with a polarization dependence; they preferentially radiate along the long axis of the grains, producing a net polarization orthogonal to the magnetic field orientation (projected perpendicular to the line of sight, or equivalently, in the plane of the sky as seen by the observer). As with the starlight absorption, this allows for the orientation of the magnetic field to be measured, but estimating the strength of the magnetic field is more difficult. This emission is predominantly in the far infrared, due to the temperature of the emitting dust grains, and was extensively mapped out by the *Planck* satellite.

The following two methods are directly relevant to the work in this thesis. Synchrotron radiation is produced when cosmic ray electrons, which are highly relativistic, propagate through a region with a magnetic field (such as interstellar space), as the result of the acceleration caused by the Lorentz force. The intensity of synchrotron emission depends on the cosmic ray density and the strength of the magnetic field. When studying synchrotron emission from nearby galaxies, often assumptions are made about the relationship between cosmic ray density and the magnetic field, in order to make estimates of the magnetic field strength; typical assumptions include minimum total energy density (the lowest possible sum of cosmic ray energy density and magnetic field energy density to produce the observed emission), equipartition of energy (equal energy density for cosmic rays and magnetic fields), or pressure equilibrium (equal pressure caused by each) [Beck & Krause, 2005]. Synchrotron emission is strongly directional, due to relativistic beaming, emitting primarily perpendicular to the magnetic field direction; as a result the synchrotron emissivity is determined by the strength of the magnetic field perpendicular to the line of sight, rather than the total magnetic field strength.

Synchrotron emission is also intrinsically polarized perpendicular to the magnetic field at the point of emission. The polarization of synchrotron emission can be used to determine the orientation of the magnetic field in the plane of the sky, through the polarization angle, and to estimate the degree of uniformity of the magnetic field, through the polarization fraction. If the magnetic field is completely uniform (constant field strength and orientation), the resulting synchrotron emission has an intrinsic polarization fraction of about 70%, depending slightly on the spectral index [Pacholczyk, 1970]. If the magnetic field has a more complex morphology, the fractional polarization will drop (if the structure in the magnetic field is smaller than the resolution of the observer). If the magnetic field has no preferred orientation, then there will be no net polarization. From the polarized fraction, the ratio of regular magnetic field (the magnetic field structure on scales larger than the resolution) to total magnetic field can be estimated [Beck & Krause, 2005], and this can be combined with estimates of the total field strength from the

synchrotron total intensity to estimate the regular and turbulent magnetic field strength. This method is used primarily for observing the magnetic field in nearby galaxies.

Finally, there is Faraday rotation, which occurs when polarized emission (typically synchrotron emission) passes through a magnetized plasma and has its polarization properties altered. Faraday rotation and its properties is critical for the work in this thesis and is discussed in more detail in Section 1.4.2.

1.2 Interstellar medium

The interstellar medium (ISM) consists of the matter in a galaxy not associated with or bound to stars. For the Milky Way, this is about 5% of the mass of the galaxy, roughly 7 million solar masses of material [Draine, 2011]. This material is distributed throughout our Galaxy, and exists in a variety of conditions, with varying densities, temperatures, and ionization and chemical states. Most of the matter in the ISM is divided into different gas *phases*, which have very different conditions but are all able to maintain approximate equilibrium between heating and cooling processes and pressure balance with respect to the other phases. These phases are the hot ionized medium (HIM, also called coronal gas), the warm ionized medium (WIM), the warm neutral medium (WNM), and cold neutral medium (CNM), cold molecular gas, and H II regions. Some variations on these classifications exist, and also variations on the estimates of the temperatures and densities; my descriptions and values are based on those found in Draine [2011] and Tielens [2010]. Interstellar dust is also present throughout all phases of the ISM, but is mostly concentrated in the higher density gas phases.

The hot ionized medium is, as the name suggests, the hottest and most tenuous phase with typical temperatures of $10^{5.5}$ – 10^6 K and (number) densities about 0.004 cm^{-3}, and is completely ionized. The hot phase is generally associated with bubbles and super bubbles in the ISM, from supernovae or strong winds, and is also much more common in the Galactic halo. The HIM phase is thought to fill roughly half of the volume of the ISM, although this is probably a function of distance from the Galactic plane. The Sun is imbedded in a large region of HIM called the Local Bubble.

The warm phases occupy most of the remaining volume of the ISM. The equilibrium temperature of the warm phase is typically between 5000 and 10000 K (depending on the model used), and densities of approximately 0.1 – 0.6 cm^{-3}. The warm material is generally thought to be separated into regions that are highly ionized (WIM) or have very low ionization (WNM), although some models also consider partially ionized regions. The neutral phase still has trace amounts of ionization, caused by processes like cosmic ray interactions, which is necessary to maintain the magnetic field.

The cold phases occupy a small fraction of interstellar space, but contain a large fraction of the total mass. The typical temperature is 100 K or below, and densities are from 30 cm^{-3} and up; the more diffuse regions (CNM) are dominated by cold atomic gas, while the higher density regions (molecular clouds) are dominated by molecular gas. These phases are concentrated strongly to the Galactic plane, with typical scale heights of only about 100 pc.

H II regions are warm, ionized, high density (1–10^5 cm^{-3}) regions that are formed around

sources of ionizing radiation (very hot stars, primarily). These regions are often significantly over-pressured and expanding into the ambient medium.

1.3 LOFAR

In recent years, radio astronomy has returned to its roots at the low-frequency end of the radio band. Many of the very first radio telescopes, including those made by Karl Jansky, Grote Reber, and Bernard Lovell, operated at very low frequencies (below 200 MHz) as the technology for high-frequency electronics had not yet advanced significantly. As these electronics were developed, most radio astronomy work became focused on higher frequencies where better angular resolution could be achieved for the same size of telescope dish. However, as the cost of electronics continued to drop, it became cost effective to develop and construct *phased array* radio telescopes, which can replace the large dishes and moving parts used in traditional radio telescope designs with electronic signal processing that can accomplish the same results. Several large low-frequency phased array telescopes have been built in recent years, such as the Low-Frequency Array (LOFAR) in Europe, the Murchison Wide-field Array (MWA) in Australia, and the Long Wavelength Array (LWA) in the United States of America.

Phased array systems (also called beam-formers) operate by adding the signals from multiple antennas together. This offers two advantages: improved sensitivity, and directional sensitivity. The improved sensitivity comes from increasing the amount of radio signal being collected; the signal from each antenna adds coherently while the noise adds incoherently, so the signal-to-noise ratio increases when the signals are added together. However, for the signals to be added coherently it is necessary to ensure that signals from the target source are synchronized, since antennas at different locations may receive the same signal at different times due to the finite speed of light. To synchronize the signals, time delays are introduced before the signals are added together; the delays required for coherent addition depend on the locations of the antennas and the direction of the signal. If the time delays are set for a particular direction, then radio signals coming from other direction will be desynchronized (out of phase) when they are added, causing them to have reduced strength. The result is that a phased array system is always most sensitive in one particular direction, and less sensitive in other directions; the pattern of sensitivity as a function of position is called the *beam* of the array. Phased arrays can operate without any moving parts; the antennas can remain in fixed locations and the time delays can be adjusted to make the beam most sensitive to the direction of the target being observed.

The LOFAR High-band Antennas (HBA) operate as a four level system, which is described in full detail in van Haarlem et al. [2013a]. The first level is the individual antennas: a pair of butterfly/bowtie dipoles oriented perpendicular to each other, which are capable of observing between 110–250 MHz. These are grouped into 16-antenna ‘tiles’, which act as phased arrays producing two analog output signals per tile (corresponding to the orthogonal antenna orientations), which are then digitized. The tiles are in groups of 24 or 48, called ‘stations’; the signals from all the tiles in a station are combined as a digital phased array. Since the tile signals are digital they can be duplicated or manipulated without any loss of sensitivity or information, which allows for many different station beams to be produced (with different time delays corresponding to different

target directions) limited only by the computational power available. The current computational resources allow for up to 96 MHz of bandwidth divided into 488 sub-bands, or the bandwidth can be exchanged for additional beams entered on different locations (for example, two simultaneous beams of 48 MHz). A picture of the LOFAR 'superterp' core is shown in Figure 1.1

Figure 1.1: Image of the LOFAR 'superterp', where the 6 central stations of the array are located. The small black squares are HBA tiles containing 16 antennas. Image credit: LOFAR / ASTRON.

At the final level, signals from the different stations are either added together (phased array mode) or correlated with each other (interferometer mode). The phased array mode maximizes sensitivity, at the cost of having a very narrow field of view, while the interferometer mode can map out larger areas of sky with slightly lower sensitivity. In the interferometer mode, the combination of antenna beam, tile beam, and station beam collectively defines the 'primary beam' (the overall sensitivity pattern on the sky), and the distribution of baselines between different stations determines the shape of the synthesized beam/point spread function and in turn the resolution.[2] The 'Dutch array' portion of LOFAR (which excludes the international stations, which are typically used for very high resolution observations and require special calibration), consists of 46 stations and has baselines of up to 120 km between stations. This allows for resolution as fine as 5″to be achieved.

[2]While writing my first LOFAR paper (Chapter 2), I was advised by Prof. Ger de Bruyn that, since LOFAR involves so many uses of the word 'beam', it is helpful to use 'point spread function' in the place of 'synthesized beam' which is more common in radio interferometry, as this substitution can help reduce confusion over which beam is meant in any given context. I have tried to follow this advice throughout my thesis.

1.4 Polarization

The properties of the polarization of radio waves are critical to the research in this thesis. Detailed introductions to polarization, including mathematical derivations, can be found in most electromagnetism or optics textbooks [e.g. Hecht, 2001; Jackson, 1998]; I give a brief introduction to the relevant properties here, skipping the full mathematical derivations.

1.4.1 Basic definitions

Electromagnetic (EM) waves are, as the name suggests, composed of electric and magnetic fields, both vector fields. The magnetic field component can be determined from the electric field component and Maxwell's equations, so EM waves are typically described in terms of their electric fields alone. Maxwell's equations also dictate that EM waves are transverse waves, so that (in a vacuum) the electric field is perpendicular to the direction of travel. If we consider a Cartesian coordinate system where the z-axis is oriented in the direction of travel of the wave, then the electric field vector is confined to the x-y plane. Mathematically, the wave can be decomposed into separate components along the x- and y-axes, each of which is separately a solution to the electromagnetic wave equation. Each component is defined by an electric field amplitude (E_x, E_y) and phase (θ_x, θ_y). However, since we have not fixed our coordinate system to a particular time and location the absolute phases are arbitrary, but the phase difference $(\theta_{xy} = \theta_x - \theta_y)$ is a meaningful quantity. As a result, the polarization properties of a single EM wave can be described by 3 parameters.

To understand these 3 parameters, and their transformations, it is useful to consider two special cases. The first is the case where the phase difference is equal to 0 or 180°. When this occurs, the x- and y-components are oscillating exactly in phase (or exactly out of phase), which results in the electric field vector being confined to a single line on the x-y plane. This is called *linear polarization*, and has a specific parameter associated with it: the polarization angle ψ (sometimes called the electric vector position angle or EVPA), which gives the orientation of the line relative to the coordinate system. Mathematically, it can be defined as $\psi = \arctan\left(\frac{E_y}{E_x}\right)$ and is only defined between 0 and 180°, as a wave with a polarization angle of 180° is equivalent to a wave at 0° with half a period of absolute phase delay.

The second case is when the phase difference is equal to ±90°(and both E_x and E_y are non-zero), which results in the x- and y-components oscillating out of phase. If E_x and E_y are equal, then the electric field vector rotates in a circle, either clockwise or counterclockwise depending on the sign of θ_{xy}[3]. This is *circular polarization*. It is interesting to note that, mathematically, left- and right-circular polarization form a pair of orthogonal basis vectors, and all polarized RM waves can be equally well described as a combination of left- and right-circular polarized waves (with corresponding parameters E_L, E_R, and θ_{RL}) instead of x- and y-parallel linear waves. This property will be useful when considering Faraday rotation later in this chapter.

[3]These are called left- and right-circular polarization, although which is which is an minor problem in definitions: physicists use one coordinate system to match clockwise/anti-clockwise to left/right, while the official IEEE definition used by engineers uses a different coordinate system that produces the opposite pairing. Since radio astronomy originally emerged from electrical engineering, the engineers' definition is generally used. Since circular polarization is not relevant to my thesis, I avoid this problem by being deliberately vague.

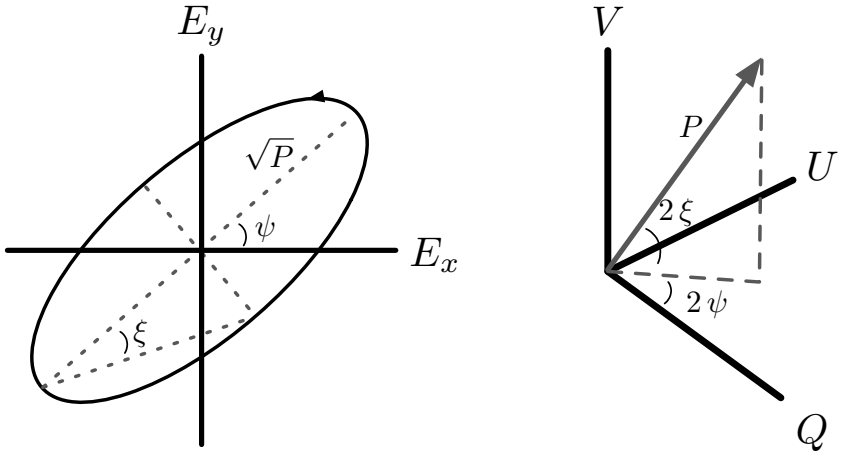

Figure 1.2: *Left:* A polarization ellipse, which can be described in the linear basis (E_x, E_y, θ_{xy}), or in terms of a polarized intensity/semi-major axis and two angles describing the ellipse: the polarization angle ψ and the ellipticity angle ξ. *Right:* The parameter space of polarized waves, which is spanned in cartesian coordinates by the Stokes parameters, Q, U, and V, or in spherical equatorial coordinates (the Poincaré sphere) by the polarized intensity, polarization angle, and ellipticity angle.

In the general case of arbitrary phase difference and amplitudes, the electric field vector traces out an ellipse in the x-y plane. Since an ellipse can be mathematically described in several different ways, there are several sets of parameters that can be used to describe the polarization state of EM waves. The set of (E_x, E_y, θ_{xy}) is used in the Jones vector formalism (in which a wave is described as a complex vector $\vec{E} = [E_x \; E_y \, e^{-i\theta_{xy}}]^{\mathrm{T}}$). Jones formalism is used extensively in radio calibration, as it is mathematically very well suited for describing the signals captured by a polarized antenna and how the electronics of a radio telescope alter those signals [Hamaker et al., 1996].

Another parameter set, which is more useful for visualizing the parameter space of polarization states, uses the polarized intensity, polarization angle, and ellipticity angle (P, ψ, ξ). The polarized intensity P is proportional to the square of the semi-major axis of the ellipse (having units of energy/intensity, instead of electric field); the polarization angle is as defined above. The ellipticity angle is defined as the angle made by the right triangle formed from the semi-major axis and semi-minor axis, but is also a signed quantity to distinguish between left- and right-circularly polarized waves; it takes values between $-45°$ and $+45°$. This set of parameters span the space of possible polarization states in spherical coordinates: the polarized intensity gives the radius, twice the polarization angle gives the azimuthal angle, and twice the ellipticity angle gives the equatorial polar angle. This is called the *Poincaré sphere*; in this representation purely linearly polarized waves (where the ellipticity angle is zero) occupy the equator of the sphere, while purely circularly polarized waves occur at the poles of the sphere. This representation is not typically used in radio astronomy, but serves as an intermediate step between the Jones vector formalism and the Stokes parameters (introduced below). Figure 1.2 shows how the quantities in the polarization ellipse can be mapped onto the Poincaré sphere.

Since the Poincaré sphere represents a spherical coordinate system for the parameter space of polarization states, there is a corresponding cartesian coordinate system. This is the set of

Stokes parameters, Q, U, and V, where Q and U span the equator of the Poincaré sphere (and thus represent the parameter space of purely linear polarization) and V is the vertical axis and gives the degree of circular polarization. In this representation, positive Stokes Q represents polarization along the x-axis, negative Stokes Q polarization along the y-axis, positive Stokes U polarization along the $+45°$ axis, and negative Stokes U polarization along the $-45°$ axis. Each of the Stokes parameters has units of intensity (square of the wave amplitude).

This representation has the advantage of naturally identifying opposite polarization states. Up to this point, I have discussed only the description of the polarization of a single EM wave, which must be polarized. However, when many waves are combined, the superposition can also be partially polarized, or unpolarized. The polarization states of waves add together as vectors, while the intensity/energy content of the waves is a positive-definite scalar that adds linearly. Polarization states can be defined in either as complex Jones vectors or as a Stokes vector, $[Q\ U\ V]^{\mathrm{T}}$, and added together. In the Stokes formalism, a fourth parameter is added, Stokes I, which gives the total intensity of all the waves. The resulting 4-component vector, $[I\ Q\ U\ V]^{\mathrm{T}}$, can describe all possible polarization states of a superposition of waves, including partially polarized and unpolarized states. The Stokes parameters can also be calculated directly from linear combinations of the correlations measured by a dual-polarization interferometer, which typically gives them very simple noise properties in radio observations. For these reasons, the Stokes parameters are the preferred representation for the polarization of astrophysical radio waves.

From the four Stokes parameters, several additional (and more physically interpretable) parameters can be calculated. The polarization angle defined previously, ψ, can be calculated from the Cartesian-to-spherical coordinate transformation using the equation $\psi = \frac{1}{2}\arctan\frac{U}{Q}$ (where the factor of $\frac{1}{2}$ is necessary because polarization angle is only defined up to $180°$, and the azimuthal angle in the Poincaré sphere is correspondingly twice the polarization angle). The (total) polarized intensity is similarly calculated as $P = \sqrt{Q^2 + U^2 + V^2}$. This can also be subdivided into the linear polarized intensity, $\sqrt{Q^2 + U^2}$, and circular polarized intensity $|V|$. In many astrophysical applications (including this thesis), the circular polarized intensity is expected to be zero, and so the term linear polarized intensity and polarized intensity are used interchangeably. Another important parameter is the fractional polarization, P/I, which describes the degree of polarization, from unpolarized to fully polarized.

1.4.2 Faraday rotation

Faraday rotation is a process where interactions between linearly polarized EM waves and magnetized plasma cause the polarization angle to change. Derivations of Faraday rotation can be found in most plasma physics textbooks, such as Choudhuri [1998] or Gurnett & Bhattacharjee [2005]; here I give a brief overview of the cause and focus primarily on how it is observed.

In a plasma electric charges are present, which affects Maxwell's equations and in turn the electromagnetic wave equation. The free electrons, with their much higher charge to mass ratio, are particularly reactive to the presence of electromagnetic waves. For 'cold' plasma, where the electrons' thermal motion is not a significant factor (which is the case for nearly all conditions in the interstellar medium), Maxwell's equations lead to transverse EM wave solutions (as in a vacuum) with one modification: the phase velocity (and thus the index of refraction) is changed

slightly. The index of refraction, μ for EM waves in a cold plasma is given by

$$\mu^2 = 1 - \frac{\nu_p^2}{\nu^2} \tag{1.1}$$

where ν is the frequency of the EM wave, and ν_p is the plasma frequency, given by $\nu_p = \sqrt{(n_e\, e^2)/(\epsilon_0\, m_e)}/(2\pi)$, where n_e is the free electron number density, e is the electric charge, ϵ_0 is the permittivity of free space, and m_e is the electron mass. The result is that at very high frequencies waves are not affected by the plasma, while waves with frequencies below the plasma frequency are absorbed. For typical conditions in the interstellar medium, the plasma frequency is of the order of kilohertz, so waves in the MHz regime and above are affected only minimally.

When a magnetic field parallel to the propagation direction is introduced to the plasma the complexity again increases, as the electron motion in response to the EM waves is now affected by the magnetic Lorentz force. This introduces an asymmetry that produces two different solutions to the resulting wave equation. In the vacuum and non-magnetized plasma cases, these two solutions (eigenmodes) were degenerate and we chose the solutions to be linearly polarized along the x- and y-axes, but in the magnetized plasma case the solutions are left- and right-circular polarized waves. The index of refraction for these waves is

$$\mu^2 = 1 - \frac{\nu_p^2}{\nu(\nu \pm \nu_B)} \tag{1.2}$$

where $+$ is for left-circular and $-$ for right-circular polarized waves (in the physics convention for left/right circular polarization), and $\nu_B = (eB_\parallel)/(2\pi\, m_e)$ is the cyclotron frequency, and $B_\parallel$ is the strength of the magnetic field parallel to the direction of propagation. The index of refraction is different between the left- and right-circular polarizations, resulting in a correspondingly different phase velocity ($v_{\rm phase} = c/\mu$).

This has the result that if a left-circular polarized wave and a right-circular polarized wave are propagating together through a magnetized plasma, the relative phase between them will change as the waves propagate. In the circular polarization parameterization, the phase difference relates directly to the linear polarization angle: $\psi = \theta_{RL}/2$. So a linearly polarized wave passing through magnetized plasma undergoes a change in polarization angle as it propagates. The rate of change of polarization angle, with respect to path length (l) through the magnetized plasma, is

$$\frac{\mathrm{d}\psi}{\mathrm{d}l} = \frac{1}{2}\frac{2\pi\,\nu_p^2\,\nu_B}{c\,\nu^2} = \frac{n_e\, e^3 B_\parallel}{8\pi^2\, m_e^2\, c\, \nu^2\, \epsilon_0}. \tag{1.3}$$

This is the physical process of *birefringence*: the index of refraction of magnetized plasma depends on the direction of propagation and the polarization state of the wave. The polarization angle of a linearly polarized emission source at a distance d, seen by some observer is then given by

$$\int_{\rm source}^{\rm observer} \frac{\mathrm{d}\psi}{\mathrm{d}l}\mathrm{d}l = \frac{e^3}{8\pi^2\, m_e^2\, c\, \nu^2\, \epsilon_0}\int_d^0 n_e\, B_\parallel\, dl \tag{1.4}$$

$$\psi_{\rm observer} - \psi_{\rm source} = \lambda^2 \frac{e^3}{8\pi^2\, m_e^2\, c^3\, \epsilon_0}\int_d^0 n_e\, B_\parallel\, \mathrm{d}l \tag{1.5}$$

$$\psi_{\rm observer} = \psi_{\rm source} + \lambda^2\phi \tag{1.6}$$

where λ is the observing wavelength (c/ν), $\psi_{\rm source}$ is the polarization angle at the source of emission, both dl, and $B_\parallel$ are defined as positive towards the observer, and ϕ is called the *Faraday depth*. The Faraday depth is defined as

$$\phi = \frac{e^3}{8\pi^2\, m_e^2\, c^3\, \epsilon_0} \int_d^0 n_e\, B_\parallel \,\mathrm{d}l = 0.812 \text{ rad m}^{-2} \int_d^0 \left(\frac{n_e}{\mathrm{cm}^{-3}}\right) \left(\frac{B_\parallel}{\mu\mathrm{G}}\right) \left(\frac{\mathrm{d}l}{\mathrm{pc}}\right), \tag{1.7}$$

represents the rate of change of polarization angle with respect to wavelength (squared), and correspondingly has units of angle per unit wavelength squared. This quantity, and its definition, is critical for the contents of this thesis. In terms of Poincaré sphere, Faraday rotation acts as a wavelength-dependent rotation in the azimuthal angle, rotating the polarization vector in the Q-U plane without changing the polarized intensity.

Due to the wavelength dependence of Faraday rotation, the effect is much stronger and more easily observed at long wavelengths (low frequencies). For this reason, Faraday rotation is typically observed at radio frequencies, usually below 10 GHz, although under extreme conditions (such as around active galactic nuclei) the effect may be noticeable in the sub-mm regime. The typical Faraday rotation caused by our Galaxy can vary from of order 10 rad m^{-2} for lines of sight going through the Galactic halo [Mao et al., 2012], to several hundred rad m^{-2} for lines of sight through the Galactic plane [Van Eck et al., 2011], up to values as high as 10^5 – 10^6 rad m^{-2} at the Galactic center [Moscibrodzka et al., 2017].

The traditional method of measuring the Faraday depth of a particular source of linear polarization is to observe the polarization angle at several wavelengths, and fit a linear relationship for ψ as a function of λ^2 [e.g. Rand & Lyne, 1994; Brown & Taylor, 2001]. The measured slope of this relationship is called the Faraday rotation measure (RM), and is normally defined as

$$\mathrm{RM} = \frac{\mathrm{d}\psi}{\mathrm{d}\lambda^2}. \tag{1.8}$$

In the case of single source of polarized emission at a single distance, the rotation measure is equal to the Faraday depth of the source. However, in more complicated cases the relationship between observed polarization angle and λ^2 can become non-linear, causing the RM to become a function of λ^2 and to have a more complicated relationship with the Faraday depth. A few examples of how this can occur are considered below.

If there are multiple sources of polarized emission at different distances, with correspondingly different Faraday depths, the observed polarization is the vector sum of the individual polarization components. Since the different contributions in the vector sum have different wavelength dependencies (different Faraday depths), the sum has a complex dependence on wavelength. As a result, the change in the polarization angle of the sum will not change linearly with λ^2, and a linear fit will not produce a meaningful result.

Another case that will produce similarly non-linear behaviour is when a source of polarization is distributed in distance and the emitting volume also causes Faraday rotation. The emission nearer the observer will undergo a different amount of Faraday rotation than emission further away, and the resulting observed polarization will the superposition of emission with many different Faraday depths. This is called a Faraday slab, or Burn slab [Burn, 1966].

The development of new methods to deal with these more complicated, nonlinear cases has been a subject of increased interest in recent years, as new radio telescopes with much larger

bandwidths (and correspondingly better ability to detect non-linear polarization behaviour) have been developed. Two major techniques currently dominate: rotation measure synthesis, which is described in the next section (and used extensively in this thesis), and QU fitting, which is the extension of the linear fitting method to consider more complex models with multiple polarization sources or more complex sources.

1.4.3 Rotation measure synthesis

The mathematical derivation of the rotation measure synthesis technique was first laid out by Burn [1966], and was further developed into a useable form by Brentjens & de Bruyn [2005]. Below I briefly lay out the mathematical structure of the method and describe the practical aspects of its implementation.

It is convenient, in terms of the mathematical formalism, to define the complex polarization $\widetilde{P}$ (I will use the tilde symbol to denote complex quantities) in terms of the Stokes Q and U parameters or the polarized intensity P and polarization angle ψ,

$$\widetilde{P} = Q + i\,U = P\,^{2i\,\psi}. \tag{1.9}$$

In this notation, a Faraday-rotated polarized signal with a Faraday depth ϕ can be described as

$$\widetilde{P}(\lambda^2) = P\,e^{2i(\psi_0+\lambda^2\phi)} = \widetilde{P}_0\,e^{2i\lambda^2\phi}, \tag{1.10}$$

where the 0 subscript is used to denote the pre-rotation quantities; $\widetilde{P}_0$ is the pre-rotation polarization and $e^{2i\lambda^2\phi}$ is change made by Faraday rotation.

In principle, polarized emission can be produced at any distance along a given line of sight, and emission at all distances will be summed together to give the observed polarized signal. For each distance, there is an associated Faraday depth, so it is possible, in theory, to map the emitted polarization as a function of distance, $\widetilde{P}_0(d)$, to the emitted polarization as a function of Faraday depth, $\widetilde{P}_0(\phi)$. At any given wavelength, the polarization at the observer is the combination of all such emission, modified by the Faraday rotation:

$$\widetilde{P}(\lambda^2) = \int_{-\infty}^{\infty} \widetilde{P}_0(\phi)\,e^{2i\lambda^2\phi}\mathrm{d}\phi. \tag{1.11}$$

This has precisely the form of an inverse Fourier transform, with λ^2 as the time-like variable and ϕ as the frequency-like variable. We can measure $\widetilde{P}(\lambda^2)$, and would like to extract $\widetilde{P}_0(\phi)$, which contains information on the polarization properties of the emission source as well as the Faraday rotation properties of the line of sight being probed. In principle, this can be straightforwardly done through the application of a forward Fourier transform to the observed polarization. In practice, we have limited information on the observed polarization due to limited coverage of the λ^2 domain, as real telescopes have only finite frequency bandwidth.

The issue of having limited measurements of $\widetilde{P}(\lambda^2)$ is dealt with by introducing a weighting/sampling function, which is non-zero at every λ^2 where a measurement exists and zero otherwise.[4] This allows for the limited information to be explicitly accounted for in the mathematics,

[4]During his sabbatical visit to the RU Astronomy department, I had several enjoyable conversations with Prof. Colin Norman of John's Hopkins University. Collin pointed out to me that the time-domain in a Fourier

and also naturally includes the discretized channelization of real data as the weight function can be made a series of delta functions for the λ^2 values of each channel.

We can then take the measured polarization, the product of the weight function $W(\lambda^2)$ and $\widetilde{P}(\lambda^2)$, as apply a Fourier transform; the result (through the Fourier convolution theorem) is the convolution of the polarization as a function of Faraday depth, $\widetilde{P}_0(\phi)$, and the Fourier transform of the weight function:

$$\mathcal{F}(W(\lambda^2) \cdot \widetilde{P}(\lambda^2)) = \widetilde{P}_0(\phi) * \mathcal{F}(W(\lambda^2)) = \widetilde{P}_0(\phi) * \widetilde{R}(\phi) \tag{1.12}$$

where $\widetilde{R}(\phi)$ is the Fourier transform of the weight function, and is called the rotation measure transfer function (RMTF) or rotation measure spread function (RMSF). The RMSF determines the resolution in RM synthesis, and is equivalent to the PSF/synthesized beam in radio interferometry; a typical RMSF for a LOFAR observation is shown in Figure 1.3. The polarization as a function of Faraday depth, $\widetilde{P}_0(\phi)$, is also called the *intrinsic Faraday spectrum*, and the convolution of this with the RMSF is the *observed Faraday spectrum*.

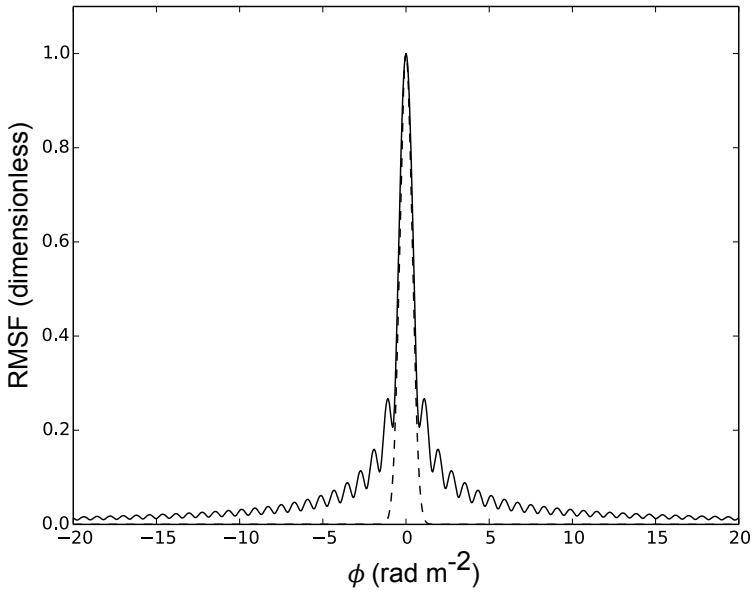

Figure 1.3: Top panel from Figure 8 of Van Eck et al. [2017], showing a typical LOFAR RMSF. The solid line is the RMSF obtained from uniform frequency coverage from 115–178 MHz; the dashed line is a Gaussian function with the width matched to the main lobe of the RMSF, which is used in the RM-CLEAN deconvolution algorithm.

The RMSF, and the limited sampling that causes it, introduce limitations to RM synthesis that need to be considered before interpreting observed Faraday spectra. The first limitation is the resolution: a typical RMSF will have a central peak with a well defined width, which causes narrow

transform extends from negative infinity to positive infinity, while the λ^2 domain in RM synthesis is positive definite, and that this could impact the invertability of the transform. This bothered me greatly, but addressing this issue rigorously would have required relearning complex analysis. In the end, I concluded that since we already have only limited sampling in the positive λ^2 regime, having no sampling at all in the negative regime is unlikely to add any new problems.

features in the Faraday spectrum to be broadened and adjacent features to become merged. The width the RMSF peak is inversely proportional to the the range of λ^2 values observed; Equation 61 of Brentjens & de Bruyn [2005] estimates that the full-width at half-max (FWHM) of the RMSF peak is given by $2\sqrt{3}/(\lambda^2_{\rm max} - \lambda^2_{\rm min})$. This dependence motivates the use of low-frequency radio telescopes for RM synthesis, as these telescopes are able to achieve very large λ^2 ranges for the same fractional bandwidth. To give a concrete example, an observation made between 100 and 200 MHz (somewhat larger that the typical LOFAR frequency range) covers a λ^2 range 2.25–8.99 m^2 and would have a Faraday depth resolution of 0.51 rad m^{-2}, while an observation from 1–2 GHz (which could be done by the Very Large Array) covers 0.022–0.090 m^2 and would have a resolution of 51 rad m^{-2}. Even a hypothetical observation from 1 GHz up to infinite frequency, with a λ^2 range of 0–0.090 m^2, would have a Faraday depth resolution of 38 rad m^{-2}; the only way to resolve Faraday depth structure narrow than 10 rad m^{-2} is to observe below 500 MHz.

The second limitation is loss of sensitivity to broad features in Faraday spectra. This is directly analogous to the 'missing short spacings' problem in radio interferometry where emission on large angular scales is not detected. The effect of this is that broad structures may not be observed, leaving only the narrower features. The Faraday depth scale at which an observation has 50% sensitivity is given by Equation 62 in Brentjens & de Bruyn [2005] as $\pi/\lambda^2_{\rm min}$. It is possible for this scale to be similar to or smaller than the resolution of the RMSF, which has the effect of making it impossible to resolve broad structures in Faraday depth; in this case only structures narrower than the resolution can be observed. This is generally the case for the LOFAR observations described in this thesis, and has repercussions for what Faraday depth spectrum features can be observed and how these features can be interpreted; this is discussed in detail in the relevant chapters. The breadth of a feature in Faraday depth is often called the Faraday thickness, and the terms 'Faraday thin' and 'Faraday thick' are sometimes used to describe features that are narrower or broader, respectively, than the RMSF.

The third limitation is loss of sensitivity to large (positive and negative) Faraday depths. This is caused by the fact that the polarization measurements are not infinitely narrow in λ^2, but are averages over a finite bandwidth. If the polarization changes significantly (such as by very strong Faraday rotation) within that bandwidth, the vector average will have lower polarized intensity; this is called bandwidth depolarization. The Faraday depth at which sensitivity has dropped to 50% is given by Equation 63 in Brentjens & de Bruyn [2005] as $\sqrt{3}/\delta\lambda^2$ where $\delta\lambda^2$ is the width of a single channel in the λ^2 domain. This makes it necessary, when planning an observation, to balance between fewer and wider channels, which reduces the computational overhead, or more and narrower channels, which allow for higher Faraday depths to be probed. If the observation target is expected to have small Faraday depths (such as local emission or targets in the Galactic halo), then this problem is less restrictive.

To reduce the presence of the RMSF sidelobes, an algorithm based on the CLEAN algorithm from radio interferometry was developed to perform partial deconvolution of observed Faraday spectra, called RM-CLEAN [Heald et al., 2009]. This algorithm finds the maximum polarized intensity present in a Faraday spectrum, subtracts a scaled version of the RMSF centred on that location, and, after the previous steps are repeated until a threshold is reached, adds back

Gaussian components scaled to the same width as the RMSF main peak (such a Gaussian is shown in Figure 1.3). This allows for fainter components, which would otherwise be hidden in the sidelobes of brighter features, to be identified, analogously to how CLEAN increases dynamic range in interferometry.

With modern radio telescopes it is possible to carry out RM synthesis not just on single sightlines or single targets but to create *Faraday depth cubes*, which consists of Faraday spectra for each pixel in an image of a region of the sky. Faraday depth cubes can be used to study the polarization and Faraday rotation of diffuse emission or objects that cover large areas of the sky. The production and analysis of Faraday depth cubes is sometimes called *Faraday tomography*, as it allows us to view the polarized sky as a series of image slices separated in Faraday depth.

1.5 Faraday tomography of the local interstellar medium: previous and concurrent work

Since the introduction of RM synthesis, there have been many papers using the method to probe the polarization properties of unresolved sources [e.g. Van Eck et al., 2011; O'Sullivan et al., 2012] or discrete resolved objects [e.g. Pizzo et al., 2011; Mao et al., 2015], but relatively few papers exploring the polarization of the diffuse Galactic foreground.

de Bruyn & Brentjens [2005] and Brentjens [2011] used RM synthesis on observations of the Perseus galaxy cluster made with the Westerbork Synthesis Radio Telescopes (WSRT) between 314 and 383 MHz (with a corresponding Faraday depth resolution of 16 rad m^{-2}). They found diffuse emission on large ($10'$) scales at low Faraday depths ($\phi < 20$ rad m^{-2}), which they attributed to local Galactic emission, and smaller features at much higher Faraday depths ($\phi \approx 50$ rad m^{-2}) which were initially attributed to the cluster [de Bruyn & Brentjens, 2005] but were later thought to be Galactic in origin [Brentjens, 2011].

Iacobelli et al. [2013] used RM synthesis with low-frequency (139–155 MHz, giving a Faraday depth resolution of 3 rad m^{-2}) data from the WSRT to investigate the diffuse polarization of a highly polarized region of the sky called the FAN region. They identified several features in the diffuse polarization, which they named the 'bubble', the 'ring', and the 'curtain'. They attempted to associate these features with structures in the ISM; they proposed that the curtain was associated with the wall of the Local Bubble, and considered several possible counterparts to the bubble, including an old supernova remnant or an old planetary nebula.

Jelić et al. [2014] and Jelić et al. [2015] applied RM synthesis to LOFAR observations of two Epoch of Reionization fields centred on the ELAIS-N1 field and the bright radio source 3C196. In the ELAIS-N1 field they observed clear polarized diffuse emission, with a brightness temperature of about 4 K (compared to a total brightness temperature of about 300 K), at low Faraday depths between -10 rad m^{-2} and $+13$ rad m^{-2}. In the 3C196 field, they observed diffuse polarized emission across the field, as well as several distinct features in Faraday depth. They observed a very straight filamentary feature, several degrees long, that produced an offset of 1.5 rad m^{-2} in Faraday depth, which they interpret as a ionized structure in the local ISM. They also observed a number of unusually straight depolarization canal-like features, which they interpret as being associated with especially turbulent regions of ISM, but they are unable to explain the

very straight nature of these features.

A very interesting follow up on the 3C196 field was done by Zaroubi et al. [2015], who found that the structure of the diffuse polarized emission strongly followed the magnetic field lines inferred from the dust polarization observed by the *Planck* satellite. These field lines were parallel to the long filamentary feature, and were perpendicular to observed gradients in Faraday depth (stated differently, the *Planck* magnetic field lines appeared to double as lines of constant Faraday depth in the 3C196 Faraday depth cube), at least in parts of the field.

Lenc et al. [2016] also looked at diffuse polarization at very low frequencies (139–231 MHz), using the MWA, in a very large (625 deg^2) field in the southern hemisphere at comparatively low resolution ($50'$). They detected diffuse emission in their field, at a fairly high intensity level (4–11 K brightness temperature at 154 MHz), indicating that either that region had strong polarized emission or that the beam depolarization was not as strong as expected. They estimated the distance to this emission using two methods: assuming a single-phase medium with typical (volume-averaged) ISM parameters, they concluded that a distance of 110–220 pc would be needed to produced the observed Faraday rotation; and by using pulsar in the field with a known distance and Faraday depth, and assuming a uniform medium between Earth and the pulsar, concluded that the distance should be approximately 51 ± 20 pc. Neither calculation included the (reduced) Faraday depth contribution of the Local Bubble.

These papers point to a few clear directions for further investigation. First, all of the observations except for Lenc et al. [2016] consisted of only single, small fields, and several showed structure that extended beyond the field of view; Lenc et al. [2016] covered a large area of sky, but lacked the resolution to probe Faraday depth structure in detail. Second, the analysis of the observed Faraday depth features was limited by the lack of associated ISM structures, which would have provided additional information on the nature of these features. Thirdly, the specific properties of RM synthesis at low frequencies, specifically with respect to how this affected what Faraday depth structures could be observed, was not explored in detail. The goal of the work in this thesis was to explore each of these directions, while increasing the area of sky studied with Faraday tomography.

1.6 This thesis

While RM synthesis/Faraday tomography has been used extensively since its development in 2005, the interpretation of Faraday spectra and Faraday depth cubes as well as the development of methods of extracting useful information from these data have all developed slowly. To date, very little of the sky has been probed using Faraday tomography; most observations with which RM synthesis has been used have had some combination of small field of view, limited short spacings (limiting detection of large-scale diffuse emission), relatively high frequency (giving very poor Faraday depth resolution), or poor image-plane resolution (resulting in beam depolarization and limiting the ability to detect smaller features). LOFAR offers a unique opportunity to overcome most of these limitations, with a large field of view (approximately 3 degree FWHM), high sensitivity to diffuse emission, very high Faraday depth resolution (≈ 1 rad m^{-2}), and sub-arcminute resolution.

Figure 1.4 shows the sky coverage of previous Faraday tomography observations, and emphasizes how little of the sky has been explored in this way.

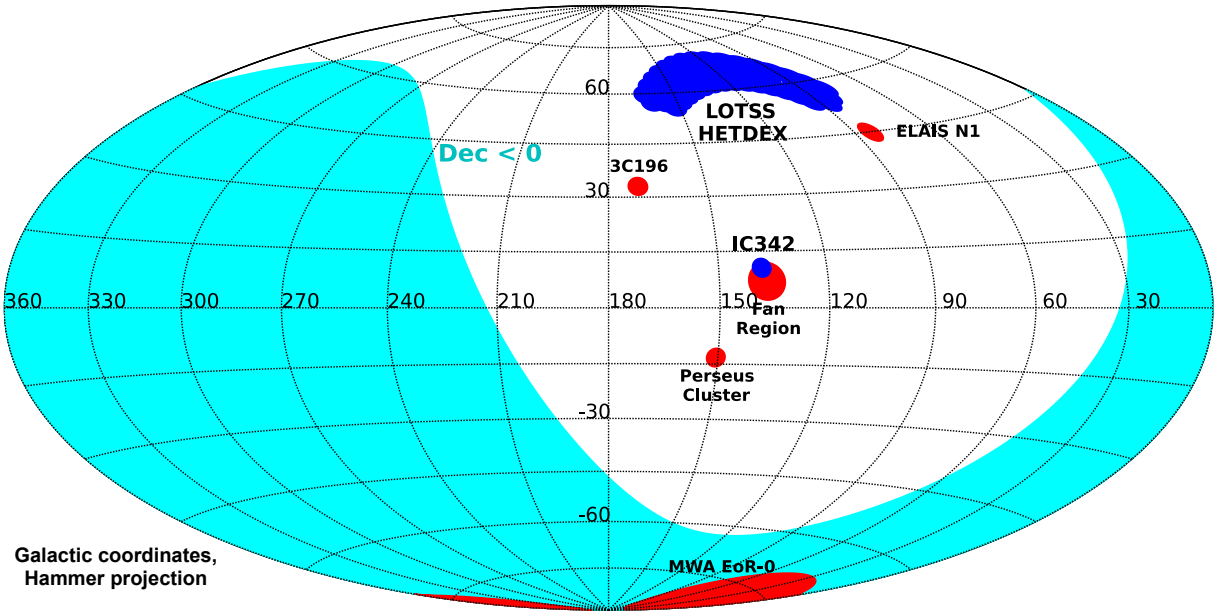

Figure 1.4: A map of the sky (in Galactic coordinates) showing the areas for which Faraday tomography has been used to study the diffuse Galactic polarized foreground. Fields in red are the previous and concurrent work described in Section 1.5; fields in blue are observations described in this thesis. The southern sky (below declination 0, where LOFAR has limited or no sensitivity) is shaded cyan.

The work in this PhD thesis focuses on exploring the use of Faraday tomography on LOFAR data and determining how this data can be used to measure the properties of magnetic fields in the interstellar medium. This work was primarily focused on two questions: "What can we see in the high-Faraday depth resolution polarized sky?", with an emphasis on finding features that can be linking to objects in the ISM; and "How can we interpret these data?", looking mostly at the limitations of RM synthesis and the implications on what physical conditions we can probe with low-frequency polarimetry.

In Chapter 2, I present the work I carried in calibrating data from some of the first post-commissioning LOFAR observations, centred on the nearby Galaxy IC342, and the resulting analysis of the observed diffuse polarization. These data clearly show multiple polarized features that overlapped in position but are separated slightly in Faraday depth, proving that high Faraday depth resolution is needed to unambiguously identify such features. I also consider the lack of sensitivity to Faraday thick structures (described in 1.4.3) in RM synthesis and how, in terms of ISM structure, this can be used to constrain the possible sources of the observed diffuse polarization. I combine these theoretical considerations, the IC342 observations, and auxiliary data on the ISM in that field to produce a model of the diffuse polarized features and their Faraday rotation, specifically showing how the emission in that field can be attributed to nearby clouds of neutral gas (WNM).

Chapter 3 is a short report on commissioning work I performed as a member of the LOFAR Magnetism Key Science Project (MKSP). One of the necessary steps in calibrating data for Faraday tomography is to remove the Faraday rotation contribution of the Earth's ionosphere, in order to isolate the astrophysical Faraday rotation. I assisted with commissioning tasks to test a new software package for performing this calibration and to evaluate the effectiveness of the ionospheric Faraday rotation correction. This software was used in the data reduction carried out in the other chapters.

In Chapters 4 and 5 I present the work done on applying Faraday tomography to 60 LOFAR observations supplied from the LOFAR Two-Meter Sky Survey [LOTSS, Shimwell et al., 2017]. Chapter 4 focuses on the data processing performed to extract measurements of the unresolved polarized sources present in the data, and analysis of these measurements. This work was done as an investigation on the feasibility and usefulness of a possible survey of background polarized sources, with an emphasis on testing algorithms for making reliable measurements of the polarization properties of these sources. I present a catalog of polarized point sources seen in the LOTSS test region, compare this catalog against previous measurements made at higher frequencies, and demonstrate some areas of investigation for which this catalog is well suited.

Chapter 5 focuses on the diffuse polarized emission observed in the same data. I present the first LOFAR Faraday depth cube mosaic, made by combining the Faraday depth cubes made from each of the 60 observations into a single cube covering over 400 square degrees. The features in this cube are identified and discussed, with an emphasis on the Faraday depth gradients observed. I show how, in previously published models for beam depolarization, these gradients are expected to be strongly depolarized, and show that for simple, but reasonable, assumptions the depolarization may be much less significant than expected. I also compare the diffuse polarized emission to several tracers of ISM structure, and find an intriguing correlation with a neutral hydrogen filament in part of the field.

Chapter 6 summarizes the work and results in this thesis, discusses some questions raised by this work, and suggests directions for follow-up research.

Chapter 2

Faraday tomography of the local interstellar medium with LOFAR: Galactic foregrounds towards IC342

C.L. Van Eck, M. Haverkorn, M.I.R. Alves, R. Beck, A.G. de Bruyn, T. Enßlin, J.S. Farnes, K. Ferrière, G. Heald, C. Horellou, A. Horneffer, M. Iacobelli, V. Jelić, I. Martí-Vidal, D.D. Mulcahy, W. Reich, H.J.A. Röttgering, A.M.M Scaife, D.H.F.M. Schnitzeler, C. Sobey, S.S. Sridhar

A&A, Vol 597, id.A98, 2017

Abstract

Magnetic fields pervade the interstellar medium (ISM), but are difficult to detect and characterize. The new generation of low-frequency radio telescopes, such as the Low Frequency Array (LOFAR: a Square Kilometre Array-low pathfinder), provides advancements in our capability of probing Galactic magnetism through low-frequency polarimetry. Maps of diffuse polarized radio emission and the associated Faraday rotation can be used to infer properties of, and trace structure in, the magnetic fields in the ISM. However, to date very little of the sky has been probed at high angular and Faraday depth resolution.

We observed a 5° by 5° region centred on the nearby galaxy IC342 ($\ell = 138.2°$, $b = +10.6°$) using the LOFAR high band antennae in the frequency range 115–178 MHz. We imaged this region at $4\farcm5 \times 3\farcm8$ resolution and performed Faraday tomography to detect foreground Galactic polarized synchrotron emission separated by Faraday depth (different amounts of Faraday rotation). Our Faraday depth cube shows a rich polarized structure, with up to 30 K of polarized emission at 150 MHz. We clearly detect two polarized features that extend over most of the field, but are clearly separated in Faraday depth.

Simulations of the behaviour of the depolarization of Faraday-thick structures at such low frequencies show that such structures would be too strongly depolarized to explain the observations. These structures are therefore rejected as the source of the observed polarized features. Only Faraday thin structures will not be strongly depolarized at low frequencies; producing such structures requires localized variations in the ratio of synchrotron emissivity to Faraday depth per unit distance. Such variations can arise from several physical phenomena, such as a transition between regions of ionized and (mostly) neutral gas.

We conclude that the observed polarized emission is Faraday thin, and propose that the emission originates from two mostly neutral clouds in the local ISM. Using maps of the local ISM to estimate distances to these clouds, we have modelled the Faraday rotation for this line of sight and estimated that the strength of the line of sight component of magnetic field of the local ISM for this direction varies between -0.86 and $+0.12$ μG (where positive is towards the Earth). We propose that this may be a useful method for mapping magnetic fields within the local ISM in all directions towards nearby neutral clouds.

2.1 Introduction

The interstellar medium (ISM) contains gas in a variety of physical conditions (cold molecular, cold and warm neutral atomic, warm and hot ionized), a population of relativistic particles (cosmic rays), dust, and an ambient magnetic field. Many aspects of the ISM are difficult to study because most of the tracers for the various components are difficult to measure, often require ancillary data, and often give integrated or average values for the physical parameters being estimated. The detection and estimation of magnetic fields in the ISM introduces the additional complication that the observational tracers also depend on one of the matter components.

Synchrotron polarization and Faraday rotation are often measured together to provide complementary information on interstellar magnetic fields. Synchrotron emission (and its polarization) traces the component of the magnetic field perpendicular to the line of sight but also depends on the cosmic ray properties. Faraday rotation provides information on the parallel component of the magnetic field along the line of sight but also depends on the thermal electron density.

Diffuse synchrotron polarization at low frequencies has shown a great deal of structure that has no counterpart in total intensity [e.g. Wieringa et al., 1993; Gray et al., 1998; Haverkorn et al., 2004]. This structure can be introduced both by fluctuations in the polarization at the emitting source, and by variations in the amount of Faraday rotation along the line of sight. As a result, these structures can provide unique information on the magnetic fields in the ISM.

The amount of information that can be extracted from polarization observations has been greatly increased by the development of the rotation measure (RM) synthesis technique [Burn, 1966; Brentjens & de Bruyn, 2005], which can separate polarized emission by the degree of Faraday rotation it has experienced. The amount of Faraday rotation (i.e. the extent to which the polarization position angle has rotated between the emission source and the receiver) is the product

of the observing wavelength squared (λ^2) and the Faraday depth (ϕ) which is defined as

$$\phi(d) = 0.812 \text{ rad m}^{-2} \int_d^0 \left(\frac{n_\text{e}}{\text{cm}^{-3}}\right) \left(\frac{\vec{B}}{\mu\text{G}}\right) \cdot \left(\frac{\vec{dl}}{\text{pc}}\right), \tag{2.1}$$

where n_e is the number density of free electrons, $\vec{B}$ is the magnetic field, $\vec{dl}$ is a differential element of the radiation path, and the integral is taken over the line of sight from a distance d to the receiver. Polarized emission detected at different Faraday depths can be used to reconstruct the magnetic field along the line of sight. This technique can be applied to a region of the sky to produce data cubes showing the distribution of diffuse polarized emission in position on the sky and in Faraday depth. We refer to the production and analysis of these data as Faraday tomography. The resolution in Faraday depth depends on the range of λ^2 covered by the observations, so observations at low frequencies and with high fractional bandwidth give better resolution.

Faraday tomography of the Milky Way has been done previously with several datasets from the Westerbork Synthesis Radio Telescope (WSRT) [e.g. Brentjens, 2011; Iacobelli et al., 2013], the Low Frequency Array (LOFAR) [Jelić et al., 2014, 2015], and the Murchison Widefield Array [Lenc et al., 2016], as well as at higher frequencies with the 26m telescope at the Dominion Radio Astrophysical Observatory [Wolleben et al., 2010]. Many of these studies have been focused on characterizing features which appear in polarized emission and have no apparent counterpart in total intensity (which can occur when the total intensity emission is spatially smooth and is filtered out by an interferometer). Some studies have proposed models for the Faraday rotation of the diffuse polarized emission [e.g. the screen and bubble model of Iacobelli et al., 2013], identifying regions of emission and Faraday rotation along the line of sight and estimating the magnetic field strengths, electron densities, and distances associated with the Faraday rotation.

In this paper, we report on LOFAR observations of Galactic diffuse polarized emission towards the nearby galaxy IC342 and the results of performing Faraday tomography on these observations. In Sect. 2.2 we describe the observations and their processing. We present the resulting Faraday depth cubes and describe the features observed in Sect. 2.3. We follow this with a model of the magnetic field along these lines of sight in Sect. 2.4 and discuss the interpretation and limitations of this model in Sect. 2.5. Our conclusions are summarized in Sect. 2.6.

2.2 Observations and data processing

Our data consist of two observations with the LOFAR high-band antennae [HBA, for full details on LOFAR's design see van Haarlem et al., 2013b]. The first observation was taken from 2013-02-02/15:50 to 20:53 UTC, while the second was taken from 2013-03-13/22:21 to 2013-03-14/03:56 UTC. The full LOFAR 'Dutch array', consisting of 48 core and 13 remote stations, was used in the HBA_DUAL_INNER mode. Each observation consisted of 19 pairs of pointings, with each pair containing a 120-second observation of the flux calibrator, 3C147 ($\alpha = 05^\text{h}42^\text{m}36^\text{s}1$, $\delta = +49°51'07''$), followed by a 720-second observation of the target field, centred on galaxy IC342 ($\alpha = 03^\text{h}46^\text{m}48^\text{s}5$, $\delta = +68°05'46''$; $\ell = 138.1726°$, $b = +10.5799°$). The observed bandwidth was divided into 324 subbands, each with a bandwidth of 0.1953 MHz further divided into 64 channels,

providing contiguous frequency coverage from 114.952 MHz to 178.233 MHz. An integration time of one second was used for all pointings, resulting in a raw data volume of about 40 TB.

We performed radio frequency interference (RFI) detection and flagging using the AOflagger algorithm [Offringa et al., 2012], which was applied to the data in three passes: on the raw data, after initial averaging, and after amplitude calibration. Before the initial RFI flagging, we flagged the two lowest and two highest channels in each subband, as these channels are generally affected by the bandpass edges of the polyphase filter. After the initial RFI detection and flagging, we averaged the data in time and frequency to 6 seconds and 8 channels per subband (24.413 kHz bandwidth per channel), to reduce the data volume to approximately 1 TB. The possibility of contamination by the bright 'A-team' sources (Cas A, Cyg A, Vir A, Her A, and Tau A) was checked by simulating the contribution to the visibilities using the Blackboard Selfcal System [BBS, Pandey et al., 2009] and found to be minor except for a few baselines at particular times. The 'demixing' algorithm of van der Tol et al. [2007] was not used, and those baselines and time intervals that showed significant A-team signal were flagged. Before calibration, the stations CS013HBA0 and CS013HBA1 were completely flagged as the antennas in these stations were rotated with respect to the rest of the array.

The calibration target, 3C147, was calibrated with the flux model from Scaife & Heald [2012], using the BBS software, independently for each subband and two minute calibration pointing. The resulting gain amplitude solutions were interpolated in time and applied to the target field. For the phase calibration of the target field, a sky model was made using the LOFAR global sky model (GSM), which was made by combining the catalogues from the NRAO VLA Sky Survey [Condon et al., 1998, NVSS], the Westerbork Northern Sky Survey [Rengelink et al., 1997, WENSS], and the VLA Low-Frequency Sky Survey redux [Lane et al., 2014, VLSSr]. Phase calibration was performed on groups of nine subbands, to improve the signal-to-noise ratio of the solutions.

No self-calibration was applied to the data. We found that the direction-independent phase calibration produced good results for the shorter baselines across most of the target field; we achieved the best images by removing the remote stations more distant from the LOFAR core. We chose to phase calibrate and image using only the core stations and the nearest three remote stations (RS305, RS503, and RS205).

To accurately determine the Faraday depths, we removed the contribution of the ionosphere to the Faraday rotation, using the RMextract software[1] written by Maaijke Mevius. This software calculates the ionospheric contribution by using the World Magnetic field Model (WMM)[2], maps of the total free electron content of the ionosphere from the Center for Orbital Determination in Europe (CODE)[3], and a model for the ionosphere to predict the Faraday rotation of the ionosphere for a given LOFAR observation. The observations were derotated by the predicted amount using the BBS software. The estimated systematic uncertainty in the Faraday depth correction is approximately 0.1–0.3 rad m^{-2} [Sotomayor-Beltran et al., 2013].

Before imaging, the baselines between each pair of HBA sub-stations (e.g. CS002HBA0 and CS002HBA1) were removed, as these were observed to have significant instrumental cross-talk. Imaging was performed with the AWimager [Tasse et al., 2013a]. Images were made in Stokes Q

[1] https://github.com/maaijke/RMextract/
[2] https://www.ngdc.noaa.gov/geomag/WMM/DoDWMM.shtml
[3] http://aiuws.unibe.ch/ionosphere/

and U for each channel, using robust weighting of 1.0 and including only baselines between 10 and 800λ. Station beam correction was applied within AWimager, and due to very low signal-to-noise in each image no cleaning was done. This produced a frequency independent resolution of $4\farcm5 \times 3\farcm8$. This was done for all 2592 channels in the data set. After imaging, 110 channels were identified by manual inspection as being badly affected by noise or instrumental effects and were removed. The standard deviation of flux density at the center of each image was about 12 mJy PSF^{-1} and almost independent of frequency, giving a theoretical band-averaged rms noise level of 0.24 mJy PSF^{-1} at the center of the field. However, these values contain contributions from both the per-channel noise and the signal present in each channel, and so represent an over-estimate of the true noise in the data.

In addition, a Stokes I image was produced to search for polarized point sources. This image was produced using the full bandwidth and time range of the observations, and used the same baseline selection as the polarization images. The resulting image is shown in Fig. 2.1. A detailed analysis of the Stokes I emission from IC342 is deferred to a future paper.

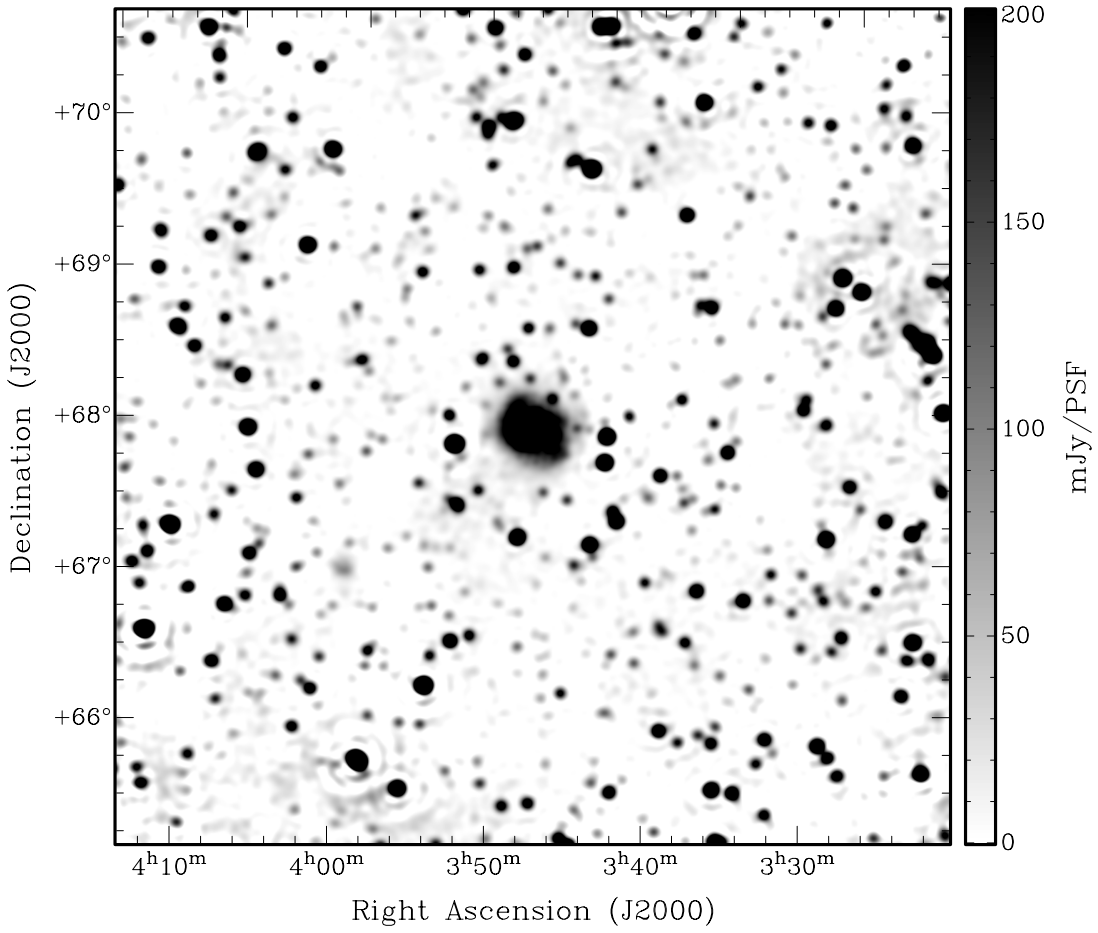

Figure 2.1: Total intensity map of the IC342 field. The nearby spiral galaxy IC342 appears prominently in the center, the giant double radio galaxy WNB 0313+683 appears on the right, and the dwarf galaxy UGCA 86 ($\alpha = 03^{\rm h}59^{\rm m}49^{\rm s}4, \delta = +67°08'38''$) appears faintly below and left of center. In Galactic coordinates, the center of the field is at $\ell = 138.2°$, $b = +10.6°$. The resolution is $4\farcm5 \times 3\farcm8$.

The pyRMsynth[4] software package was used to perform the Faraday tomography. The frequency coverage of the data produced a Faraday depth resolution of 0.9 rad m^{-2}, a maximum scale of 1.1 rad m^{-2}, and sensitivity to Faraday depths in the range $|\phi| < 2200$ rad m^{-2}, as calculated from equations 61-63 of Brentjens & de Bruyn [2005]. However, these equations are only applicable with the criterion that $|\phi|\Delta\lambda^2 \ll 1$, which is only satisfied for $|\phi| \ll 350$ rad m^{-2} at the lowest frequency. Since our field is outside of the Galactic plane, we do not expect emission at large Faraday depths, so this criterion should not be violated. The small difference between the resolution and the maximum scale means that we are not able to resolve Faraday depth structure; features broader than the maximum scale will be strongly depolarized and thus filtered out, while features narrower than the resolution will appear as unresolved peaks. The consequences of this are discussed in Sect. 2.4.1 and Appendix 2.A.

Channel weights were applied inside pyRMsynth, and were made equal to the inverse square of the rms noise in each image (analogous to natural weighting in radio interferometry). Uniform channel weighting was also tested and found to produce insignificant differences in the final Faraday cubes. The restoring beam used in RM-cleaning was a Gaussian fitted to the rotation measure spread function (RMSF, the response function introduced by limited sampling in the wavelength domain), with a fitted standard deviation of 0.37 rad m^{-2} (corresponding to a FWHM of 0.87 rad m^{-2}, in agreement with the theoretical resolution above). RM-CLEAN [Heald et al., 2009] was applied to each cube, down to a threshold of 2 mJy PSF^{-1} RMSF^{-1}. No correction for the spectral index of the emission was applied, as the diffuse flux was not detected in total intensity to determine the appropriate spectral index; this may introduce a small error in the polarized intensities of order 2–5% [Brentjens & de Bruyn, 2005]. Cubes were also made without applying RM-CLEAN, and found to have no significant differences to those with RM-CLEAN.

During calibration, polarization leakage from Stokes I into Stokes Q and U was not corrected for, as at the time of processing no method had been developed to determine this correction and the effects on the data were judged minor enough to not merit reprocessing. The leakage produces apparent polarization at the location of all Stokes I sources. The leakage is frequency-independent, so the spurious polarization appears at 0 rad m^{-2} in Faraday depth. However, the ionospheric Faraday rotation correction causes all the polarization to be shifted in Faraday depth by the opposite of the predicted ionospheric Faraday depth, to remove the ionospheric contribution. By doing so, the astrophysical signal was moved to the correct Faraday depth, and the instrumental polarization was moved away from 0 rad m^{-2}. Since the ionospheric correction was time-variable, the leakage is 'corrected' to different values for each time. In the resulting Faraday cubes the leakage is then smeared out over a range of Faraday depths corresponding to the (negative of the) range of values of the ionospheric correction. For these data, this correction ranged from 0.2 to 1.1 rad m^{-2}, so the instrumental polarization was shifted to between -1.1 and -0.2 rad m^{-2} and, due to convolution with the RMSF, appears in the cube slices between approximately -1.5 and $+0.5$ rad m^{-2}.

Two Faraday depth cubes were produced: a finely-sampled cube, covering Faraday depths from -25 to 25 rad m^{-2} in steps of 0.25 rad m^{-2}, and a more coarsely-sampled cube from -100 to 100 rad m^{-2} in steps of 0.5 rad m^{-2}. The catalogue of Taylor et al. [2009] contains

[4]https://github.com/mrbell/pyrmsynth

polarized sources with rotation measures between -70 rad m^{-2} and $+23$ rad m^{-2} in this region of the sky, so we did not expect any diffuse emission or point sources with Faraday depths beyond ± 100 rad m^{-2}. The final noise in the cubes was determined on a pixel-by-pixel basis by masking out Faraday depths between -20 and $+20$ rad m^{-2} (where most of the signal was expected), constructing a histogram of the polarized intensity distribution for the remaining (empty) Faraday spectrum, and fitting a Rayleigh distribution with a least-squares solver. The Rayleigh distribution represents the distribution of polarized intensity when the distributions of Stokes Q and U are both Gaussian. We found that this method gave similar values to fitting Gaussians to the noise distributions in Q and U, with the advantage of using all the data in a single fit. The resulting noise (expressed as Rayleigh σ parameter, which is equivalent to the Gaussian σ_{QU} of the Stokes Q and U distributions) was position dependent (due to beam correction), and ranged from 0.2 mJy PSF^{-1} RMSF^{-1} near the center of the field (in agreement with the band-averaged noise estimate above) to approximately 2 mJy PSF^{-1} RMSF^{-1} in the lower left and upper right corners (3.5 degrees from the phase center). At the band center, 146.6 MHz, the conversion from flux density to brightness temperature is 0.924 K (mJy PSF^{-1})$^{-1}$, from equations 9-25 and 9-26 of Wrobel & Walker [1999].

2.3 Faraday depth cubes

In this section we present and describe the resulting Faraday depth cubes. Figs. 2.2 through 2.5 show images of polarized intensity extracted from the Faraday cubes, which were selected to show the interesting features in the cube. Fig. 2.6 shows some sample Faraday depth spectra for different positions in the cube.

In broad terms, the observed polarized emission can be divided into four components: instrumental polarization leakage, appearing between -1.5 rad m^{-2} and $+0.5$ rad m^{-2}, as discussed in Sect. 2.2; unresolved polarized sources, most likely background radio galaxies, observed between -30 and -8 rad m^{-2}; a diffuse emission feature, with a complex morphology that covers most of the field, between -7 rad m^{-2} and $+3$ rad m^{-2}, with a typical polarized brightness of 30 K; and a second, fainter, diffuse emission feature, with a different morphology, between $+1.5$ rad m^{-2} and $+11$ rad m^{-2}, with a typical polarized brightness of 10 K.

2.3.1 Polarized background sources

Three unresolved polarized background sources were detected in the 5° by 5° field. Two of these coincide with locations in the double radio galaxy WNB 0313+683, with different Faraday depth values and slightly different positions. The third is a single radio source, NVSS J041445+690108. All three were matched with sources in the Taylor et al. [2009] RM catalogue. Table 2.1 gives the measured parameters for these sources.

A consequence of the instrumental polarization is that any polarized sources with Faraday depths between -1.5 and $+0.5$ rad m^{-2} cannot be separated from the leakage, and currently cannot be identified. Of the 45 sources in this field with catalogued RMs from Taylor et al. 2009, there is only one source with an RM value within this range (11 additional sources are within 1σ of this range). Since we detected only 3 polarized sources in the accessible Faraday depth range

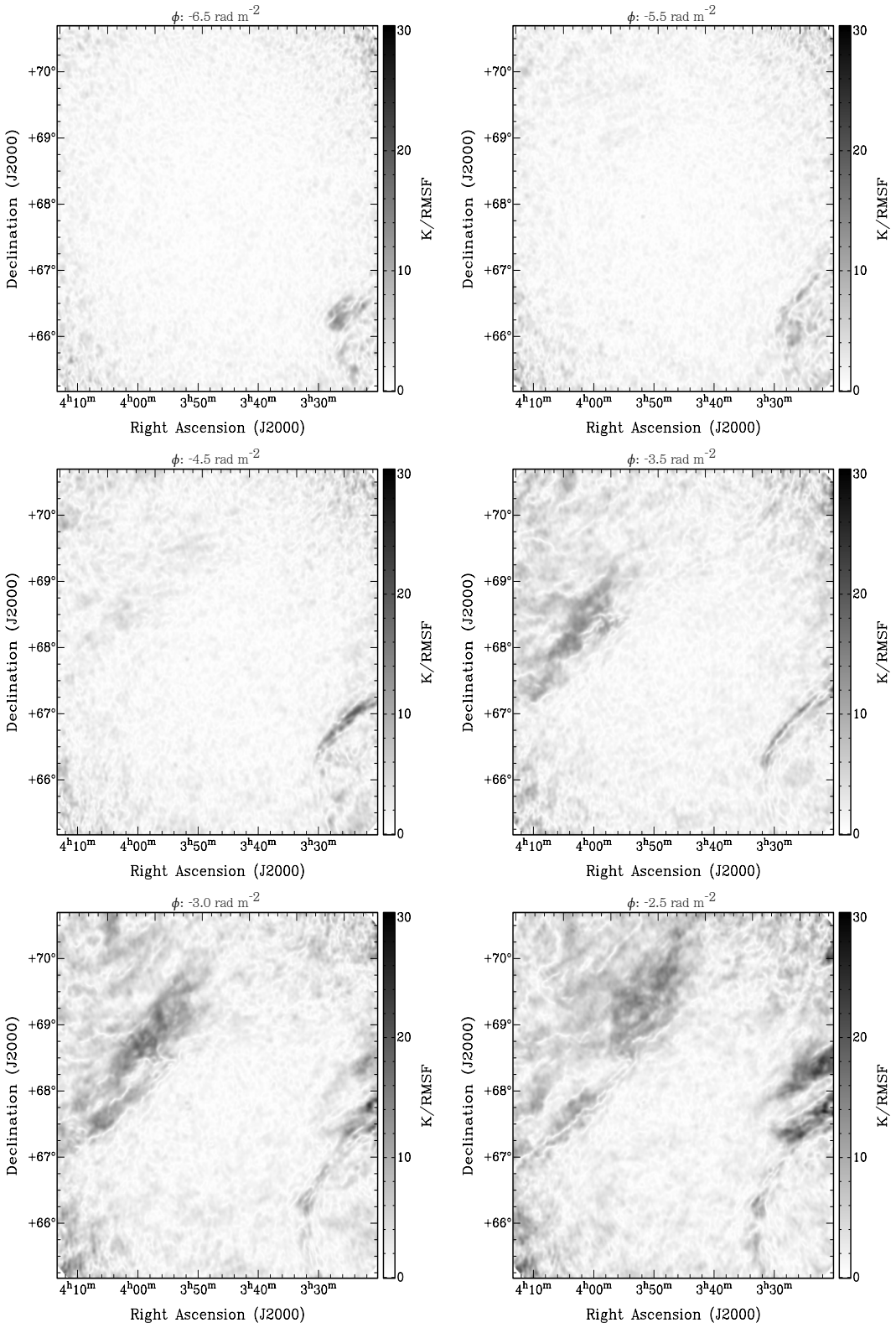

Figure 2.2: Selected slices from the finely-sampled Faraday depth cube, showing the polarized intensity at different Faraday depths from -6.5 rad m^{-2} to -2.5 rad m^{-2}. A bright polarized diffuse feature can be seen entering the field from the top left and bottom right corners. The resolution is $4\farcm5 \times 3\farcm8$.

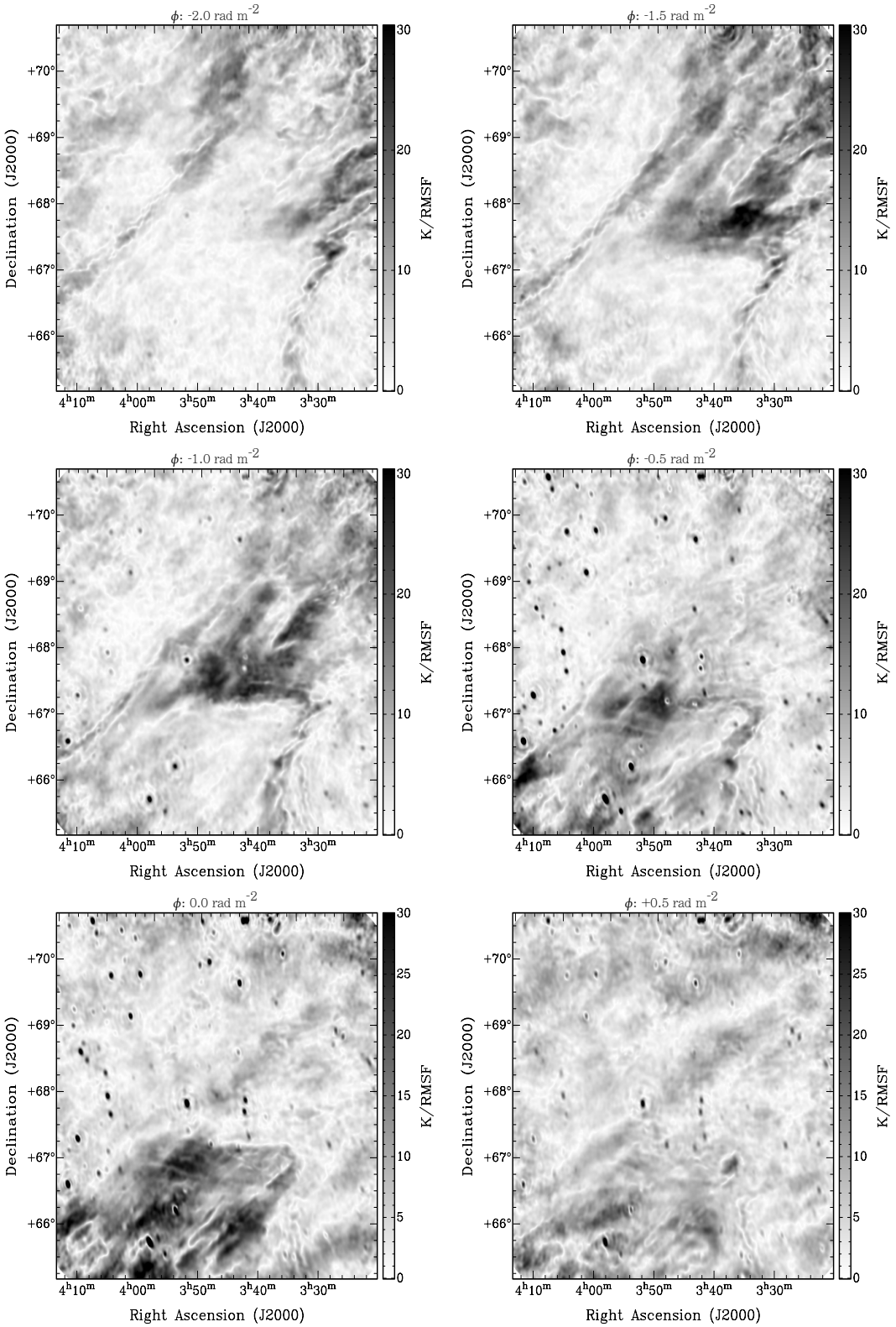

Figure 2.3: As Fig. 2.2, more slices from the same cube, from -2 rad m^{-2} to $+0.5$ rad m^{-2}. The bright polarized feature can be seen to move through the center of the frame and towards the lower left corner. The polarization leakage from Stokes I into Q and U can be seen at Faraday depths between -1 and $+0.5$ rad m^{-2}.

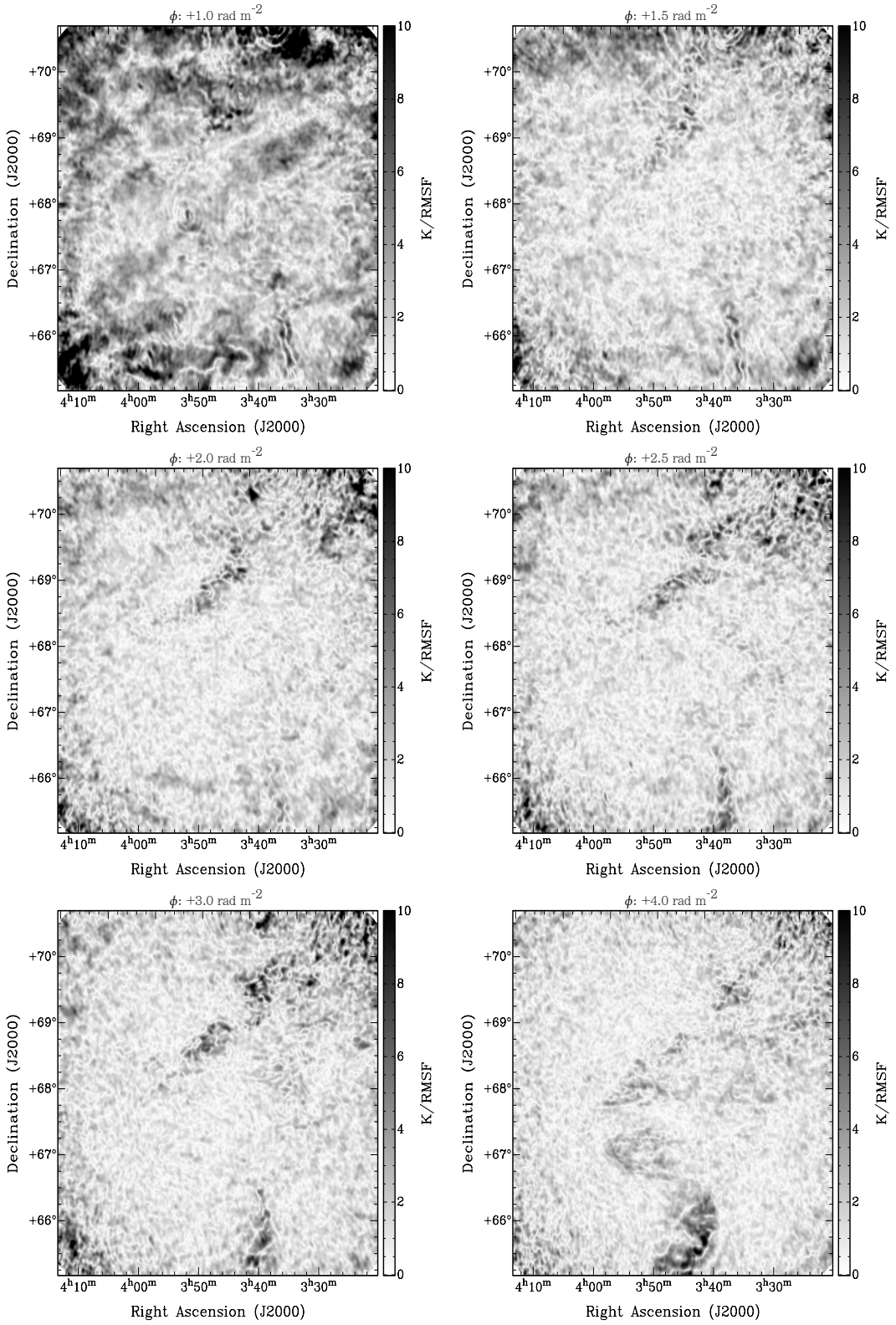

Figure 2.4: As Fig. 2.2, more slices from the same cube, from +1 rad m^{-2} to +4.0 rad m^{-2}. The intensity scale has been adjusted to show the faint emission more clearly. The bright polarized feature fades away, and a second, fainter feature emerges in the top and bottom of the field, moving towards the lower left.

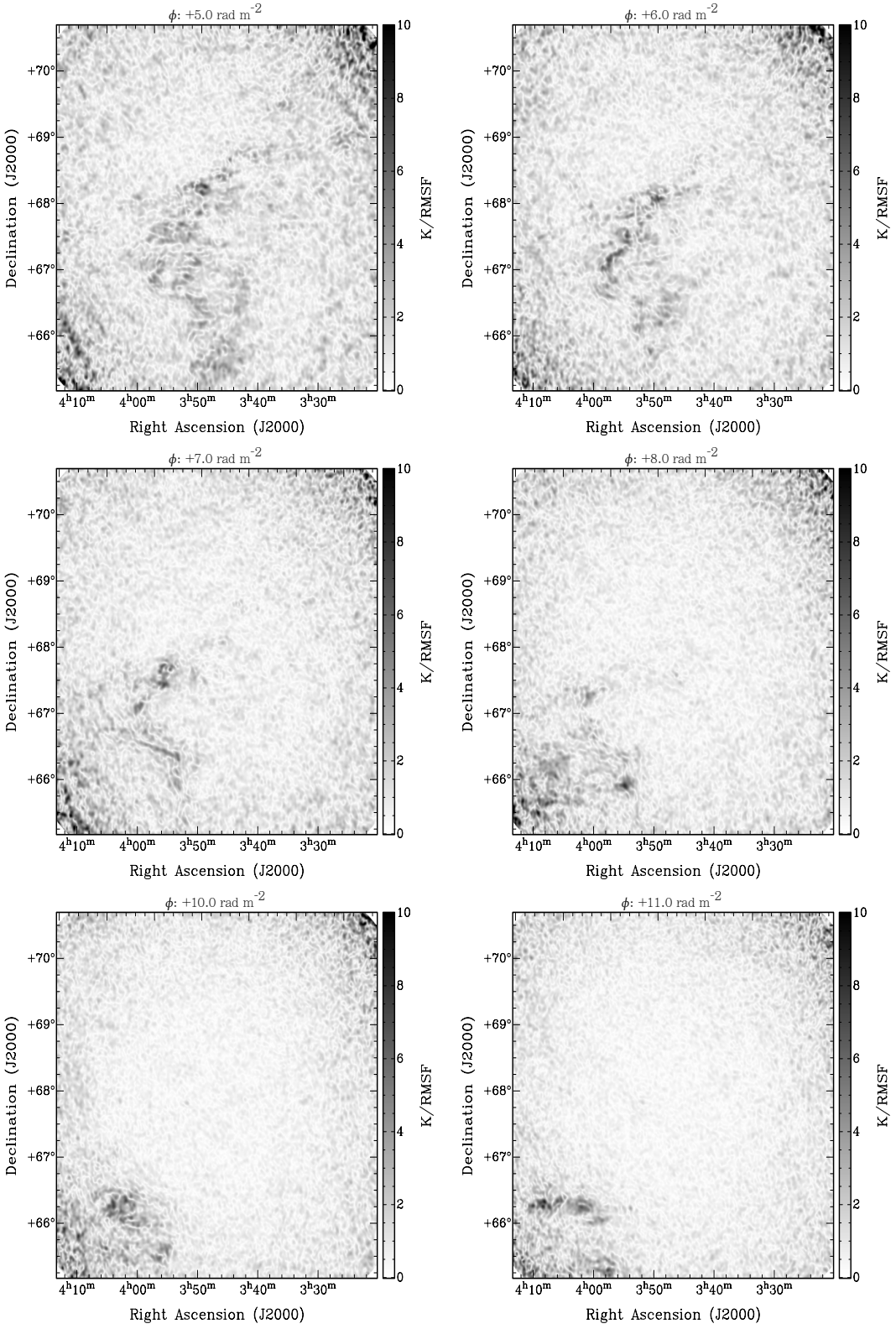

Figure 2.5: As Fig. 2.2, more slices from the same cube, from +5 rad m^{-2} to +11 rad m^{-2}. The intensity scale has been adjusted to show the faint emission more clearly. The faint polarized feature moves through the center towards the lower left.

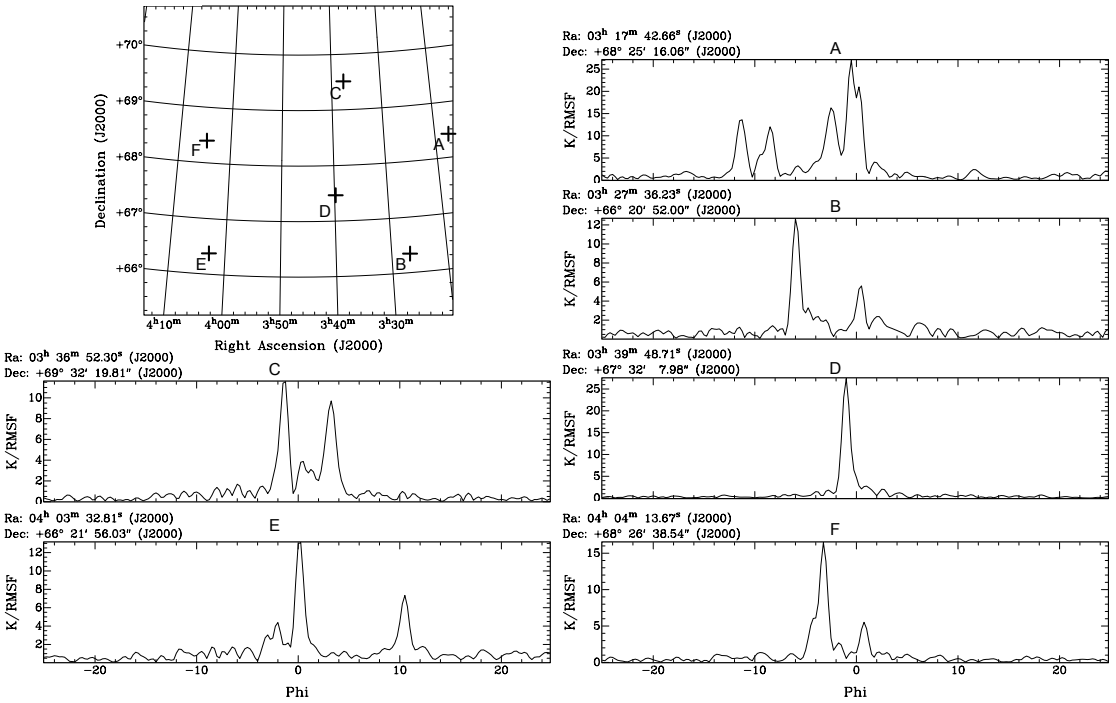

Figure 2.6: Faraday depth spectra for selected lines of sight. The top left panel shows the locations of the lines of sight. Panel A is at the location of the polarized emission from the giant radio galaxy WNB 0313+683, which shows two Faraday depth components at −11.4 and −8.6 rad m^{-2} (which overlap in angular position at this resolution), a Stokes I leakage feature at −0.5 rad m^{-2}, and a diffuse emisison peak at −3 rad m^{-2}. Other panels are at locations containing only diffuse emission, and show either one (D) or two (B,C,E,F) clear peaks.

Table 2.1: Measured parameters of the polarized background sources

$\alpha_{J2000}{}^a$ [h m s]	$\delta_{J2000}{}^a$ [d m s]	I(150 MHz)^b [mJy PSF^{-1}]	PI(150 MHz)^c [mJy PSF^{-1}]	RM^d [rad m^{-2}]	NVSS RM ^{e} [rad m^{-2}]
04 14 45±2	69 01 14±9	562± 5	8.0±0.5	−28.6 ± 0.05	−32.9±15.8
03 17 47±1	68 24 54±6^f	1740±10	15.4±0.7	−11.4± 0.05	−12.9± 4.9
03 17 40±1	68 24 03±6^f	1320±10	14.6±0.7	−8.6± 0.05	−12.8± 4.7

Notes: $^{(a)}$ Position from fitting the source in polarized intensity. $^{(b)}$ Observed intensity at the pixel closest to the fitted position. $^{(c)}$ Polarized intensity, found by fitting a 3D Gaussian to the source. $^{(d)}$ Rotation measure, found by fitting a 3D Gaussian to the source. The ionospheric Faraday rotation correction introduces an additional systematic error of about 0.1–0.3 rad m^{-2}. $^{(e)}$ Rotation measure from the catalogue of Taylor et al. [2009]. $^{(f)}$ These sources are at the position of WNB 0313+683.

of our data, out of the 44 known polarized sources in this range, we conclude that it is unlikely that another polarized source is hidden inside the instrumental leakage signal.

Due to the small number of sources, we defer a detailed analysis of these polarized sources to a planned follow-up paper, which will use this and other LOFAR observations to construct a much larger and statistically useful sample of low-frequency polarized sources.

No obvious polarization was observed at the location of IC342, other than the instrumental polarization leakage from Stokes I. A careful upper limit on the polarization of IC342 at this frequency is deferred to a future paper where the data will be reprocessed at full resolution, to reduce the possible effects of beam depolarization.

2.3.2 Diffuse polarized emission

We divide the diffuse polarized emission into two features, based on the morphology and range of Faraday depths. Both have similar large-scale structure in Faraday depth, but are displaced from each other by several rad m^{-2}. The first feature covers a Faraday depth range between about -7 and $+3$ rad m^{-2} (Figs. 2.2 to 2.4), and consists of diffuse emission across the entire field. The lowest Faraday depths occur at the lower right and upper left corners, with a gradient towards the center and upper right. Around Faraday depth -2 to -1 rad m^{-2} the center and upper right become filled with emission, and two filamentary 'arms' extend to either side of the lower left corner. From -1 to $+1$ rad m^{-2} there is a strong gradient, with the emission sharply transitioning from the upper right to the lower left. At Faraday depths greater than $+1$ rad m^{-2}, there is some remaining diffuse emission in the lower left corner, which remains present to at least $+3$ rad m^{-2}, but it is difficult to determine where exactly the emission ends as the edges of the cube are significantly affected by noise (due to the beam correction). The morphology of this emission matches up very well with the observations of Iacobelli et al. [2013], which overlap the lower right corner of our field.

This emission feature also contains a number of long, nearly straight depolarization canals. These canals appear to have a preferred axis (towards the lower-left and upper-right corners), which appears to be aligned well with the Galactic plane (lines of constant Galactic latitude also run from the lower-left to the upper-right). Since we did not use CLEAN on the individual Q and U channel images, these canals are not artifacts of the type described by Pratley & Johnston-Hollitt [2016], but reflect real structure in the emission (albeit affected by the resolution of the observations). Further investigation into the significance and possible interpretations of this are left for a follow-up analysis.

The second, fainter, diffuse feature covers a significant fraction of the field at higher Faraday depths, from $+1.5$ to $+11$ rad m^{-2} (Fig. 2.4 and 2.5). This feature has a similar trend to the first: at the lowest Faraday depths it occurs in the top left and lower right corners, with a gradient towards the center and upper right with increasing Faraday depth values. At Faraday depths between $+3.5$ and $+5$ rad m^{-2} it can be seen to fill much of the center and upper right of the frame, and transitions sharply towards the lower left between $+5$ and $+11$ rad m^{-2}. This feature shows very similar behaviour in the Faraday depth gradients to the first, but the structure of the emission (i.e. extent of emission, and locations of bright regions and canals) is different between the two. This suggests that the gradient is the result of a large-scale foreground Faraday-rotating

screen in front of both emission features, while the structure in the polarized intensity is unique to each source of diffuse polarized emission.

One concern when interpreting Faraday spectra is the risk of mis-identifying instrumental artifacts as real features. This can occur, for example, when the RMSF sidelobes of two emission features interact to produce a third, artificial feature. We conclude that this is not the case for the weaker emission feature we see here, and also that the fainter feature is not a sidelobe of the brighter feature, for three reasons. Firstly, through most of the field, there is no second bright feature that would mix with the brighter diffuse emission feature. It is possible that the instrumental leakage and the real emission could mix and produce an apparent feature in the spectrum, but this would be more likely to occur at Faraday depths between the real emission and the leakage, not at higher Faraday depths (an interaction like this between the two emission features could explain the small, 3 K RSMF^{-1} peaks seen around +1 rad m^{-2} in spectrum C of Fig. 2.6). Also, the leakage is mostly confined to the point sources, and would not be able to produce a spurious diffuse feature. Secondly, the first sidelobes in the RMSF are separated from the main lobe by $\pm$1.2 rad m^{-2}, while the two diffuse emission features are observed to be separated by 4–10 rad m^{-2}. At this separation, the RMSF sidelobes have a strength between 6% and 4% of the main peak, which is too small to explain the observed intensity of the second feature. Thirdly, the morphology between the two emission features shows significant differences, which can not be easily explained if the two features are related by some instrumental effect. For these reasons, we conclude that the fainter emission feature is real.

From the morphology, each diffuse feature appears to be a single emission region distributed across a range of Faraday depths: each represents a connected sheet in the three-dimensional volume of the Faraday cube, smoothly varying in Faraday depth as a function of position on the sky. In Fig. 2.7 we show the Faraday depth and polarized intensity of each feature per pixel, by finding the peak polarized intensity in fixed Faraday depth ranges selected to pick out each feature. These maps demonstrate the same features observed in the individual slices: the two diffuse features have distinctly different morphologies in emission, but similar trends in Faraday rotation.

2.4 Modelling the diffuse Galactic emission

In this section, we present a physical model that describes the main features of the diffuse emission described above. To do so, we first account for the effects of incomplete wavelength coverage on the Faraday spectrum, and then consider possible physical configurations that might produce the observations given these effects.

2.4.1 Properties of low-frequency RM synthesis

Since RM synthesis is a Fourier transform-like process, the reconstruction of the Faraday spectrum is affected by filtering due to incomplete sampling of the λ^2 domain. By analogy to radio interferometry, the dirty beam is represented by the RMSF, which is convolved with the actual Faraday spectrum to give the measured spectrum. The effects this has on the observed spectrum, especially the resulting limits to the information in a Faraday depth spectrum, have been studied

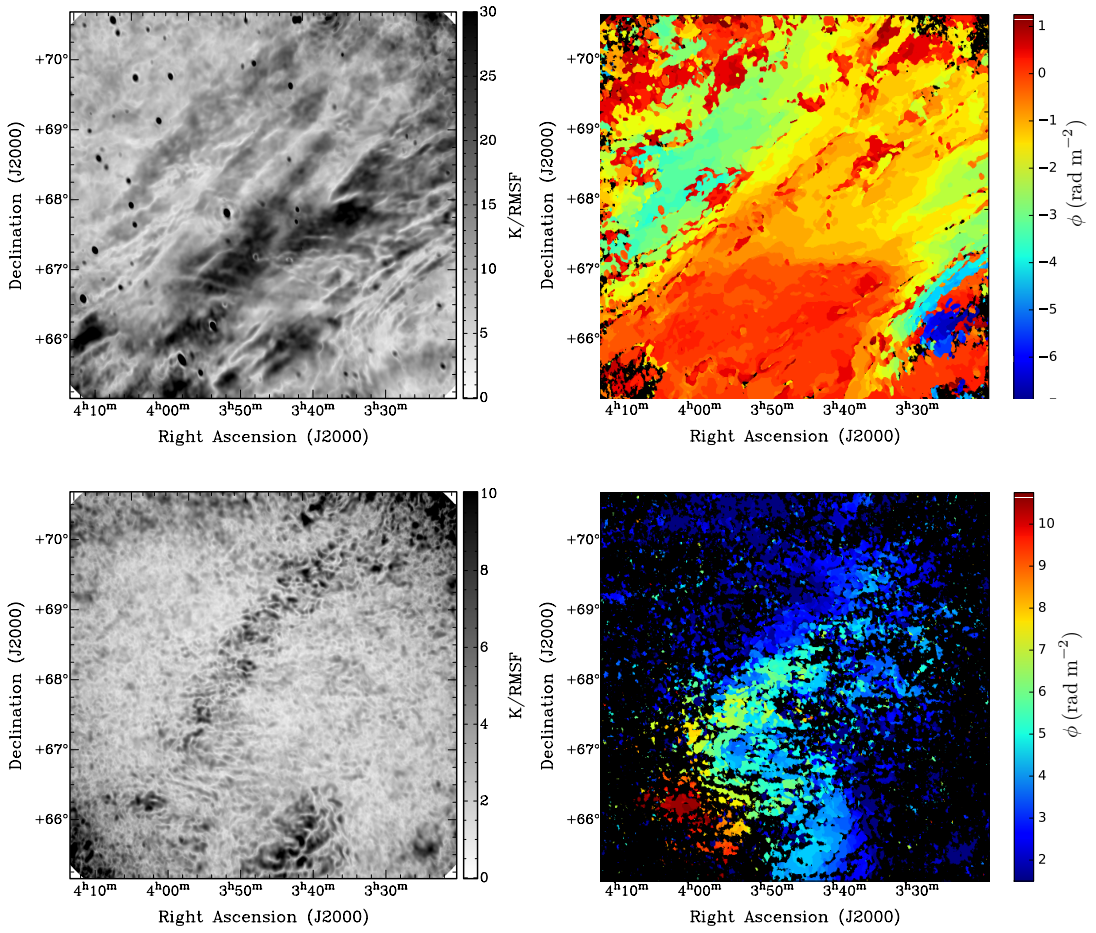

Figure 2.7: Left: Maps of the peak polarized intensity in selected Faraday depth ranges. Right: Maps of the Faraday depth of peak emission, for the same ranges in Faraday depth. Pixels with peak polarized intensity below 10 σ_{QU} are masked. Top panels: Faraday depths between -7 and $+1.5$ rad m^{-2}. Bottom panels: Faraday depths between $+1.5$ and $+11$ rad m^{-2}. The compact sources in the top panel are caused by the instrumental polarization.

by several authors [e.g. Brentjens & de Bruyn, 2005; Beck et al., 2012, and references therein]. One such effect, which becomes very constraining at low frequencies, is the loss of sensitivity to broad structures in the Faraday spectrum (which are often called Faraday thick features, although this term is often tied to the Faraday depth resolution of a given observation), directly analogous to how a lack of short baselines removes large-scale emission in interferometry. This can also be interpreted in terms of wavelength-dependent depolarization by considering the Fourier scaling property: making a feature broader in Faraday depth makes the transform of that function narrower in the λ^2 domain. Broader features in Faraday depth result in the polarization becoming more rapidly depolarized with increasing wavelength. We note that we are only discussing depth depolarization in an emitting and Faraday-rotating volume, and neglecting the effects of beam depolarization by a Faraday-rotating foreground, which has been studied by Tribble [1991]; Sokoloff et al. [1998]; Schnitzeler et al. [2015].

This behaviour is demonstrated in Fig. 2.8, where we simulate a Faraday-thin component (modelled as a Dirac delta function) and a Faraday slab [a top-hat or square pulse function in the Faraday spectrum, also called a Burn slab, Burn, 1966], using identical λ^2 coverage to our LOFAR observations. If the slab is significantly broader than the RMSF, the result is two peaks in the Faraday depth spectrum corresponding to the two edges of the tophat [Brentjens & de Bruyn, 2005; Heald et al., 2009; Beck et al., 2012]. The measured amplitude of these two peaks, given our λ^2 coverage, is 12% $\pm$ 1% of the true amplitude for all slabs thicker than about 2 rad m^{-2} (see Appendix 2.A for a discussion of this value).

The result of the filtering in the observed spectrum is that smooth features are removed while narrow features or sharp edges (i.e. narrower than the width of the RMSF) are preserved in low-frequency observations. This has significant implications on the physical conditions that can be observed. The key parameter that sets the amplitude in the Faraday spectrum, which we call A_ϕ, is the ratio of polarized synchrotron emissivity to Faraday depth per unit distance,

$$A_\phi = \frac{p_0 \left(\frac{\varepsilon}{\mathrm{K\,pc^{-1}}}\right)}{0.812 \left(\frac{n_\mathrm{e}}{\mathrm{cm^{-3}}}\right) \left(\frac{|B_\parallel|}{\mu\mathrm{G}}\right)} \mathrm{K\,(rad\,m^{-2})^{-1}}, \tag{2.2}$$

where the (total intensity) synchrotron emissivity, ε, depends on the cosmic ray electron density and the perpendicular magnetic field strength, and p_0 is the intrinsic polarization fraction of the emission. Sharp variations in this ratio, as a function of distance, are one method to produce narrow or sharp features in the Faraday spectrum; it is the presence of these sharp variations that causes the Faraday slab to appear as two peaks (one peak where it sharply increases from zero to the slab's amplitude, and the second where it decreases back to zero). These variations can take the form of positive or negative changes to the Faraday spectrum amplitude; a sharp decrease in A_ϕ will produce a feature indistinguishable from a sharp increase after the broad components are filtered out. Below, we consider some different physical processes that could produce such variations in A_ϕ.

A localized enhancement in the perpendicular magnetic field, such as that produced by the shock of an expanding supernova remnant, will create a region of enhanced synchrotron emission. The limited depth of such a shock could very naturally produce a sharp feature in the Faraday spectrum, which may not depolarize much if the total Faraday depth produced inside the shock

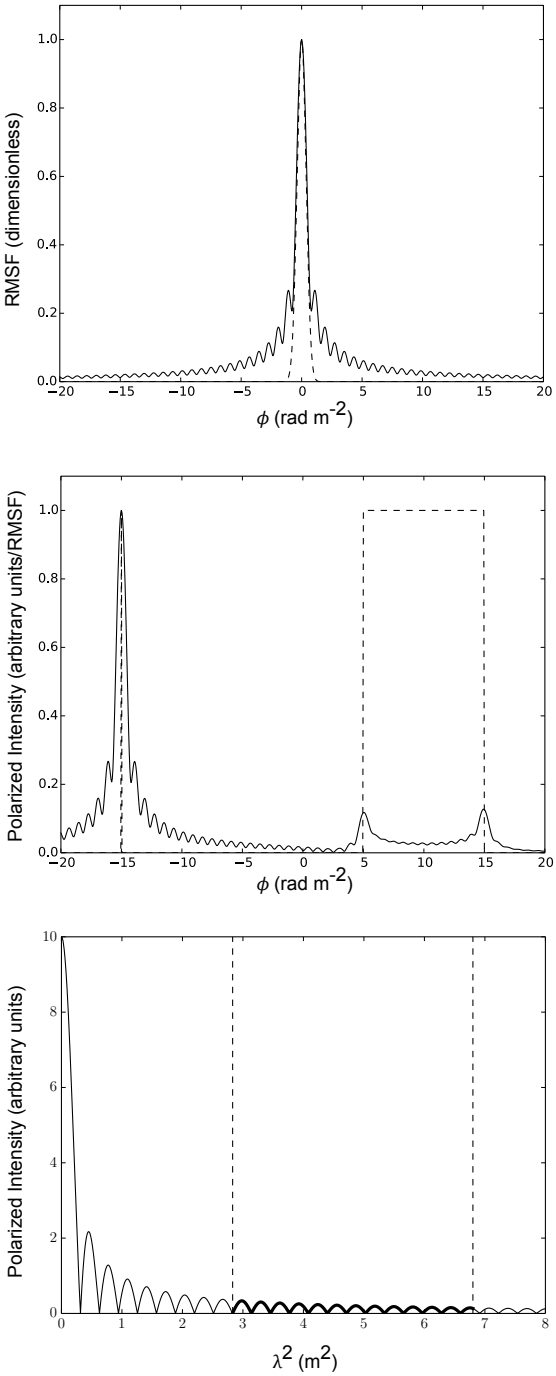

FIGURE 2.8: *Top:* Solid line: The RMSF for the frequency sampling of the IC342 observations. Dashed line: The Gaussian used as the restoring function in the RM CLEAN algorithm. *Middle:* Dashed line: Input spectrum containing a delta function at $\phi = -15$ rad m^{-2} and a Faraday slab between +5 and +15 rad m^{-2}, both with amplitude of 1. Solid line: Resulting spectrum using the frequency sampling of the IC342 observations. The Faraday slab is almost completely depolarized. *Bottom:* The polarization as a function of λ^2 for the Faraday slab above. The wavelength range of the LOFAR HBA is between the two dashed lines and the simulated signal in this range is marked in bold.

is less than the width of the RMSF. A diminishment in the perpendicular magnetic field would produce a similar (negative) feature in the Faraday spectrum.

The intrinsic polarization fraction, which is determined by how ordered the magnetic field is in the emitting region, may also vary and affect the Faraday spectrum amplitude. A region with a more ordered field or a more isotropic field will produce stronger or weaker polarization, respectively. A shock oriented perpendicular to the line of sight can make the magnetic field more ordered (parallel to the shock surface), giving the magnetic field in the region of the shock a preferred orientation and enhancing the polarization fraction.

The parallel component of the magnetic field could also be varied, either by an enhancement or diminishment. An enhancement would increase the strength of the Faraday rotation, which would decrease A_ϕ, while a diminishment would have the opposite effect. A region where the parallel magnetic field component changes sign will produce a very sharp feature in the Faraday spectrum, called a Faraday caustic [Bell et al., 2011; Beck et al., 2012]. Faraday caustics are strong candidates for detection at low frequencies, as they produce sharp, high-amplitude features that should not be strongly depolarized at low frequencies.

Finally, the free electron density can be varied, with the same effects as changes in the parallel magnetic field. Sharp localized changes in the free electron density can be associated with sharp density fluctuations, like shocks, and at interfaces between different gas phases of the ISM.

The different phases of the ISM have very different density and ionization conditions, leading to sharp changes in the electron density where a line of sight passes through regions containing different phases. Here we ignore the cold molecular phase and compact H II regions, which occupy a very small fraction of the ISM and are not expected to be large enough to contain sufficient synchrotron-emitting volume to be detected in our data (also, these phases have not been observed in the lines of sight probed by our data). We confine our consideration to the 3 phases which occupy the bulk of the volume of the ISM: the warm ionized medium (WIM), warm neutral medium (WNM), and hot ionized medium (HIM).

The highest thermal electron densities are found in the WIM, which has been found to have electron densities of approximately 0.18-0.46 cm^{-3} [Ferrière, 2001]. The WNM has total number densities of approximately 0.1-0.6 cm^{-3}, and ionization fractions of a few percent [typically inversely related to density; Wolfire et al., 1995]. The resulting thermal electron densities in the WNM are approximately 0.01 cm^{-3}, although this can be significantly higher in the presence of additional ionization sources [Jenkins, 2013]. The HIM has a lower thermal electron density of approximately 0.005 cm^{-3} [Spangler, 2009]. The number densities given are local, not volume averaged or multiplied by filling factors, as we want to consider the Faraday rotation occurring inside each phase.

Assuming a parallel magnetic field strength of 2 μG and an electron density of 0.01 cm^{-3}, the WNM produces 0.016 rad m^{-2} pc^{-1} of Faraday rotation. For LOFAR observations like those presented here where the maximum scale is 1.1 rad m^{-2}, this corresponds to a path length of 68 pc. From this, we predict that our observations should be fully sensitive to neutral regions of this depth or shorter. Repeating the calculation for the WIM and HIM, with assumed typical electron densities of 0.2 and 0.005 cm^{-3} respectively and the same magnetic field strength gives 0.32 and 0.008 rad m^{-2} pc^{-1} of Faraday rotation. This, in turn, gives 7 and 140 pc as the depth scales

where a Faraday slab would begin to be resolved out in LOFAR observations, for the WIM and HIM respectively. Regions thicker than these values will be significantly depolarized at LOFAR frequencies, while regions thinner then these values will not suffer from significant internal depth depolarization. It should be noted that these depths are based on the assumed parallel magnetic field strength and thermal electron density, and so represent typical order-of-magnitude scales for this behaviour; variations in these parameters will change the required depth.

2.4.2 Rejecting Faraday thick models

An obvious starting point for a physical model of the IC342 field is a Faraday slab model, since most of the field shows two clear emission peaks in the Faraday depth spectrum, which can be interpreted as the signature of a Faraday slab. In this model, the Faraday depth offset from zero (and the variations in this offset with position) would be caused by a foreground Faraday-rotating volume with very little emission, while the emission and the separation between the two features is supplied by a Faraday slab.

It is not possible to determine from the data which emission feature is the leading (nearer to the telescope) edge and which is the trailing. If we assume the brighter feature at lower Faraday depths (top panels of Fig. 2.7) is the leading edge, the foreground Faraday rotation must contribute between -7 and $+3$ rad m^{-2} in front of the slab, and the slab has a thickness of approximately $+8$ rad m^{-2}. If we instead assume the weaker feature (bottom panels of Fig. 2.7) is the leading edge, the foreground Faraday-rotating region must contribute $+1.5$ to $+11$ rad m^{-2} and the slab has a thickness of approximately -8 rad m^{-2} (the negative sign signifying that the Faraday depth decreases with increasing distance). For both cases, there would also be a second Faraday-rotating screen behind the slab, providing negative Faraday-rotation to the background extragalactic sources (Table 2.1).

For an idealized Faraday slab, both features would have the same intensity, whereas we observe a significant difference, approximately a factor of 2–3 in polarized intensity, between the first and second emission features. This can be explained as a departure from the ideal tophat spectrum, with either a peak in the brighter side of the slab (such as is seen in Fig. 2 of Beck et al. 2012) or a more gentle decrease in the other side (producing additional depolarization, resulting in a weaker peak in the observed spectrum). If we assume that one of these peaks represents the observed intensity of an idealized Faraday slab and divide by the expected ratio of observed to true amplitude (12%, as per the previous section), this gives a prediction of the true polarized intensity of the slab. To convert from RMSF^{-1} to (rad m^{-2})$^{-1}$, we use the same method used for the conversion from mJy PSF^{-1} to brightness temperature, adapted to one dimension, and use the fitted Gaussian for RM-CLEAN. The resulting conversion is 0.93 rad m^{-2} RMSF^{-1}. Using 30 K RMSF^{-1} and 10 K RMSF^{-1} for the typical polarized brightnesses of the first and second emission features respectively, this gives intrinsic polarized amplitudes of 250 or 83 K (rad m^{-2})$^{-1}$. The two features are separated by approximately 8 rad m^{-2}, which would mean an intrinsic polarized flux of 2000 to 660 K. If the emission is more complex or turbulent than a uniform Faraday slab, which is almost certainly the case, then the emission will be more strongly depolarized and the intrinsic polarized flux must be higher than these values.

This diffuse emission is not seen in total intensity as it is smooth on the angular scales probed

by LOFAR and is correspondingly filtered out. However, the total intensity flux is known from earlier single-dish measurements. The 150 MHz all-sky map from Landecker & Wielebinski [1970] shows that the brightness temperature varies across this field from 460 to 600 K. Accounting for the fact that the maximum possible fractional polarization for Galactic synchrotron emission is about 75% [Rybicki & Lightman, 1985], this puts the upper limit for polarized flux at 345 to 450 K. This upper limit requires that the magnetic field be perfectly ordered throughout the emitting volume. For a more realistic combination of turbulent and ordered magnetic fields, this limit drops further.

Since the polarized flux required for this model (660 K or more) significantly exceeds the maximum possible polarized flux consistent with the total intensity (450 K or less), we conclude that our observations cannot be explained by a single Faraday slab or similar feature. This is also supported by the significant differences in morphology between the two observed features. Therefore, a multiple component model is required to explain the observations.

2.4.3 A six-component physical model

Having rejected the Faraday slab model, we propose a more complicated but physically motivated model, which contains two neutral regions producing the observed Faraday-thin features, three (presumably fully) ionized regions that are Faraday-thick and therefore depolarized and not observed but contribute to the Faraday rotation of the observed features, and the hot ionized Local Bubble.

The Local Bubble is the volume of HIM surrounding the Sun. The estimated depth of the Local Bubble in this direction is 90 pc [Lallement et al., 2014], and it is known to have a low electron density of 0.005 cm^{-1} [Cordes & Lazio, 2002]. Again using a typical magnetic field strength of 2 μG, the predicted Faraday rotation is 0.7 rad m^{-2}. Therefore, we do not expect the Local Bubble to contribute significant Faraday rotation of background polarized emission, and the synchrotron emission produced inside the Local Bubble should create a Faraday-thin feature in the Faraday spectrum at a Faraday depth at 0 rad m^{-2}. The bright emission feature passes through 0 rad m^{-2}, but it also covers Faraday depths from -6 rad m^{-2} to $+1$ rad m^{-2}. This indicates the presence of a Faraday rotating screen in front of the emission, so the Local Bubble cannot be the source of this emission feature. Instead, the Local Bubble emission we expect at 0 rad m^{-2} must be fainter than, and thus blended into, the brighter emission feature.

The emission features must be Faraday-thin, to be consistent with the flux calculations in the previous section, and behind at least one Faraday-rotating screen, which must provide the Faraday rotation observed in both components. Below we will identify possible physical causes for the emission features. Shocks from supernova remnants cannot explain our observations because no supernovae remnants are catalogued in the direction of our observations. The available data do not allow us to exclude Faraday caustics or other magnetic phenomena as possible explanations.

Identifying and localizing WNM or HIM volumes of interstellar space is difficult, as there are very few reliable tracers of these phases that are also distance resolved. The H I 21-cm line traces neutral gas and has been mapped extensively in the Galaxy, but does not provide good distance resolution within the nearest few hundred parsecs. Hot gas can be traced by soft X-ray emission, but this gives no distance information; bubbles of HIM in the Galactic disk are typically identified

as voids in the warm medium and by the presence of neutral walls around such bubbles. Na I absorption of starlight has been used to trace neutral clouds, but comprehensive maps only exist out to a few hundred parsecs [e.g. Vergely et al., 2010]. Similar maps of the local ISM have been made using optical extinction and reddening [e.g. Lallement et al., 2014; Green et al., 2015], which correlate well with the maps of neutral clouds and show the presence of the Local Bubble as a low-density region.

We used the software package MWDUST[5] [Bovy et al., 2016] to probe the dust distribution predicted by the Green et al. [2015] reddening model in the IC342 field, as a proxy for neutral clouds in the ISM. This code gives the total reddening to a given position; to determine the position of the dust/neutral clouds, the numerical derivative was taken with respect to distance to give the local reddening per unit distance as a function of distance. The results, for selected lines of sight, are shown in Fig. 2.9. For all of the lines of sight, there is a clear concentration of dust between 200 and 500 pc (depending on the line of sight), indicating the presence of a cloud that fills the field of view. For lines of sight D and E, which cover the center and lower-left of the field where the fainter emission feature is observed, a second cloud is present between 500 and 800 pc. Based on these profiles, we divided the line of sight into two regions: from 0 to 500 pc, and from 500 to 1000 pc, such that each region contains one distinct region of high local reddening; the resulting maps are shown in Fig. 2.10. The nearer cloud fills the field of view, while the more distant cloud is concentrated along a broad region from the bottom left corner towards the top right. The presence of this nearer cloud is also supported by models of the local ISM [Vergely et al., 2010; Lallement et al., 2014], which generally do not extend far enough in distance to include the second cloud. The model by Lallement et al. [2014] shows no bubbles of HIM beyond the Local Bubble in the direction of our data, out to a distance of 500 pc. Therefore HIM regions cannot explain the polarization features we observe.

Due to the morphological correspondence, we interpret the two emission features in our observations as emission produced in these two neutral clouds, and use the estimated distances and sizes of these clouds to produce a model for the emission and Faraday rotation. Drawing from the dust models, we begin our model with two warm neutral clouds, the first at a distance of 200 pc, and the second at a distance between 500 and 800 pc, which produce the observed polarized emission. The distance between the Local Bubble and the first neutral cloud we model as a warm ionized region, which provides the observed Faraday rotation of the emission from the first cloud. Between the two clouds is another ionized region which provides the Faraday rotation difference between the two emission features, and beyond the second cloud is some unconstrained volume of ionized gas to the edge of the Galaxy which provides the difference in Faraday rotation between the diffuse emission and the background polarized sources. Fig. 2.11 gives a schematic view of this model, where the two emitting regions are matched to the two neutral clouds.

The observed emission features were assigned to the neutral clouds based on their morphology. The more distant dust feature runs through the field from the bottom left to the upper right, occupying a very similar part of the field as the fainter emission feature. The nearer dust cloud fills the field of view, as does the brighter emission feature. Based on these similarities, we assigned the brighter feature to the nearer cloud ('E1' in Fig. 2.11) and the fainter feature to the more

[5] https://github.com/jobovy/mwdust

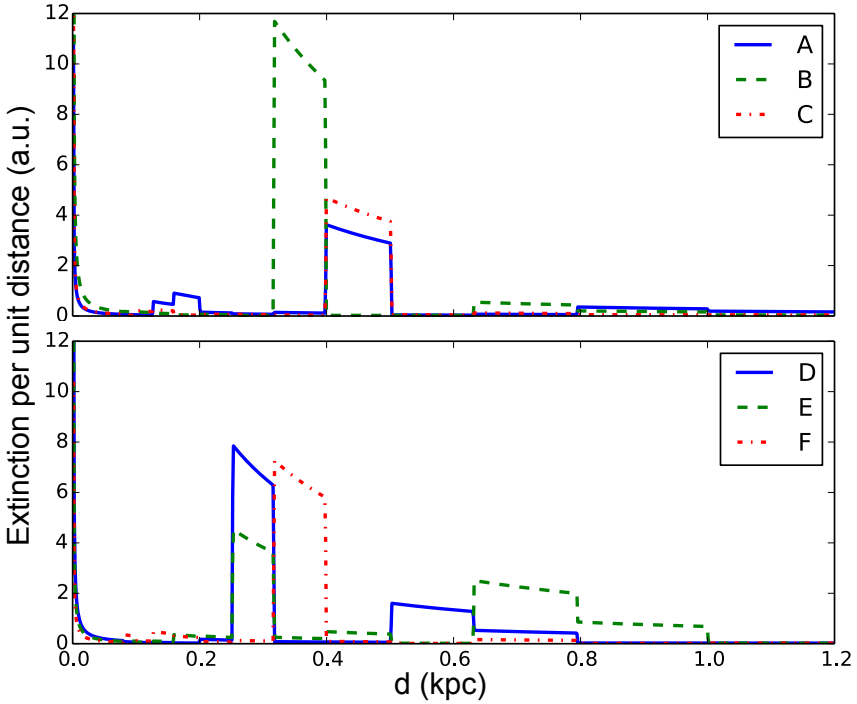

Figure 2.9: Profiles of the local reddening per unit distance for selected lines of sight in the IC342 field, calculated from the Green et al. [2015] reddening model with MWDUST. The labels correspond to the lines of sight shown in Fig. 2.6. All six profiles show the presence of a dust cloud between 200 and 500 pc, and D and E show the presence of a second cloud between 500 and 800 pc.

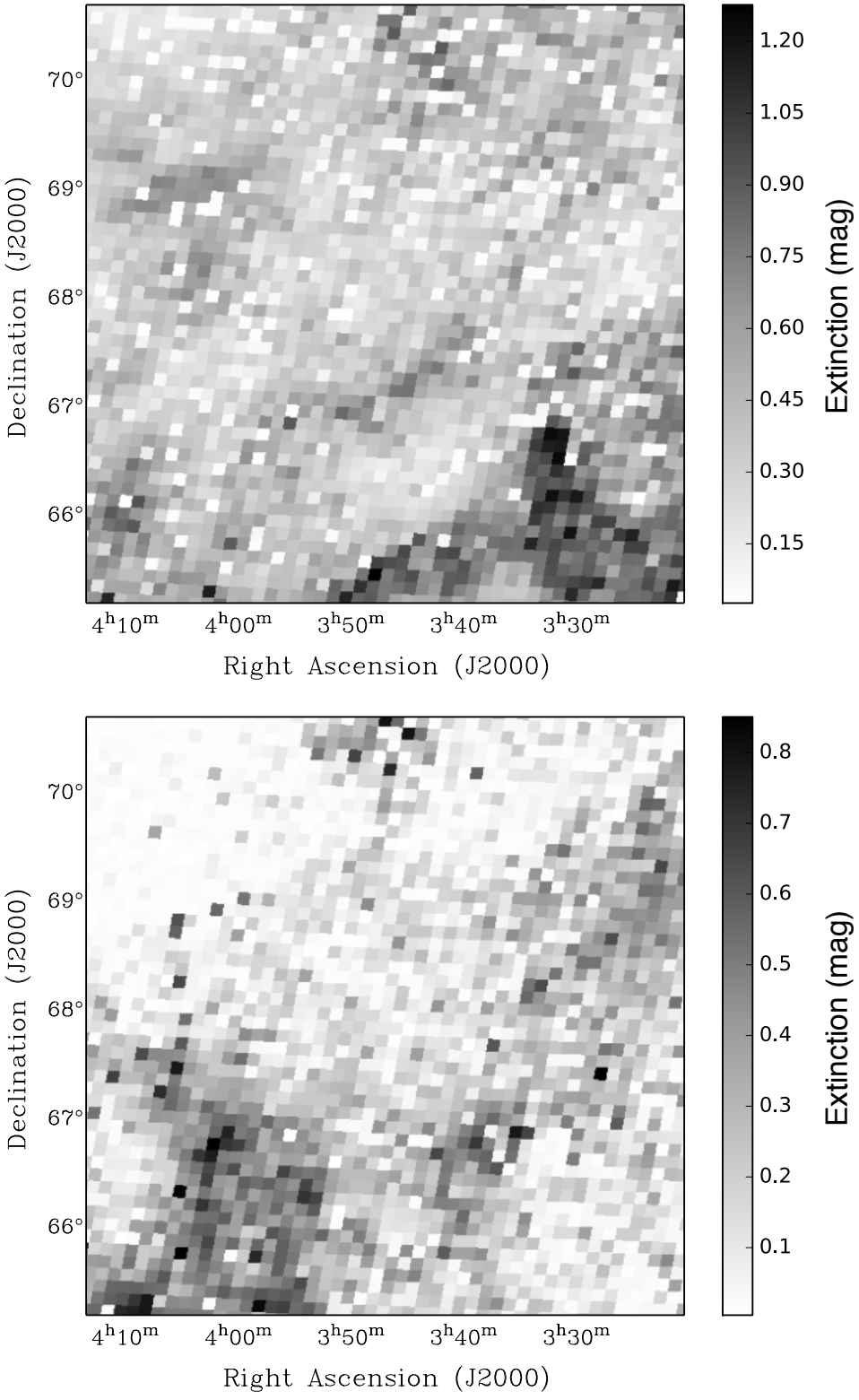

Figure 2.10: Maps of the reddening caused between 0 and 500 pc (top), and 500 and 1000 pc (bottom), calculated by integrating profiles from Fig. 2.9 over the selected distance range. The pixel size is set by the resolution of the Green et al. [2015] model. The top plot shows the presence of a field-filling dust cloud (assumed to be a neutral region) while the bottom shows the presence of a more distant cloud that occupies only part of the field.

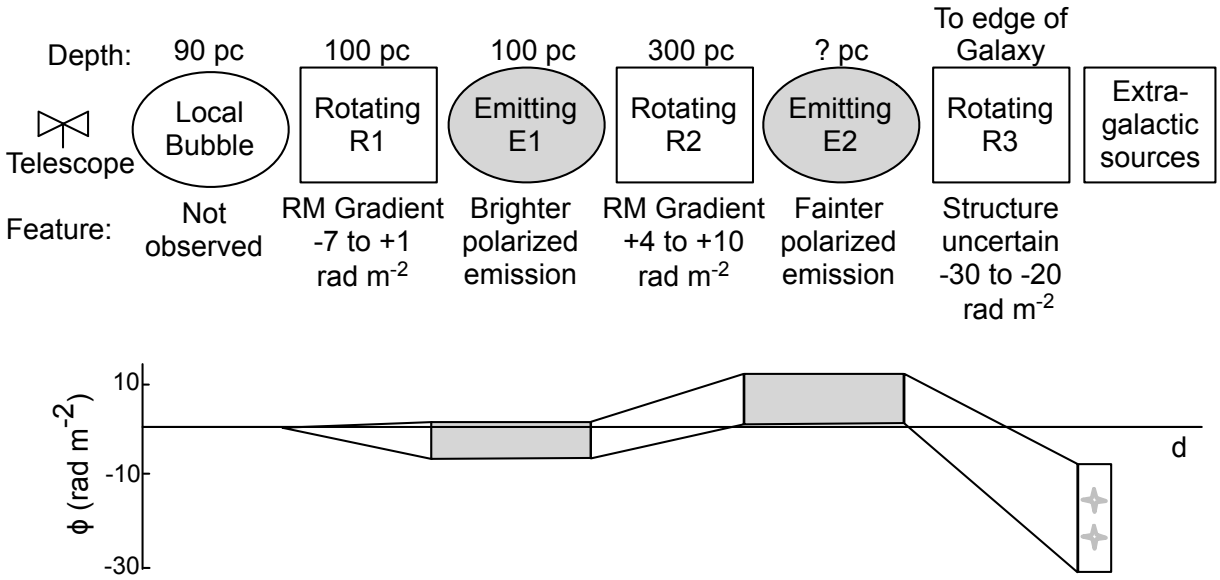

Figure 2.11: A schematic view of the physical model for the IC342 field. The three Faraday-rotating and two emitting regions are labelled, for clarity in the text, and the defining feature of each region is given. The Local Bubble is included as it is a known ISM feature that occupies a portion of the line of sight, but does not contribute significant Faraday rotation and no associated polarized emission is observed. The Faraday depth of each region is shown below, with the two horizontal lines bounding the range of Faraday depths for different positions in the field; for any given direction and distance only one value in that range is appropriate. Grey shading and stars represent diffuse and point-source polarized emission respectively.

distant cloud (E2). The depth of the nearer cloud was estimated from the Vergely et al. [2010] and Lallement et al. [2014] models to be roughly 100 pc, but the more distant cloud is outside of the region of these models. The Green et al. [2015] dust model does not have the distance resolution to estimate the depths of the clouds. We note that the 100 pc depth of the region is greater than the depolarization depth scale discussed at the end of Sect. 2.4.1, but this can be due to the parallel magnetic field or thermal electron density being slightly lower than the values assumed in that calculation.

At a reference frequency of 150 MHz (near the center of the band for these observations), a typical value for the (total intensity) synchrotron emissivity is about 140 K kpc^{-1} [Iacobelli et al., 2013; Nord et al., 2006]. The polarized fraction is difficult to estimate, as it depends strongly on position (e.g. the Galactic plane is strongly depolarized) and resolution (coarser observations have increased beam depolarization). The maximum possible polarization fraction of synchrotron emission is about 75% for Galactic synchrotron [Rybicki & Lightman, 1985]. An approximate value can be made using Equation 10 of Burn [1966], which states that the polarized fraction is modified from the maximum by the ratio of the energy of the large-scale field to the energy of the total magnetic field when the scale of the random field is smaller than the resolution. Using typical values of 2 μG for the ordered field and about 6 μG for the total field gives an estimate of about 8%, but this may be a lower limit as the ordered field estimate is for much larger scales than the expected spatial resolution of our observations (our resolution at 200 pc gives a scale of about 0.3 pc, so all scales above a few pc may be considered as part of the ordered field for our purposes). Using this 8% value, the expected polarized emissivity is 11 K kpc^{-1}.

Using the value and the estimated depth of the first emitting region, the predicted polarized synchrotron brightness is 1.1 K, well below the observed value of 30 K. This implies that the perpendicular magnetic field may be significantly stronger than average, or that the magnetic field is more ordered (on the physical scales being probed) than the rough estimates used above. Without a depth estimate for the second cloud, it is not possible to give a predicted polarized brightness.

The first Faraday-rotating region (labelled R1 in Fig. 2.11) is associated with Faraday rotation by the ionized gas between the Local Bubble and the first neutral cloud. As with the Faraday slab model, the first region must provide the spatial gradients in Faraday depth that are observed in both emission features, and must provide all the Faraday rotation present in the first emitting region, corresponding to Faraday depths between −7 and +1 rad m^{-2}. Assuming a path length of approximately 100 pc, and a thermal electron density of 0.1 cm^{-3}, the required average parallel magnetic field strength ranges from −0.86 to +0.12 μG, with the magnetic field directed away from the Earth (negative) in the lower left corner and towards the Earth (positive) throughout the rest of the field.

The second Faraday-rotating region (R2) provides the Faraday depth offset between the two diffuse emission features, which varies with location between +4 and +10 rad m^{-2}. Assuming a depth of about 300 pc for this inter-cloud region, the average product of the electron density and parallel magnetic field needed to produce this Faraday rotation is between 0.016 and 0.042 μG cm^{-3}. If we again assume a thermal electron density of 0.1 cm^{-3}, this gives an average parallel magnetic field strength of +0.16 to +0.42 μG.

The final Faraday-rotating region (R3) represents all Faraday rotation between the second cloud and the extragalactic polarized sources. Oppermann et al. [2014] used published extragalactic Faraday rotation measurements to produce an all-sky map of the Galactic foreground contribution. For our field, their map gives Faraday depths ranging from -54 rad m^{-2} to $+16$ rad m^{-2}, with a typical error of 10 to 30 rad m^{-2}. Since this error is much larger than the range of Faraday depths we observe, we concluded it was not meaningful to produce a difference map between the Oppermann et al. [2014] map and the second emission feature, which would represent the Faraday rotation in region R3.

2.5 Discussion

The largest discrepancy between the models and the observations is the intensity of the polarized synchrotron emission. This is not a surprising result given that this field is in the Fan region, which has been long known to have abnormally high polarization [Brouw & Spoelstra, 1976]. This is further supported by LOFAR observations of other regions of the sky, which have observed polarized brightnesses between 1 and 15 K [Jelić et al., 2014, 2015], and observations with the Murchison Widefield Array, which have observed an average polarized brightness of 4 K at 154 MHz [Lenc et al., 2016]. Given the unusually high polarization of the Fan region, an enhancement in the perpendicular magnetic field or the degree of order in the magnetic field would be quite reasonable.

Our model presented in Sect. 2.4.3 assumes that the Faraday thin emission comes from mostly neutral regions associated with the warm neutral phase of the ISM. It could be possible that one or both emission features correspond to a Faraday caustic, particularly the fainter feature as that emission has the most positive Faraday depths and could represent the transition from parallel fields oriented towards the Sun (producing positive Faraday rotation) to fields oriented away from the Sun (producing negative Faraday rotation). This alternative is effectively indistinguishable from the two neutral cloud model of the previous section, but would require a substantial path length with very small parallel magnetic fields in order to produce enough polarized intensity at the same Faraday depth. The more distant neutral cloud in the model is less certain to exist than the nearer, as it is beyond the range of the Lallement et al. [2014] model and the morphological correspondence between the Green et al. [2015] extinction map (bottom of Fig. 2.10) and the fainter emission feature (bottom left of Fig. 2.7) is weak. This feature could also be explained by a bubble of HIM without affecting the model significantly. Another possibility, as discussed in Sect. 2.4.1, is enhanced magnetic fields from a shock or compression. There are no known supernova remnants or other features that might indicate such a shock, so we did not consider this for our model.

It is important to note that in this model it is not that the synchrotron emission or intrinsic polarized fraction is enhanced in the neutral regions, compared to the ionized regions, but rather that these are the only portions of the line of sight that are not strongly depolarized at low frequencies. The magnetic field can have identical properties between the neutral and ionized regions, without affecting this model. The transition between a strongly Faraday-rotating ionized medium and a weakly Faraday-rotating (mostly-) neutral region, combined with the limited

physical depth of the neutral regions, produces a very narrow feature in the Faraday spectrum that does not depolarize much compared to the other polarized emission along the line of sight.

In this model we have considered only the effects of depth depolarization, and not beam depolarization. Depth depolarization causes a Faraday-thick emitting and rotating region to depolarize, but does not affect the polarized intensity of background emission (unless the background emission overlaps in Faraday depth, as might occur if the parallel component of the magnetic field reverses sign along the line of sight). Beam depolarization, which can be produced by unresolved gradients in Faraday depth, will cause some depolarization of background emission passing through a Faraday rotating foreground [Tribble, 1991; Sokoloff et al., 1998; Schnitzeler et al., 2015]. This is most likely present in our observations, causing the observed polarized intensities to be lower than the true values. Since the values of polarized intensity were not important for our analysis (beyond the observation that they are already quite high, even without accounting for beam depolarization), we did not include any beam depolarization in our modelling.

If we assume that the observed emission features are Faraday thin and not significantly depolarized, the integrated polarized intensity of each diffuse polarized feature (Fig. 2.7, left panels) should represent the intrinsic polarization of the emitting regions. The variations in the polarized intensity with position on the sky may reflect variations in the local synchrotron emissivity which are caused by variations in the perpendicular magnetic field. A detailed analysis of the properties of the integrated intensity may yield interesting measurements of the properties of the emitting region, but such analysis is beyond the scope of this paper.

Our model also assumes that the Faraday rotation of the first emission feature was caused by an ionized region outside the Local Bubble when estimating the magnetic field strength. It is also possible that the Local Bubble wall may provide a significant amount of this Faraday rotation, if it has enhanced magnetic field strength and free electron density [such as observed in the W4 superbubble by Gao et al., 2015]. It is also possible that part of the variation in Faraday depths across each emission feature is caused by changing path lengths through the ionized regions, if the distances to the clouds vary significantly between different positions in the field.

The morphological correspondence between the dust maps and the observed polarized emission was used to motivate the presence of the neutral clouds in the model, but the correlation between regions with high dust density and high polarized emission is actually quite poor. We can explain this imperfect correspondence because the polarized synchrotron intensity depends on the path length of neutral (or low-ionization) material, and not the column density. For regions of higher dust column density, it is not possible to distinguish between lines of sight with long path lengths of lower density neutral material or shorter lengths of higher density material. For our analysis it is not important what quantity of dust present, but instead where it is present in sufficient quantity to serve as an indicator of the neutral phase of the ISM.

Further evidence that the fainter emission is likely to be more distant is in the characteristic angular scale of the emission. From a visual inspection of Fig. 2.7, it appears that the brighter feature has more emission on larger angular scales (the long, mostly straight depolarization canals are a clear signature of this), while the fainter emission clearly has much more structure on smaller scales. If we assume that the characteristic angular scale is caused by the characteristic turbulent length scale in the emitting volume and that this scale is approximately the same for

both features, then the fainter emission must be more distant. If we assume that the structure comes from depolarization effects in Faraday-rotating regions in front of the emission, and that these depolarization effects are tied to the turbulent length scale in the Faraday-rotating regions, then the same argument holds and the fainter emission must be more distant. A quantitative analysis of the characteristic scales and angular power spectra is beyond the scope of this paper, but should be investigated in follow-up studies.

This type of modelling can benefit significantly from the inclusion of rotation measure and dispersion measure data (which measure the column density of free electrons) from pulsars with independent distance estimates. Of the 17 pulsars listed in the ATNF catalogue[6] within ten degrees of IC342, 16 have DMs, two have RMs, but only two have independent distance measurements. Both of these are beyond 2 kpc, well outside the distance range of our model, so they are not useful for constraining either the Faraday rotation or the electron density. We did not include these pulsars in our analysis, but future modelling on other fields should consider pulsar measurements.

2.6 Summary and conclusions

We have observed a 5° by 5° region centred on the nearby galaxy IC342 using LOFAR in the frequency range 115–178 MHz, and performed Faraday tomography to detect the foreground Galactic diffuse polarized synchrotron emission. We clearly detect two emission features, overlapping in position but separated in Faraday depth. Both features are distributed in Faraday depth with similar gradients, but with very different morphologies in integrated intensity.

We have performed simulations showing the extent of the depolarization of Faraday-thick structures at LOFAR frequencies. Faraday slabs, which are defined by a tophat function in the Faraday profile and represent regions of uniform emission and Faraday rotation, are strongly depolarized: they retain only 12% of their true amplitude at the edges, producing the appearance of two low-intensity Faraday-thin peaks. Smoother features in the Faraday profile would be more strongly depolarized.

From the strong depolarization shown in these simulations, and a comparison of the observed polarized intensity compared to the total intensity, we argue that these features cannot be the edges of a Faraday slab or other Faraday thick structure, and represent two Faraday thin emission regions. Such emission regions require a volume without significant Faraday rotation, so we further argue that these emission regions probably correspond to mostly neutral clouds within the nearby ISM large enough to produce significant synchrotron emission. We have inspected reconstructed maps of the ISM, and found there is evidence for two neutral clouds along the lines of sight we observed. Using the estimated sizes and distances to these neutral clouds, we proposed a model where these two neutral regions produce the Faraday-thin polarized emission, while (depolarized) ionized regions through the remainder of the line of sight provide the observed Faraday rotation structure. Using estimated sizes and distances to these clouds, we have modelled the synchrotron emission and Faraday rotation for lines of sight through this region. We find that even in the Faraday-thin case, where there is no depth depolarization present, we observed much

[6] http://www.atnf.csiro.au/people/pulsar/psrcat/

more polarized intensity than can be explained using typical values for relevant parameters. This is not surprising, as our field is in the Fan region, which is known for anomalously high polarization. We estimated that the strength of the parallel magnetic field required to produce the observed foreground Faraday rotation is -0.86 to $+0.12$ μG (where positive is orientated towards the Earth, negative away from the Earth).

To confirm that the observed emission features are tied to these neutral clouds, similar observations over a large area of the sky would be very useful. These would allow for the large-scale morphology of the emission to be observed and correlated against the boundaries of the neutral clouds inferred from extinction and Na I absorption. Such observations would be best done at low Galactic latitudes, where the locations of neutral clouds are best constrained by the ISM models.

If confirmed, this provides us with a very powerful method to map out the magnetic field (parallel to the line of sight) inside the local ISM. There are many known neutral clouds within 500 pc of the Sun, which could be used to produce models of the magnetic field in the local ISM in the same way that the observed RMs of pulsars and extragalactic sources are used to model the large-scale field of the entire Galaxy.

This method relies on the properties of depolarization at very low frequencies. Emission features that are extended in Faraday depth are very strongly depolarized at low frequencies, meaning that they can be effectively filtered out based on the choice of observing frequency, leaving only Faraday-thin components that can be isolated and studied individually. This makes low-frequency Faraday tomography a unique way to probe the magnetism of our Galaxy.

Acknowledgements
We thank the referee for their feedback, which has significantly improved the manuscript. This work is part of the research programme 639.042.915, which is (partly) financed by the Netherlands Organisation for Scientific Research (NWO). AMMS and DDM gratefully acknowledge support from ERCStG 307215 (LODESTONE).

LOFAR, the Low Frequency Array designed and constructed by ASTRON, has facilities in several countries, that are owned by various parties (each with their own funding sources), and that are collectively operated by the International LOFAR Telescope (ILT) foundation under a joint scientific policy.

2.A Simulating Faraday slabs

To determine the degree of depolarization that could be expected in LOFAR observations, we performed simulations of Faraday slabs of different widths but fixed amplitude (where we define the amplitude as the magnitude of the Faraday profile, which has units of spectral flux density (or brightness temperature) per unit Faraday depth), using the same frequency coverage as the IC342 observations, and measured the resulting simulated peaks in the Faraday spectrum. The resulting 'measured' amplitude of the peaks is shown in Fig. 2.12 as a function of the width of the slab. For widths greater than about 2 rad m^{-2} (twice the width of the RMSF), the amplitude varies between 11 and 13% of the true amplitude.

The weak dependence on the width is a consequence of the way we have defined the Faraday slab, with a fixed Faraday spectrum amplitude. This results in the intrinsic polarization (the hypothetical polarization at $\lambda^2 = 0$) being equal to the product of the amplitude, A_ϕ, and the width of the slab, $\Delta\phi$. The polarized intensity as a function of wavelength is then defined as $P(\lambda^2) = A\Delta\phi\frac{|\sin(\Delta\phi\,\lambda^2)|}{\Delta\phi\,\lambda^2}$. So for a fixed bandwidth, the only effect of changing the width is the number of oscillations of the sine term, which only weakly affects the observed amplitude. Therefore, the 11 to 13% figure given above applies to all Faraday slabs with widths greater than about 2 rad m^{-2} when observed by LOFAR.

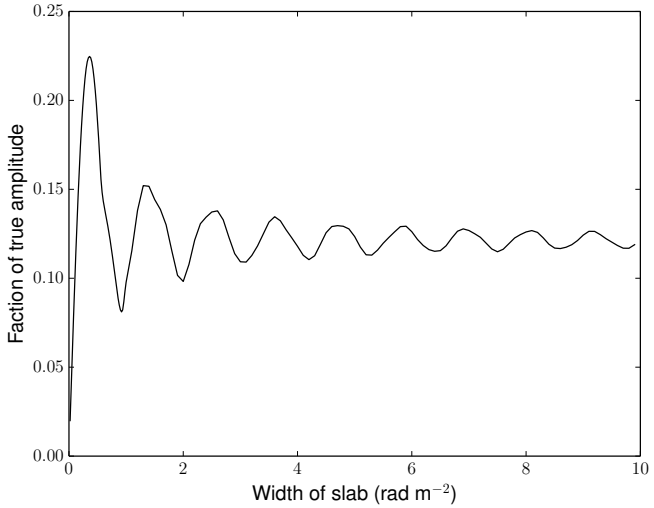

Figure 2.12: Measured amplitude of ideal Faraday slabs, for the same bandwidth as the IC342 observations, as a function of the width of the slab. For widths significantly wider than the RMSF (1 rad m^{-2}), the amplitude oscillates around 12% of the intrinsic amplitude, with variations of about 1%.

Chapter 3

Testing ionospheric Faraday rotation corrections for LOFAR

Abstract

The new generation of low-frequency radio telescopes offer us the ability to measure the Faraday rotation of polarized radio emission with unprecedented accuracy, by taking advantage of the strong wavelength dependence of Faraday rotation. Using the Low Frequency Array (LOFAR), it is possible to achieve measurement accuracy of 0.1 rad m^{-2} or less. However, to fully exploit this high accuracy, it is necessary to correct for the Faraday rotation caused by the Earth's ionosphere, which is typically of order 1–2 rad m^{-2}. These corrections are typically done by predicting the ionospheric Faraday rotation using models of the Earth's magnetic field and measurements of ionospheric free electron density. In this report I present work that I did on testing these corrections with LOFAR observations during two 'Busy Week' meetings organized by the LOFAR Magnetism Key Science Project. I found that these corrections can be successfully applied to LOFAR data and produce the expected changes in measured Faraday rotation and polarized intensities.

3.1 Background

Just as the atmosphere provides many challenges for optical astronomy, the ionosphere plays a similar role in low-frequency radio astronomy. The ionosphere is a region above the Earth's atmosphere, typically from 60 to 1000 km above ground level, that contains ionized gas, which interacts with radio waves through several different processes. For astrophysical observations it is desired to measure the properties of the astrophysical source being studied, so it is often necessary to remove any contaminating effects caused by the ionosphere in order to isolate the astrophysical signal.

The dominant effect of the ionosphere on low-frequency radio waves are changes to the index of refraction. It is a classical result in plasma physics (and correspondingly can be found in most plasma physics textbooks) that the free electrons in a plasma cause electromagnetic waves

to propagate slightly differently than in a vacuum, resulting in an index of refraction slightly different than unity. This difference depends on the density of the plasma, and is much stronger at low frequencies.

This effect manifests in several ways in low-frequency radio astronomy. Time variability in the ionosphere produces scintillation where variations in the ionosphere cause emission to be focused or defocused on a receiver, causing more or less emission to be observed at different times (directly analogous to 'twinkling' commonly seen in starlight). Spatial variations in the ionosphere cause initially smooth wavefronts to become distorted, which affects the phase relationships measured by the different elements of a radio interferometer and in turn changes the source position measured by the interferometer.

When measuring the polarization of low-frequency radio waves, an additional ionospheric effect is present. When a magnetic field is present, the index of refraction of plasma becomes polarization dependent: right-circularly polarized waves have a slightly different index of refraction than left-circularly polarized waves. When linearly polarized waves, which can be decomposed into a combination of left- and right-circularly polarized components, propagate through magnetized plasma, the phase difference between the circularly polarized components changes, resulting in a net change of the linear polarization angle. This is Faraday rotation and since the ionosphere is imbedded in Earth's magnetosphere, it contributes to the Faraday rotation of astrophysical radio emission passing through.

To measure astrophysical Faraday rotation with high precision, it is necessary to remove the ionospheric contribution. In the past, the ionospheric contribution to Faraday rotation has often been neglected, as this contribution is often on the order of 1–2 rad m^{-2}, and typical uncertainties in the Faraday rotation measures were larger than this. However, new low-frequency radio telescopes such as the Low Frequency Array (LOFAR) now allow for measurement accuracies of 0.1 rad m^{-2} or less, so the ionospheric contribution is no longer smaller than the uncertainties and much be corrected for in order to achieve the best accuracy possible.

In this report, I present tests of a software package for estimating the ionospheric Faraday rotation present in radio observations. This was commissioning work I performed as part of the LOFAR Magnetism Key Science Project (MKSP), during two 'Busy Week' commissioning meetings in Manchester, UK during 22–24 April 2015 and 26–28 August 2015. This work looked at the 'RMextract' software written by Maaijke Mevius[1], which reads in radio astronomy data and produces a prediction for the ionospheric Faraday rotation.

3.2 Estimating Ionospheric Faraday rotation

Ionospheric Faraday rotation cannot be directly observationally separated from the astrophysical Faraday rotation. Instead, it is necessary to estimate the ionospheric contribution and subtract it from the observations by rotating the observed polarization by an amount equal and opposite to the predicted ionospheric Faraday rotation, which should produce the same polarization as was present in the radio emission before it passed through the ionosphere.

[1] https://github.com/maaijke/RMextract/

To estimate the ionospheric Faraday rotation contribution, the necessary components are a magnetic field model for the ionosphere region, measurements of the ionospheric free electron content at the time and location of the observations, and a model for the distribution of the plasma/free electrons in the ionosphere.

A magnetic field model is required to know the magnetic field strength and orientation as a function of position on Earth, as this is essential in determining the strength and sign of the ionospheric Faraday rotation. RMextract uses the Enhanced Magnetic Model (EMM2015)[2] published by the National Center for Environmental Information in the United States of America. EMM2015 models the magnetic field at and near the surface of the Earth, using data that includes magnetometer measurements both from ground and from satellites orbiting in the upper parts of the ionosphere. The typical uncertainty in the magnetic field strength is of order 100 nT, or approximately 0.25%.

Measurements of the ionospheric free electron content are necessary to determine the density of free electrons present at the time of the observation, as this can vary quite strongly over time. The measured quantity is called the total electron content (TEC), and is the column density of free electrons in the ionosphere. TEC values are typically measured through frequency-dependent dispersive delays, which are caused by the frequency dependent index of refraction in the ionospheric plasma. Ground stations with dual-frequency GPS/GLONASS receivers can measure the time delay between signals at two frequencies, and use this to calculate the column density of free electrons (in radio astronomy terms, this is the dispersion measure from the ground to these satellites). These measurements are made for each satellite visible from the ground station, and for each ground station in the network, and are then used to construct maps of the ionospheric TEC. RMextract is currently capable of downloading these TEC maps from two different sources: the Centre for Orbital Determination in Europe (CODE) and the Royal Observatory of Belgium (ROB). Comparing these two TEC sources was a major task of this work, so the details of each are discussed later in this report. Uncertainties in measured TEC values are not well quantified, but are probably of order 10% [Rovira-Garcia et al., 2016], so TEC uncertainties dominate the uncertainties in the predicted Faraday rotation.

A model of the distribution of free electrons in the ionosphere is necessary for two reasons. First, it is necessary to determine how the TEC values change with the *slant angle* through the ionosphere (in astronomy terms, the zenith angle), as lines of sight closer to horizon will have longer path lengths through the ionosphere. Second, it's necessary to evaluate the Faraday rotation integral, particularly if the magnetic field changes significantly along the path length.

The standard model that is used for the both the CODE and ROB TEC maps as well as inside RMextract is a single thin shell model, where the ionosphere is treated as a spherical shell of infinitesimal thickness at some height above the Earth's surface. With this assumption, each TEC measurement and radio observation (and more specifically, each receiver used in an observation) has an ionospheric pierce-point (IPP) where the line of sight intersects with the modelled ionosphere. For TEC measurements, the IPP is used as the location of the measurement, and the locations between measurements are calculated by interpolation. To calculate the Faraday rotation contribution for an observation, the TEC value for the IPP is extracted from the TEC

[2] https://www.ngdc.noaa.gov/geomag/EMM/emm2015.shtml

maps and the magnetic field at the IPP location is calculated from the magnetic field model. It is not necessary to assume any value for the thickness of the ionosphere, as the TEC values are reported as column densities and thus already incorporate the integral over distance.[3]

3.3 RMextract

RMextract is a python package that provides functions to download TEC maps from CODE or ROB, extract TEC data from those maps, calculate magnetic field vectors from the EMM2015 magnetic field model, and calculate ionospheric Faraday rotation for radio observations. Must usefully, it has the ability to read in a radio astronomy observation in the Common Astronomy Software Applications (CASA) Measurement Set (MS) format, which is used for LOFAR observations, extract the critical parameters such as the time, location, and direction of the observation, and output the ionospheric Faraday rotation as a function of time and station in the array in the parmdb (Parameter Database) format which is used by the primary LOFAR calibration software packages, Blackboard Selfcal (BBS) and Default Pre-processing Pipeline (DPPP). This allows these software to subtract the ionospheric Faraday rotation in that observation.

At the beginning of the first Busy Week (22–24 April 2015), RMextract could only use TEC maps from CODE, but the ability to download and use ROB TEC maps was developed over the course of that week. RMextract uses these TEC maps with the EMM2015 model, and assumes a single thin layer ionosphere at a height of 450 km to calculate the ionospheric Faraday rotation.

One of the major purposes of the Busy Weeks tests was to compare the effectiveness of the CODE and ROB TEC maps. The CODE TEC maps are generated with a time resolution of 2 hours, and are produced by fitting their observations with spherical harmonic functions up to order 15, giving an effective resolution of 2.5° by 5° in geographic latitude and longitude [Jee et al., 2010] which corresponds to scales of about 250 km. By comparison, the ROB TEC maps have a time resolution of 15 minutes and a resolution of 0.5 by 0.5° [Bergeot, Nicolas et al., 2014].

3.4 Testing RMextract

The first polarization Busy Week, 22–24 April 2015, had the goals of testing RMextract in several ways: first, that it worked and could be applied successfully to LOFAR data, producing the expected astrophysical Faraday rotation measurements; second, whether the different TEC maps produced different results; and third, whether RMextract would predict different ionospheric Faraday rotation for widely separated LOFAR stations. I was directly involved in the first two of these tests, so they will be described below.

The second polarization Busy Week, 26–28 August 2015, had the goal of testing RMextract on longer observations to see if the initial results from the first Busy Week still held and how well the time variability in the predicted ionospheric Faraday rotation matched the variations in the real data.

[3]Since the ionosphere model assumes a layer of infinitesimal thickness, the magnetic field is treated as constant along the line of sight through the ionosphere so that it comes out of the Faraday rotation integral, which converts that integral into the free electron column density.

3.4.1 Data

The first Busy Week used a single 7-minute observation taken from the Multifrequency Snapshot Sky Survey [MSSS, Heald et al., 2015], pointing H035+44. This observation had 8 bands of 2 MHz bandwidth divided into 5 channels, and was calibrated using the MSSS pipeline. This observation was chosen for the presence of a known pulsar, J0218+4232, with a previously known rotation measure of -61.4 rad m^{-2} (Charlotte Sobey, private communication).

The second Busy week used an 8 hour observation centred on the pulsar B0329+54/J0332+5434, with the same frequency structure as the previous observation. This pulsar also had previously measured rotation measure measurements of -61.7 rad m^{-2} (Charlotte Sobey, private communication), -63.7 ± 0.4 rad m^{-2} [Manchester, 1972], and -65.8 rad m^{-2} (Emilio Enriquez, private communication). The observation was calibrated by David Mulcahy prior to the Busy Week.

For both pulsars, it's not clear how these previous measurements accounted for the ionosphere, so they were treated as guidelines for which Faraday depths to expect, rather than as target values for the ionospheric correction to achieve.

For both data sets, the steps taken during the Busy Weeks were mostly the same. First, RMextract was used, with the specific settings being tested, to calculate the predicted ionospheric Faraday rotation and produce a parmdb output. Next, BBS was run using this parmdb to apply the correction to the observation. AWImager [Tasse et al., 2013b] was used to image all of the channels in the observation in Stokes Q and U. Finally, pyRMsynth[4] was used to perform RM synthesis. Examples of the resulting Faraday spectra are shown in Figure 3.1.

3.4.2 Results

The first test, using the 7-minute MSSS observation, was to confirm that RMextract produced reasonable output and that the ionospheric correction could be successfully applied to a LOFAR MS, using both ROB and CODE TEC maps. It was also an initial check that the two TEC sources gave similar results. Using the CODE TEC maps, it predicted the ionospheric Faraday rotation was between 2.73 and 2.77 rad m^{-2} (where the range is the values at the start and end points of the observation; RMextract interpolates between TEC measurements, and the 7-minute observation is shorter than the time resolution of both TEC sources), while using ROB TEC maps predicted between 2.74–2.75 rad m^{-2}.

Three RM cubes were made: with no correction, with the CODE correction, and with the ROB correction. Each cube had a Faraday depth step size of 0.5 rad m^{-2}, so the Faraday depth of the pulsar could not be determined more precisely than this. For each cube, the Faraday depth and polarized intensity of the peak was read directly from the cube (no fitting was done). Without the correction, the measured Faraday depth and polarized intensity were -59.0 rad m^{-2} and 175 mJy; after correction with CODE they were -61.5 rad m^{-2} and 201 mJy; after correction with ROB they were -61.5 rad m^{-2} and 207 mJy. The Faraday depth change caused by both corrections were the same (within the limited measurement accuracy), and consistent with the predicted shift. The post-correction Faraday depth was consistent with the previous measurements. The polarized intensities measured with both the CODE and ROB corrections were consistent with

[4] https://github.com/mrbell/pyrmsynth

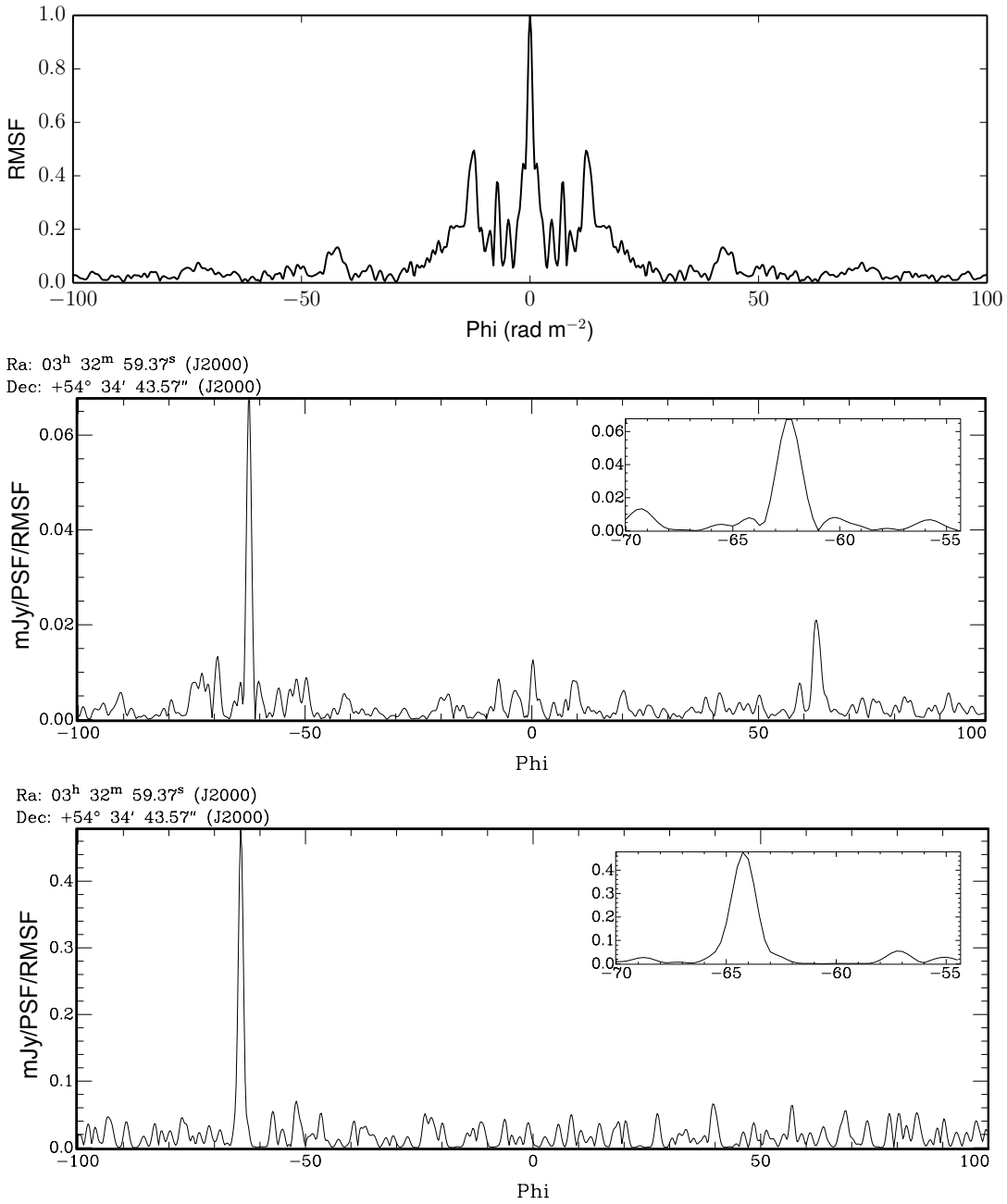

Figure 3.1: *Top:* the rotation measure spread function (RMSF), a function of Faraday depth ('Phi'), resulting from the frequency coverage of the observations (both observations used the same frequency coverage, and thus have the same RMSF). *Middle:* The Faraday spectrum from the 8-hour observation of B0329+54. The primary peak is visible at -62.5 rad m^{-2} (the inset is zoomed in on this peak), as well as a small leakage peak at 0 rad m^{-2} and an artifact peak at $+62.5$ rad m^{-2} (an artifact caused by the RM synthesis software). *Bottom:* The Faraday spectrum from the same observation after correction using the prediction generated using CODE TEC maps. The peak is clearly shifted in Faraday depth, and has a much greater polarized intensity. The leakage and artifact peaks are smeared out as a result of the correction and are depolarized to the extent they can no longer be seen. The spectrum resulting from the ROB correction is not shown but looks very similar.

each other and slightly higher than the uncorrected measurement. This observation was short enough that depolarization based on time-variability in the ionosphere was not expected to be significant, so I interpret this being due to the Faraday depth of the corrected peaks being closer to the sampled Faraday depth than in the uncorrected data (i.e., in the uncorrected data the true peak falls between two sampling points, so the true peak flux is not measured). From this test, I concluded that the correction was being successfully applied to the observation, and that ROB and CODE both gave consistent answers.

The follow-up tests with the 8-hour observation were intended to test the performance of the ionospheric correction on longer time scales. It was expected that the ROB TEC maps would more accurately predict the ionospheric variability, as it had better spatial and temporal resolution. The first test with these data mirrored the previous test: I produced 3 Faraday depth cubes (with a finer sampling of 0.25 rad m^{-2}) using the full data with different ionospheric corrections: no correction, with ROB, and with CODE. The ionospheric Faraday rotation predicted by RMextract with the CODE and ROB TEC maps are shown in Figure 3.2. From this plot, the prediction using ROB TEC maps clearly shows shorter duration variability as expected, but it also shows a systematic offset of about 0.1-0.2 rad m^{-2} between the CODE and ROB TEC maps. For this observation, depolarization was expected to be much more significant because of the significant change (almost 1 rad m^{-2}) in the ionospheric Faraday rotation over the duration of the observation. This depolarization is caused by different Faraday rotation (producing correspondingly different polarization angles) at different times being averaged together; correctly predicting and correcting for the changes in the ionospheric Faraday rotation should remove this depolarization and result in higher polarized intensity.

As with the previous test, the Faraday depth and polarized intensity of pulsar were measured from each RM cube. The uncorrected cube had a clear peak between -62.5 and -62.25 rad m^{-2}, and a polarized intensity of 63 mJy. After correction with CODE TEC maps, these values were -64.25 rad m^{-2} and 480 mJy; after correction with ROB TEC maps these values were -64.0 rad m^{-2} and 420 mJy. The shift in the peak Faraday depth between the corrected and uncorrected peaks, including the slightly larger correction with the CODE TEC maps, fits the predictions, confirming that the correction is being properly applied to the data. The difference between the polarized intensity values was very striking: the uncorrected peak had a polarized intensity 7–8 times lower than the corrected peaks, confirming that the uncorrected data is suffering from significant depolarization as a result of ionospheric variability. The larger polarized flux for the CODE-corrected peak suggested that the CODE-based correction was more accurately predicting the variability, despite the lower time resolution, which was an unexpected result.

The final test was to further investigate the time variability in the data and compare it with the predictions. For this test, I produced multiple RM cubes from the uncorrected data, each using 1 minute of data, spaced 15 minutes apart. From each cube, the RM spectrum at the pulsar location was extracted and a Gaussian was fit to the peak, giving a fitted amplitude (polarized intensity) and position (Faraday depth), which allowed the Faraday depth to be tracked more accurately than the Faraday depth resolution of the cubes (0.25 rad m^{-2}). This produced a sequence of 32 Faraday depth measurements. Figure 3.3 shows the resulting Faraday depth variations with the two ionospheric predictions overlaid. This figure shows that both predictions correctly predict the

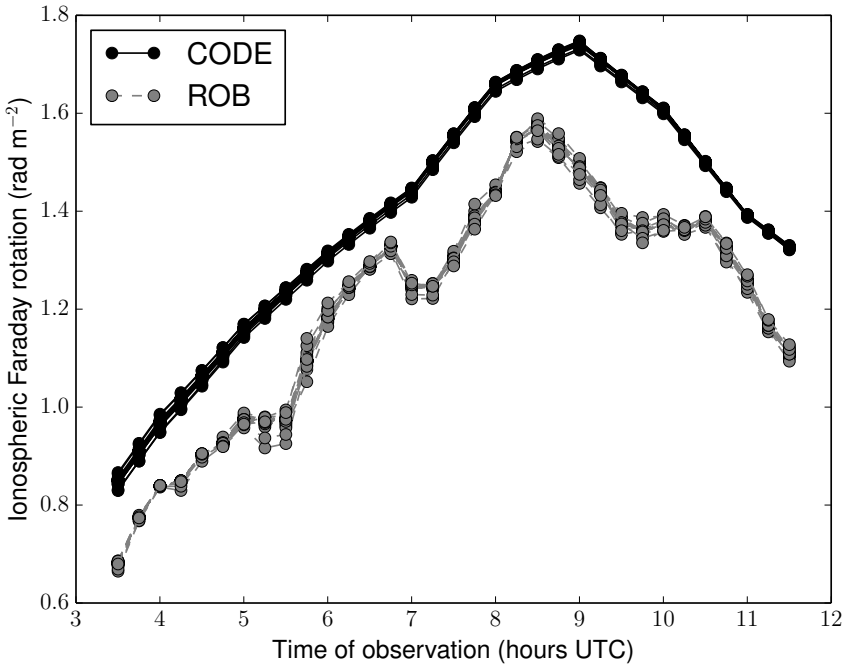

Figure 3.2: The ionospheric Faraday rotation predicted by RMextract, using the CODE (black) or ROB (grey) TEC maps, for the 8 hour observation of pulsar B0329+54. Each LOFAR station is plotted separately; the spread in points at each time is due to slightly different predictions at the different locations of each station. The higher time resolution of the ROB TEC maps is reflected in the shorter duration variability in the ROB prediction. There is also a systematic offset between the CODE and ROB predictions.

variations on longer (several hour) timescales, but the shorter duration variations predicted using the ROB TEC maps are not present in the observations and may even be anti-correlated with the actual variability. This result explains why the full-duration polarized intensity was lower with the ROB prediction: the ROB prediction did not follow the real variations as closely, resulting in greater depolarization.

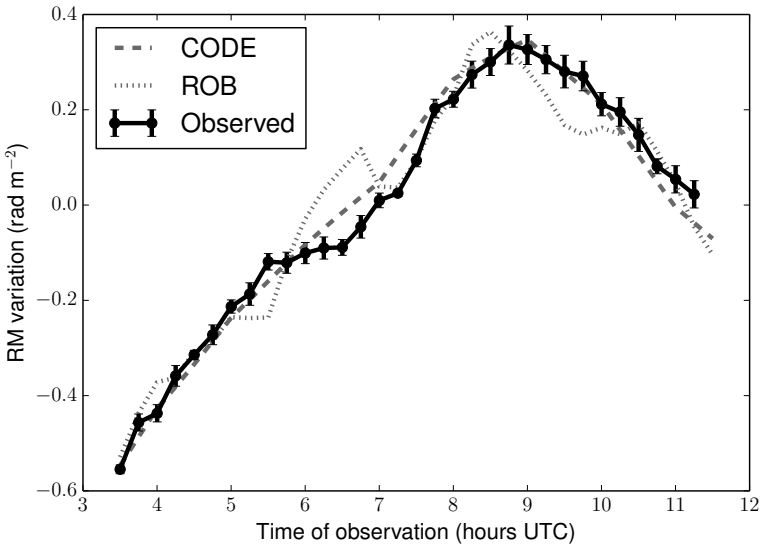

Figure 3.3: The observed variations in the Faraday depth of the pulsar (black points), along with the ionospheric Faraday rotation predictions made using the CODE (dark grey dashed line) and ROB (light grey dotted line) TEC maps, each with the mean subtracted so that they overlap. While the trend on multi-hour timescales is well matched by both predictions, the short-duration variations predicted using the ROB TEC maps are not matched in the observations. The CODE predictions more consistently follow the actual trends in the observations.

3.5 Conclusions and Remaining Questions

These tests have produced a few clear results:

- RMextract can successfully generate ionospheric Faraday rotation predictions, using TEC maps from both CODE and ROB, and these predictions can be applied to LOFAR observations using BBS.

- applying the ionospheric Faraday rotation correction makes a very significant difference to the resulting polarized intensity in long observations, showing that the correction is successful in removing a significant fraction of the variability, at least on longer time scales.

- while both TEC sources can predict the longer duration variations, the short term variations predicted by the ROB TEC maps don't appear to correspond to the variations observed in the data.

There are still some aspects that remain unexplored. Most notable is the systematic offset between the CODE and ROB predictions for the second data set: what is the origin of this offset? Is it present for other observations? Which is correctly predicting the magnitude of the ionospheric Faraday rotation? The first two questions may be answered with further investigation into the differences between how the TEC maps are generated. One possibility is that the difference may emerge from different assumptions about the height of the ionosphere (CODE assumes 450 km, while ROB assumes 400 km when creating the TEC models; RMextract assumes 450 km when calculating the predictions). This difference would change the position of the ionospheric pierce-point for an observation, and there may be sufficient differences in the ionosphere between the different predicted positions to account for this offset. If this is the case, we can expect this offset to be more likely to occur in observations further from the zenith.

The third question, regarding which prediction is correct, is tied to another question that these tests could not address: even if the time variability is successfully predicted, is the magnitude of the prediction correct? It is conceivable, but perhaps unlikely, that RMextract could successfully predict the time variability of the ionospheric Faraday rotation but also have a time-independent offset from the actual value. This could not be tested using the data available, because this would require a source with a very accurate and reliable absolute Faraday rotation measurement, with an uncertainty smaller than 0.1 rad m^{-2}. At this time, there are no such sources known. I propose two methods by which such an accurate absolute measurement could be made, but both are very far outside the scope of this project. The first possibilty method would be a space-based measurement of the Faraday depth of a source, as such a measurement could be made above the ionosphere and, assuming the (astrophysical) Faraday rotation of this source is not time-variable, could be used as a calibration target for further ground-based tests. The second method would be to identify a man-made satellite producing polarized emission at multiple frequencies, as this would allow the Faraday rotation through the ionosphere to the satellite to be measured (as the astrophysical Faraday rotation of a local satellite would be zero) and compared to predictions made by RMextract or other similar software.

An alternative to RMextract or other ionospheric prediction tools has been proposed, called 'rotation measure self-calibration' or RM Self-cal. The principle of this method is similar to the test I performed where I split the long observation into smaller time-ranges. For each small time range in an observation, some characteristic Faraday depth could be measured (it is not yet clear whether this would belong to a single source in the field such as a pulsar, or some average of all polarized emission in the field), and a correction could be calculated for each time-range that would shift the entire observation to the same Faraday depth. This method would have the advantage of capturing and removing all of the time-variabilty (on time scales longer than the time range used to measure the variation) in an observation, but would have the disadvantage of not having any information on the time-independent component of the ionospheric Faraday rotation. Ideally, a combined method that could combine the variability removal of the RM self-cal method with the absolute Faraday depth prediction provided from modelling software like RMextract could exploit the advantages of both techniques.

Acknowledgements
This work is part of the research programme 639.042.915, which is (partly) financed by the Netherlands Organisation for Scientific Research (NWO).

LOFAR, the Low Frequency Array designed and constructed by ASTRON, has facilities in several countries, that are owned by various parties (each with their own funding sources), and that are collectively operated by the International LOFAR Telescope (ILT) foundation under a joint scientific policy.

This research made extensive use of NumPy [van der Walt et al., 2011]; IPython [Pérez & Granger, 2007]; matplotlib [Hunter, 2007]; and the Common Astronomy Software Applications [CASA, McMullin et al., 2007].

Chapter 4

Polarized point sources in the LOFAR Two-meter Sky Survey

C.L.Van Eck, M. Haverkorn, M.I.R. Alves, R. Beck, P.N. Best, E. Carretti, K.T. Chyży, J.S. Farnes, K. Ferrière, G. Heald, C. Horellou, M. Iacobelli, V. Jelić, D.D. Mulcahy, I.M. Polderman, W. Reich, H.J.A. Röttgering, D.H.F.M. Schnitzeler, T.W. Shimwell, C. Sobey, V. Vacca, J. Vink, and G.J. White

A&A, in preparation

Abstract

Polarized radio sources and their Faraday rotation can tell us both about the magnetic fields in the interstellar medium of our own Galaxy as well as the magnetized environment in and around the sources themselves. The new generation of low-frequency radio telescopes, including the Low Frequency Array (LOFAR: a Square Kilometre Array Low pathfinder), offer much higher precision Faraday rotation measurements and the ability to probe complex structure in Faraday rotation through rotation measure synthesis.

The LOFAR Two-Meter Sky Survey (LOTSS) is an ongoing project to map out the sky north of declination 0° at very low frequencies (120–170 MHz) with high sensitivity and angular resolution. In this paper, we report on the preliminary development of a data reduction pipeline to carry out polarization processing and Faraday tomography for LOTSS data and present the results of this pipeline from the LOTSS HETDEX test region. We have produced a catalog of 102 polarized radio sources at 150 MHz, which is the first large polarized source catalog at such low frequencies. We suggest a number of possible analyses that this catalog would be uniquely suited for.

4.1 Introduction

Magnetic fields play a significant role in the dynamics and evolution of the interstellar medium (ISM) in galaxies, through many phenomena including confinement and acceleration of cosmic rays, angular momentum transport in star formation, and magnetohydrodynamic turbulence.

Observing the linear polarization of radio sources provides insight into the magnetic fields both at the source (from synchrotron polarization and Faraday rotation) and along the line of sight between the source and the observer (from Faraday rotation).

For many years, catalogs of large numbers of polarized radio sources (with corresponding Faraday rotation measurements) have been useful for many purposes including modelling the large-scale structure of the magnetic field in the Milky Way [e.g. Brown et al., 2007; Van Eck et al., 2011], studying the properties of smaller-scale structure in the Milky Way magnetic field [e.g. Haverkorn et al., 2008; Stil et al., 2014], studying magnetic fields in nearby galaxies [e.g. Gießübel et al., 2013], and studying the evolution over time of galactic magnetic fields [e.g. Farnes et al., 2014].

The amount of Faraday rotation (i.e. the extent to which the polarization position angle has rotated between the emission source and the receiver) is the product of the observing wavelength squared (λ^2) and the Faraday depth (ϕ, sometimes also called the Faraday rotation measure or RM) which is defined as

$$\phi(d) = 0.812 \text{ rad m}^{-2} \int_d^0 \left(\frac{n_\text{e}}{\text{cm}^{-3}}\right) \left(\frac{\vec{B}}{\mu\text{G}}\right) \cdot \left(\frac{\vec{dl}}{\text{pc}}\right), \tag{4.1}$$

where n_e is the number density of free electrons, $\vec{B}$ is the magnetic field, $\vec{dl}$ is a differential element of the radiation path, and the integral is taken over the line of sight from a distance d to the receiver. Polarized emission detected at different Faraday depths can be used to infer properties of the magnetic field along the line of sight.

The wavelength-squared dependence of Faraday rotation causes low frequency (long wavelength) observations to be much more sensitive to small variations in Faraday rotation. The new generation of very low frequency radio telescopes, including the Low Frequency Array (LOFAR) and the Murchison Widefield Array (MWA) have the potential to probe structure in Faraday depth at the level of 1 rad m^{-2} or less. However, low frequencies also generally increase the strength of depolarization processes, particularly for sources where the polarized emission is distributed over a range in Faraday depth, which can limit which magnetic field and ISM configurations can be observed [Van Eck et al., 2017].

In this paper, we present a new catalog of polarized radio sources observed at very low frequencies with LOFAR, covering a 570 square degree area of the sky. This is the first statistically useful sample of such sources at such a low frequency. In Section 4.2 we present the data reduction pipeline we used to generate the catalog, in Section 4.3 we present our catalog and compare it with the higher frequency catalog of Taylor et al. [2009], in Section 4.4 we analyze some interesting properties of our catalog, in Section 4.5 we discuss the implications of our results on larger area LOFAR polarization surveys and steps for improving our source-identification pipeline, and finally in Section 4.6 we summarize our work and suggest areas of analysis that our catalog would enable.

4.2 Data processing and source extraction

We used the calibrated data from the LOFAR Two-meter Sky Survey [LOTSS; Shimwell et al., 2017]; full details on observational parameters and data calibration can be found in their paper. The polarization calibration and imaging followed the methods used in Van Eck et al. [2017], and are summarized below; a flowchart showing the overall procedure of data processing and source identification is shown in Figure 4.1. This paper describes the results from the 63 fields covering the HETDEX region [Hill et al., 2008]. Each observation consisted of 8 hours (giving a nominal Stokes I sensitivity of 100 μJy) with the full LOFAR array (allowing angular resolutions up to $5''$ to be achieved), covering the frequency range from 120.262 to 167.827 MHz with 488 channels (resulting in a channel width of 97.656 kHz).

4.2.1 Imaging and RM synthesis

We began with the visibility data after direction-independent calibration.[1] Before polarization imaging was performed, it was necessary to correct for the Faraday rotation caused by the Earth's ionosphere. For this we used the RMExtract software[2] written by Maaijke Mevius, which calculates the ionospheric Faraday rotation for the specific time and observation direction of a LOFAR observation. This correction introduces a systematic uncertainty in the measured Faraday depths of approximately 0.1–0.3 rad m^{-2} [Sotomayor-Beltran et al., 2013].

Before imaging, we removed the baselines between the two HBA substations [e.g., CS002HBA0 and CS002HBA1; see van Haarlem et al., 2013b, for a description of the substation layout and naming] within each station, as these are known to often have significant instrumental contamination. All the remaining core-core baselines were used, as well as the baselines between the core stations and remote stations RS205, RS305, and RS503, which are closest to the LOFAR core. A baseline length cutoff of 800λ was also imposed. This was done to deliberately reduce the resolution so as to minimize the presence of image artifacts and to keep the resolution consistent across the full bandwidth. The AWimager software [Tasse et al., 2013b] was used to produce Stokes Q and U images for each channel. No CLEANing was performed, as the signal-to-noise ratio in individual channels was expected to be too low for this to be effective.

The primary purpose of the polarization imaging was the investigation of the Galactic diffuse polarized emission, and so several parameters in the imaging process were optimized for this science goal. The resulting data products were not ideal for point source analysis, but a full reprocessing using point source-optimized parameters was not possible within the scope of this work. A discussion of how the processing could be improved for polarized point source extraction appears in Section 4.5.1.

A fraction of the resulting images were found to have issues, usually in the form of image artifacts formed by single baselines or stations with anomalously high amplitudes. To remove the affected channels, we used the non-primary beam corrected images to determine the root-mean-square noise per channel. For each channel, we compared the noise to the median noise of the

[1] Due to the vagaries of data reduction, many datasets varied slightly from the ideal (e.g., missing stations, flagged out channels, reduced observing time, etc.). These variations did not affect the final data products significantly, so we do not list these minor variations.

[2] https://github.com/maaijke/RMextract/

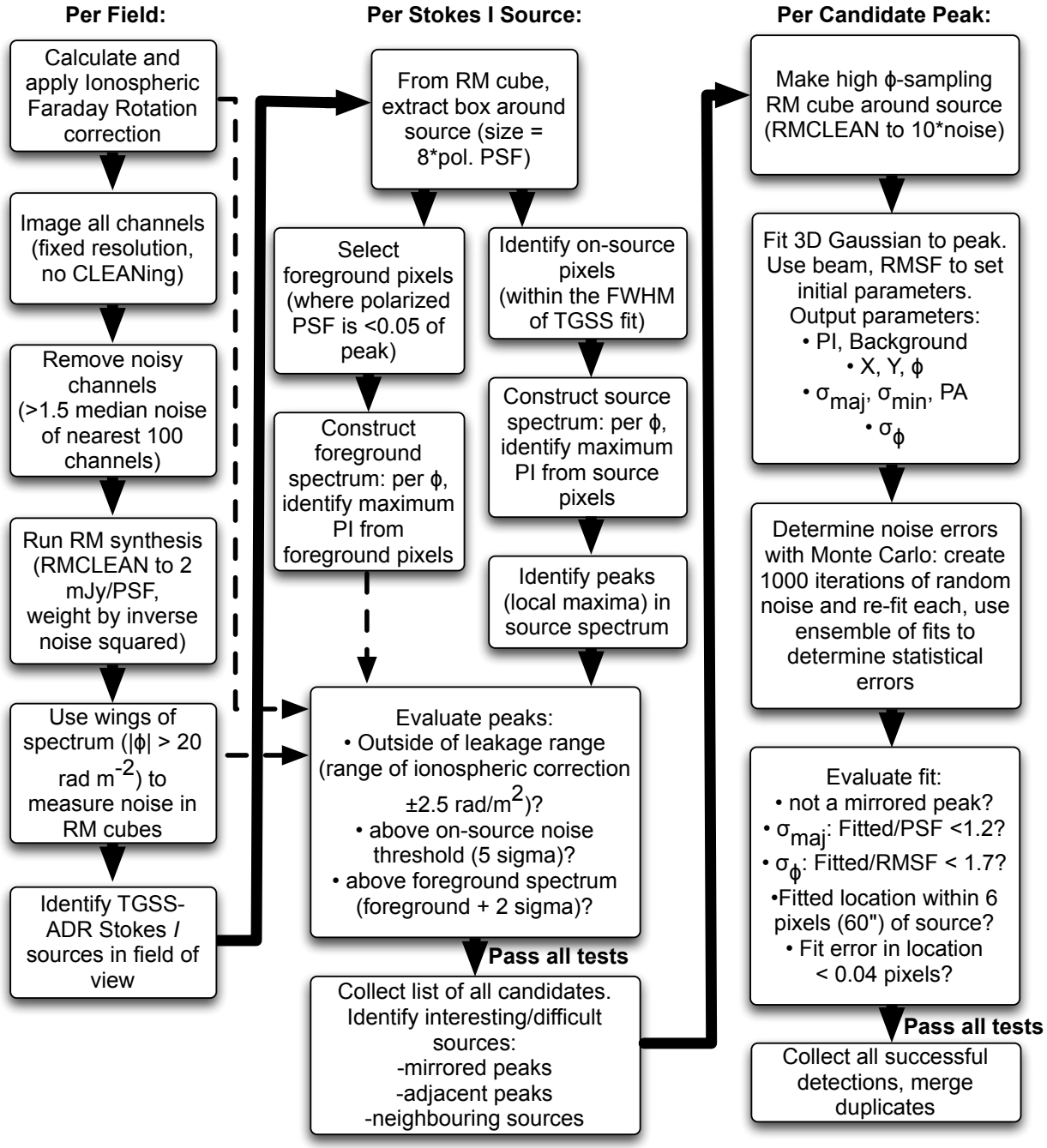

Figure 4.1: A flowchart showing the key steps in the data processing, with emphasis on the parameters used. Details of each step are given in the text.

100 adjacent channels; if the noise was more than 1.5 times the median, the channel was removed and not used for RM synthesis. This typically removed 2–10 channels, with a few fields losing 60–80 channels. The noise level in the remaining channels was typically between 2–4 mJy/beam. Three fields were found to have much higher noise levels in all channels due to the presence of polarization leakage from very bright 3C sources. These fields were dropped from the processing and did not have Faraday depth cubes made, leaving 60 fields for the remaining steps of the pipeline.

RM synthesis was done using the pyRMsynth software[3]. From the frequency coverage of the data, the FWHM of the rotation measure spread function (RMSF) is 1.15 rad m^{-2}, and the observations have much reduced sensitivity to Faraday depth structures wider than 1.0 rad m^{-2}. The consequence of this is that we are not able to resolve structures in Faraday depth that are wider than the RMSF, as they would be strongly depolarized at these frequencies, and that the polarized emission we do detect must be Faraday thin. The channels were weighted by the inverse of the noise squared, equivalent to natural weighting in radio imaging. The nominal theoretical noise in the resulting Faraday depth cubes, assuming 480 channels with 3 mJy/beam noise, is 0.14 mJy/beam/RMSF.

For each field, Faraday depth cubes were produced that covered the Faraday depth range $|\phi| < 100$ rad m^{-2}, in steps of 0.5 rad m^{-2}. RM-CLEAN was applied with a conservative threshold of 2 mJy/beam. No correction for spectral index was applied, which may introduce polarized intensity errors of 2–5% [Brentjens & de Bruyn, 2005].

No correction was made for the instrumental polarization leakage, as no method has yet been developed for removing this effect from LOFAR data. The polarization leakage caused part of the total intensity emission to appear as artificial, frequency-independent polarized emission, producing a peak in the Faraday spectrum at 0 rad m^{-2}. However, the ionospheric correction had the effect of shifting the Faraday depth of both the astrophysical and instrumental polarization. Since the ionospheric Faraday rotation ranged from 0 to 2.8 rad m^{-2} between observations, the leakage peaks were shifted to negative values by the same amount for all the sources in the same observation.

To determine the position-dependent noise level in the resulting cubes, we used the following method. For each image-plane pixel, the Faraday depths $|\phi| < 20$ rad m^{-2} were masked out, and the histogram of polarized intensity values from the remaining regions of the Faraday spectrum was constructed. A Rayleigh distribution (which is the expected distribution of polarized intensity in the absence of signal) was fit to this histogram, and the resulting Rayleigh σ parameter (which is the equivalent for the Gaussian σ of the underlying Stokes Q and U distributions) was taken as the noise. An alternative method, where the histograms of the Stokes Q and U distributions were fit with Gaussians, was also tested and found to give the same results. The masked Faraday depth range was selected to include all of the observed diffuse emission (as well as the polarization leakage peak) in order to remove all the Faraday depths at which signal was expected.

The noise measured with this method was observed to be position dependent in two respects. First, the noise increased smoothly with distance away from the phase center in each field, due to the effects of the station beam correction applied by AWimager. Second, the noise was observed

[3]https://github.com/mrbell/pyrmsynth

to be higher at the location of bright Stokes I sources. This suggests that even though the polarization leakage is mostly confined to Faraday depths near zero, there is still contamination even in the wings of the Faraday spectrum. The result of this is that the on-source noise is significantly higher than the off-source noise, and that position-dependent noise estimates are necessary to properly characterize these data.

4.2.2 Source candidate identification

After the Faraday depth cubes were produced, the next step was to search for polarized source candidates. Source-finding directly on the polarization data was considered and rejected; a discussion on the problems of source-finding in polarization can be found in Farnes et al. (submitted). Instead, we chose to search for polarization only at the locations of known Stokes I sources. At that time, the LOTSS catalog [Shimwell et al., 2017] was not available, so we used the TGSS-ADR1 catalog of sources [Intema et al., 2016], as this was the most sensitive catalog available at the same frequency.

At this stage, the problem of diffuse foreground contamination was considered. Diffuse polarized foreground was seen at nearly all positions in the Faraday cubes, at levels of up to 10 mJy/PSF/RMSF, making it necessary to develop some method of removing it or otherwise preventing it from being spuriously associated with the background sources. We first considered foreground subtraction methods, where the foreground contribution is calculated from neighbouring off-source pixels and subtracted from the on-source Faraday spectrum to give the Faraday spectrum of just the source. These methods were rejected, as we found that the foreground varies strongly with position and it was not possible to accurately determine the on-source foreground contribution. We instead chose to use foreground-thresholding: we used the neighbouring off-source pixels to measure the strength of the foreground in that region (as a function of Faraday depth), and required that the on-source polarization be significantly stronger than this to be classified as a detection.

For each field, a list of TGSS-ADR1 sources inside the field was generated. For each source, a box centered on the source was extracted from the Faraday depth cube, with a size of 8 $\sigma_{\rm maj}$ for each axis in the image plane and covering the full Faraday depth range of the cube, where $\sigma_{\rm maj}$ is the width of the major axis of the image-plane PSF (expressed as a Gaussian σ). This width is equivalent to 3.4 times the FWHM of the PSF. Sources too close to the edge of the cube for this box to be extracted were discarded.

The TGSS-ADR1 fitted source size was overlaid on this box, and pixels within the source FWHM were classified as 'on-source' pixels for the next step. The polarized PSF was overlaid on the box (positions of all TGSS-ADR1 sources within the box), and all pixels below 5% of the PSF peak were classified as foreground pixels for the next step.

The source Faraday depth spectrum was constructed by taking the maximum polarized intensity of the on-source pixels at each Faraday depth. The foreground spectrum was constructed in the same way for the foreground pixels around the source. The source spectrum was then searched for peaks, simply by identifying all the local maxima in the spectrum. Figure 4.2 shows four examples of source and foreground Faraday depth spectra constructed using this method.

From the noise map calculated in the previous section, the highest noise of the on-source pixels

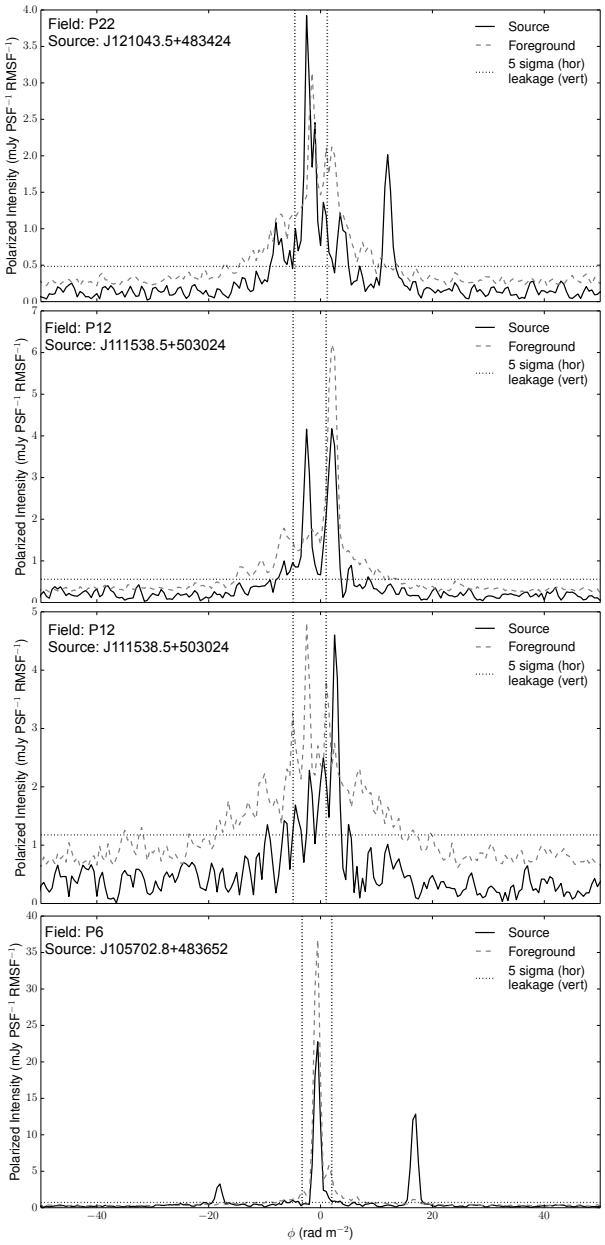

Figure 4.2: Four examples of Faraday depth spectra of different sources. For each, the source Faraday spectrum and foreground Faraday spectrum are shown in black and grey respectively, the 5-sigma (noise level) is marked in a horizontal dotted line, and the excluded Faraday depth range around the instrumental leakage is bounded by vertical dotted lines. The four spectra were selected to show examples of different phenomena: *Top:* a typical positive detection, with a clear bright source at +12 rad m^{-2}; *2nd:* A source with bright foreground (both on-source and off-source) at +3 rad m^{-2}, showing the need to consider the foreground emission when identifying sources; *3rd:* a false detection (which failed later tests) at +3 rad m^{-2}, which can be seen in the full 3D cube to be a local enhancement in the foreground emission; *Bottom:* a real detection at +17 rad m^{-2} with an artificial 'mirrored' peak at -18 rad m^{-2}.

was selected as the noise at the source location. For each peak, a series of tests was applied to select candidate detections. The first test was that a peak must have polarized intensity greater than 5 times the noise. This removed low-intensity noise-like peaks. The second was that the peak must have a polarized intensity greater than the foreground spectrum plus two times the noise. This removed most peaks caused by foreground diffuse polarization. The third test was that the peak had to be clearly separated from the instrumental leakage peak. Peaks that were within 2.5 rad m^{-2} of the range of values for the ionospheric correction were rejected. The free parameters in these tests were tuned manually to minimize the number of false detections while not removing any peaks that looked promising to a by-eye inspection. This process resulted in 814 candidate peaks; this number contains both sources appearing in multiple fields (due to overlap in the image-plane) and sources with multiple peaks in Faraday depth.

The Faraday depth cubes were too coarsely sampled in Faraday depth for high-accuracy measurements, so for each source with one or more candidate peaks a new postage-stamp Faraday depth cube was produced. These cubes had image-plane dimensions equal to the size of the box used in the previous step, and covering Faraday depths in the range ± 100 rad m^{-2} in steps of 0.1 rad m^{-2}. RM-CLEAN was performed to a threshold of 10 times the source noise. From these Faraday cubes, the Faraday depth range ± 2 rad m^{-2} around each candidate peak was extracted and used to fit the peak.

The fitting function used was a 3D Gaussian, formed by multiplying a general 2D image-plane Gaussian with a 1D Faraday depth Gaussian. A non-zero background level, added in quadrature with the Gaussian, was also included as a free parameter, resulting in a 9-parameter model for each peak: a peak polarized intensity (P), a background polarized intensity (C), the image-plane centroids (X and Y, in pixel coordinates), the image-plane semi-major axis ($\sigma_{\rm maj}$), semi-minor axis ($\sigma_{\rm min}$), and position angle (PA), the Faraday depth centroid (ϕ), and the Faraday depth width (σ_ϕ).[4]

The 'curve_fit' task from the Python SciPy module was used for the fitting procedure. The initial guess parameters, in the same order as above, were the peak polarized intensity from the previous cube, the source noise, the TGSS-ADR1 source location, the image-plane PSF size and orientation, the peak Faraday depth from the previous cube, and the RMSF width. For each peak, the best-fit parameters and the fit errors reported by SciPy were recorded. Peaks where the fitting algorithm failed to converge were labeled as false detections and discarded.

4.2.3 Error analysis

The fit errors produced by SciPy were not useful, as they were unrealistically small in nearly all cases (for example, typical errors in centroid position of a few hundredths of a pixel). This is due to the underlying assumptions used in calculating those errors; it is assumed that each data point (in this case, each voxel of the Faraday cube) is independent of the others and has its own Gaussian error distribution. Using this assumption, the chi-squared statistic and the fit covariance matrix are used to calculate the errors in the fitted parameters.

[4]The three width parameters were kept as Gaussian σ, rather than expressed as FWHM. This convention will be followed throughout the paper unless otherwise specified.

However, with interferometric/RM synthesis data, adjacent pixels/Faraday depths are not independent due to the effects of the PSF/RMSF. The errors in neighbouring data points are correlated with a characteristic scale related to the size of the PSF/RMSF. The result is that the number of effective independent degrees of freedom is much smaller than what is assumed, so the derived errors are much smaller than the true errors.

To derive more reasonable errors, we attempted a different approach, using Monte-Carlo techniques. Bootstrapping methods were considered and rejected, as a naive approach to bootstrapping (such as simply randomizing the fit residuals) would not reproduce the correlation structure of the noise. Instead, we chose to create randomized realizations of noise with correlation structure as close to the real noise as possible, and simulate the fitting procedure on these noise realizations.

To produce simulated noise with the correct characteristics, we considered the source of the noise in the data. During the imaging process, the input visibilities contain noise, so each grid-point in the (u, v) plane that contains visibilities will also have an associated noise (this noise is generally estimated for weighting purposes), which should be independent of other points. Unfortunately, the imager software does not provide access to these noise values. Without this, the only information we had on the correlation structure in the data is the PSF. We performed an FFT of the 3D PSF+RMSF to recover the distribution of Fourier components in the PSF. Each component was then multiplied by a random number drawn from a Gaussian distribution with zero mean and a standard deviation of 1. The resulting randomized Fourier components were transformed back to the image plane and the imaginary component discarded, producing a randomized noise realization with correlation structure that appeared very similar to the real data. The amplitude of the noise realization was then scaled so that the standard deviation matched the source noise.

For each source, 1000 such random noise realizations were created. Each realization was added to the best-fit model, a new fit was performed, and the resulting fit parameters were recorded. For each fit parameter, the standard deviation of the 1000 simulated fits was used as the estimated error caused by noise. For all parameters, the noise error was typically 30–100 times greater than the fit error, so the noise errors are taken to represent the true uncertainties on the fit parameters.

There are at least 3 issues with this method that we were not able to address. First, the use of the PSF and RMSF to determine the Fourier components of the noise is not correct. The Fourier transform of the PSF/RMSF should be equal to the weights used in the imaging/RM synthesis processes, rather than the noise. The weights will not be proportional to the noise, and for some weighting schemes (e.g. natural weighting) will actually be anti-correlated with the noise value for each Fourier component. For this reason, the PSF/RMSF will show which Fourier components are present in the data, but will not give the correct relative amplitudes.

Second, since this method combines the noise realization with the best-fit model to produce a new simulated dataset, it does not take into account any uncertainties that result from unfitted structure in the real data (i.e. in the residuals). Any non-Gaussianity in the real data, which could affect the estimation of fit parameters, is not accounted for in this process (but, instead, probably appears into the fit errors output by SciPy's curve_fit).

Third, the resulting noise, and its combination with the best-fit model, do not follow the proper statistical distributions for polarized intensity. The simulated noise has a Gaussian dis-

tribution, while polarized intensity should follow a Ricean distribution. For high signal-to-noise cases the current method should be very close to accurate (as the Ricean distribution becomes more Gaussian-like), but for lower signal cases and for the off-source voxels the difference will be greater. A more careful treatment using the full complex polarization would resolve this problem, as the real and imaginary components of the polarization are observed to follow Gaussian distributions like we were simulating so the proper statistics for the polarized intensity would emerge naturally.

Despite these unresolved problems, we consider the resulting uncertainties to be the most accurate estimation available for the true uncertainties in our measured fit parameters, largely due to the lack of any other methods.

4.2.4 Candidate evaluation

Of the 814 candidate peaks, 51 failed to be fit leaving 763 fits. A large number of these were clearly not real polarized sources (e.g were indistinguishable from adjacent foreground emission, were clearly separated in position from the Stokes I source, or appeared to be sidelobes of the instrumental leakage), so additional selection tests were necessary to separate the reliable detections from the probable false detections.

To determine what tests could be applied to make this separation, it was first necessary to have a population of real and false detections. Each of the candidate peaks was inspected manually, both in the source Faraday spectrum and in the 3D Faraday cube. The candidates were classified as either clearly real, clearly false, or ambiguous, and were further classified as either isolated (without any other candidates nearby in position and Faraday depth) or with a neighbouring candidate.

This inspection produced 129 isolated real candidates, 63 isolated ambiguous candidates, 444 isolated false detections, 88 real candidates with neighbour(s), 24 ambiguous candidates with neighbours, and 66 false detections with neighbours. This manual inspection process was not considered acceptable for deciding membership in the final catalog, but instead was used to determine which quantitative selection tests would be most effective.

The first test was to remove candidates that were 'mirrored peaks', a type of instrumental artifact seen in some Faraday spectra. Some Faraday spectra that contained a bright real peak and a strong leakage peak would have a third, weaker peak on the opposite side of the leakage peak from the real peak and with the same separation in Faraday depth, giving the appearance of being 'reflected' across the leakage peak. The bottom panel of Figure 4.2 shows an example of such a Faraday spectrum. To identify these mirrored peaks, we checked each candidate for the presence of a counterpart candidate on the opposite side of the leakage peak. If such a counterpart was found, the peak with the weaker polarized intensity was discarded.

The next two tests were to discriminate between unresolved point-sources and sources that appeared extended in either the image plane or in Faraday depth. Due to the poor image-plane resolution of the polarization data and the strong presence of diffuse foreground, we made the assumption that any fit that deviated significantly from the PSF was much more likely to be a diffuse polarized feature than an extended polarized background source. The properties of the RMSF meant that we were not sensitive to resolved structures in Faraday depth, so fits significantly

broader than the RMSF were interpreted as being unphysical. To determine which parameters and thresholds were effective in discriminating between real and false sources, we compared the distributions of the sources identified by-eye as isolated real sources to those identified as isolated false detections. We found that the fitted major axis ($\sigma_{\rm maj}$) and Faraday depth width (σ_ϕ) were the most effective discriminants. The fitted minor axis and position angle were not found to provide a useful distinction between real and false detections. Sources with $\sigma_{\rm maj}$ greater than 1.2 times that of the PSF or with σ_ϕ greater than 1.7 times that of the RMSF were rejected.

The next test checked that the position of the polarized source corresponded with the position of Stokes I counterpart in the TGSS-ADR1 catalog, as it was expected that most spurious detections caused by foreground polarization would not be centered on the source location. For each candidate, the image-plane separation between the fitted centroid and the TGSS-ADR1 centroid was calculated, and the distribution for real and false isolated candidates was used to determine the best threshold. Based on these distributions, we rejected all candidates where the separation was greater than 1 arcminute (6 pixels).

We found that several of the fit errors were very powerful discriminants between real and false candidates. As described in the previous section, these errors were unphysical, but they appeared to still be sensitive to the quality of the fit. Our interpretation is that large fit errors are mostly likely caused when significant non-Gaussianities are present, and this is often a sign that the polarization is diffuse foreground instead of from the background source. After looking at the different fit errors, the most effective test appeared to be the position error (the X and Y centroid errors added in quadrature). Candidates with position errors larger than 0.04 pixels were rejected. Figure 4.3 shows how effective this test was in discriminating between candidates that did not pass the manual inspection; the fitted position error and the major axis were the most effective tests, together removing 80% of the false detections.

After this test, we found that 113 of the 129 isolated real detections and 10 of the 444 isolated false detections passed all tests. We were unable to find any additional tests that could remove the remaining false sources from the sample, and considered this to be an acceptable false-detection rate. The tests described above were applied to all candidate peaks, resulting in 197 detections. Due to the overlap between adjacent fields many sources were detected multiple times, so the number of unique TGSS-ADR1 sources with detections is 103.

4.2.5 Catalog verification

The multiple detections of many sources offered an opportunity to verify the reliability of the measurements. This allowed us to assess the consistency of the by-eye inspection and quantitative tests used to assess the candidate polarized sources, check if the calculated noise errors are reasonable, and check the accuracy of our Faraday depth measurements.

We limited our investigation to sources where at least one candidate detection passed all tests (i.e. the 103 sources reported in the previous section). Of these sources, 36 sources had 2 candidate detections, 25 had 3 detections, and 14 had 4 detections.

The manual inspection was shown to be quite self-consistent: of the 36 double-detections, 19 had both candidates classified as real, 6 were classified as real once and ambiguous once, 5 were double-ambiguous, 4 were both classified as false, and 2 were classified as false once and ambiguous

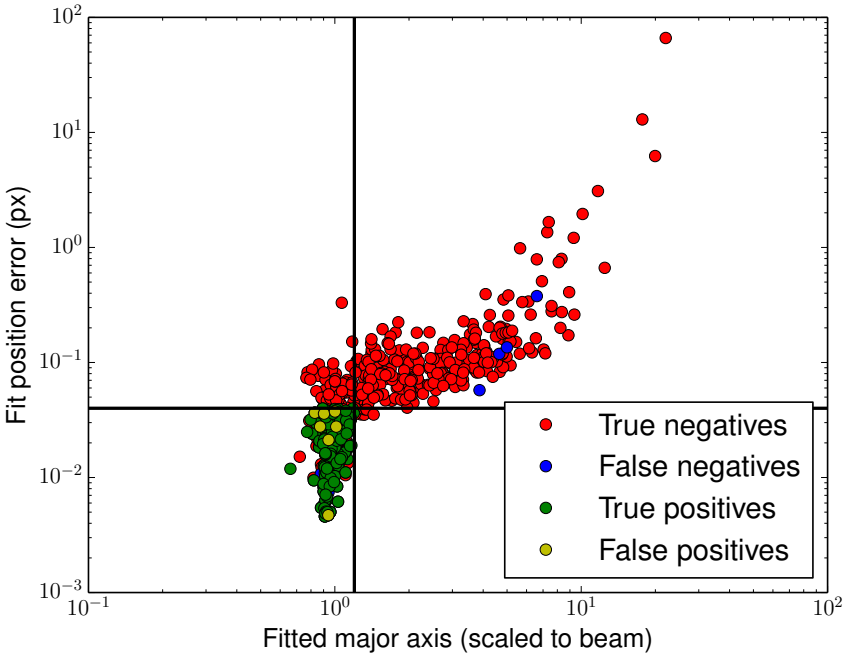

Figure 4.3: Two of the tests to determine which sources were real: the size of the fitted major axis relative to the PSF (horizontal axis) and the error in position from the fit (vertical axis). The black lines show the test thresholds: 1.2 times the fitted major axis size and 0.04 pixels position error. Each point is a candidate source, colored by how it was evaluated by the tests (positives passed all tests, negatives failed one or more tests, including the tests not shown) and the manual inspection (true positives/negatives where the tests match the manual inspection, false where the tests don't match the manual inspection).

once. None had conflicting real-false classifications. Of the 25 triply detected candidates, 10 had all 3 candidates classified as real, 9 were a mixture of real and ambiguous, 3 were triply-ambiguous, 2 had a mixture of ambiguous and false classifications. One source had two false classifications and a real classification. Of the 14 sources detected as candidates in 4 fields, 9 were classified as real for all 4 fields and 2 were a mixture of real and ambiguous. Three contained a mixture of real, false, and ambiguous.

Similarly, for the quantitative tests described previously: Of the 36 double-detections, 24 passed both in both fields, while 12 passed in only one. Of the 25 triple-detections, 12 passed 3 times, 6 passed twice, and 7 passed only once. Of the 14 quadruple-detections, 8 were passed all 4 times, 4 passed 3 times, 1 passed twice, and 1 passed once.

To assess the consistency of the Faraday depth measurements, and to determine whether the repeated detections that failed the tests were still useful, we looked at the variations in the fitted Faraday depth. For each source with two or more candidate detections, we calculated the mean and mean-subtracted residuals in Faraday depth. The resulting distribution was divided by whether the source passed the quantitative tests, and is shown in the top plot of Figure 4.4. This figure shows that the sources that passed the quantitative tests are all very consistent with each other, while those that did not are mostly consistent but show a few outliers that vary significantly from the other detections. We removed all the 'fails' from the calculation of the mean ϕ for each

source, which produced the distribution shown in the bottom plot of Figure 4.4. This clearly shows that the sources that did not pass the tests often show significant Faraday depth variations from the passing detections. From this result, we concluded that these detections were combined to produce a single catalog entry per source, the failed detections should not be used, in order to maximize the reliability of the catalog.

From Figure 4.4 we were also able to assess the night-to-night variations in the ionospheric Faraday rotation correction. Uncertainties in the ionospheric Faraday rotation should manifest as systematic shifts in the measured Faraday depths of all polarized emission in each observation. The observed differences between detections of the same source in different observations should be due to a combination of this effect and the random noise error. Considering the residuals from the population of passes from the lower plot of Figure 4.4 gives a standard deviation of 0.068 rad m^{-2}. The root-mean-square noise error in ϕ for the same candidates is 0.049 rad m^{-2}. The two sources of uncertainty (noise and ionospheric correction) should be independent, so subtracting the noise-error from the observed error in quadrature yields an estimated correction uncertainty of 0.047 rad m^{-2}. This is smaller than the 0.1-0.3 rad m^{-2} estimated by Sotomayor-Beltran et al. [2013]. We interpret this difference to mean either the ionospheric correction uncertainty is smaller than expected, or a significant portion of the uncertainty is systematic and effects all observations equally.

To test whether the estimated noise errors were realistic, we performed a similar analysis as above, but replacing Faraday depth with right ascension and declination. These were chosen as they were expected to not suffer from any polarization-specific problems, and during the noise simulations they were observed to have normally-distributed errors. For both right ascension and declination separately, and using only the passed multiply-detected candidates, we computed the mean, residuals, and the noise error on the residuals. The residuals, normalized by their calculated noise error, were expected to follow a normal distribution with unit variance. The results are shown in Figure 4.5. The right ascension distribution has an unexplained peak at zero, but otherwise both distributions are well represented by a normal with unit variance. We calculated the standard deviation for each distribution as 1.06 for right ascension and 1.10 for declination, which suggests that the noise errors we calculated may be slightly underestimated by a few percent. Since this difference is quite small, we chose to leave the errors as recalculated, with no rescaling.

The final step to produce the final catalog was to combine the multiple detections into single catalog entries. For each source with multiple detections, the positions, polarized intensities, and Faraday depths were averaged using only those detections that passed all quantitative tests. The noise errors on these quantities were averaged in quadrature. During this process, we found that there were overlapping detections within the individual fields, caused by very closely spaced TGSS-ADR1 sources. In a few cases where the source locations were close enough, the polarized peak would occur between the two sources and would be close enough to the TGSS-ADR1 source locations to pass the position test for both. This would result in two detections with the same fitted location in polarization, but matched to different TGSS-ADR1 sources. We identified 7 cases where this occurred (and both detected passed all tests). Since these represented duplicate measurements of the same data, the detection with the larger distance to its TGSS-ADR1

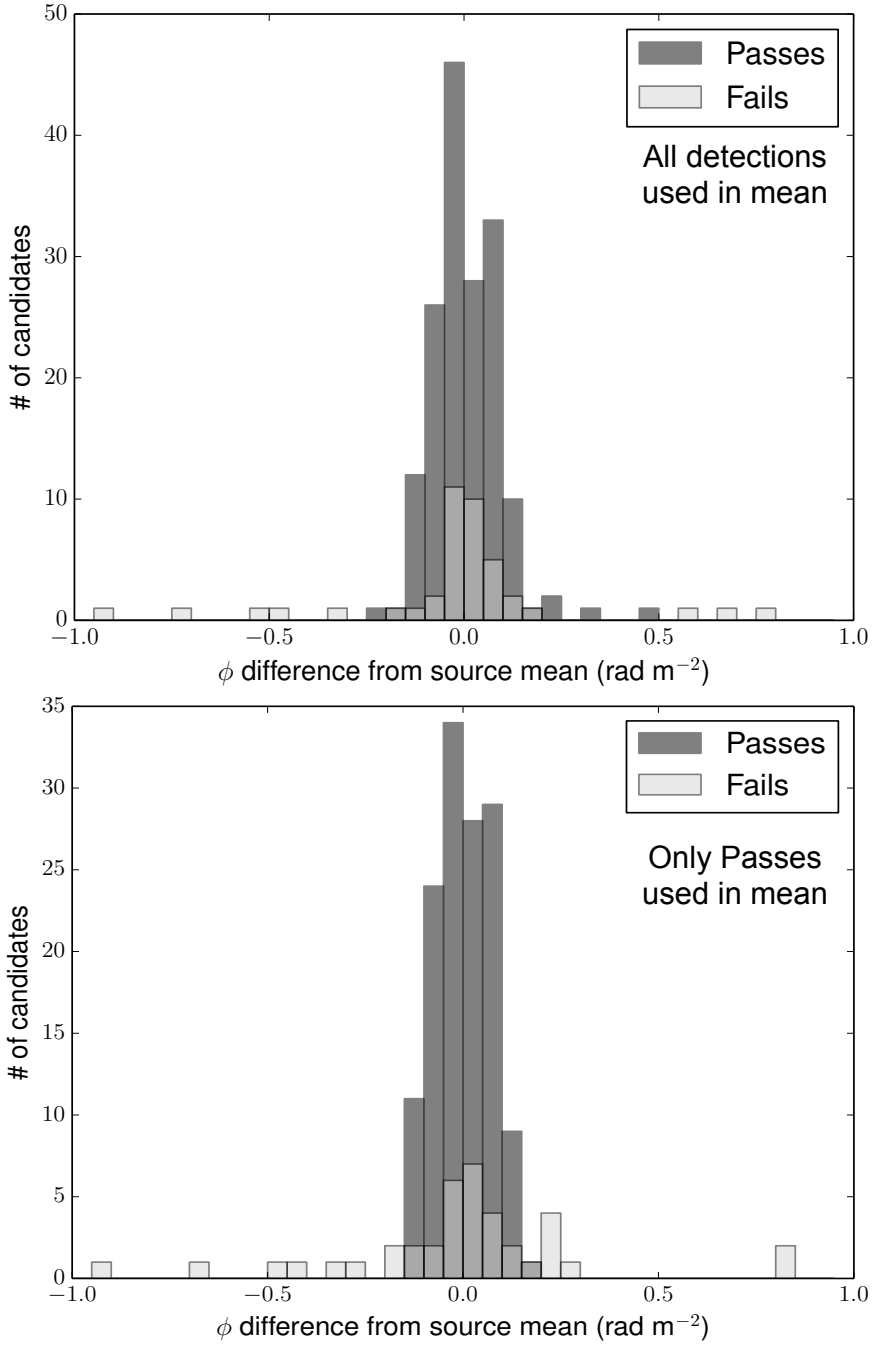

Figure 4.4: Histograms of the mean-subtracted residual Faraday depth for sources with multiple candidate detections from different observations, where the mean is calculated using all candidates (*top plot*) or only with those source that passed the quantitative tests (*bottom plot*). The candidates are separated by whether they passed the quantitative tests or not (each source must have at least candidate detection that passed all tests).

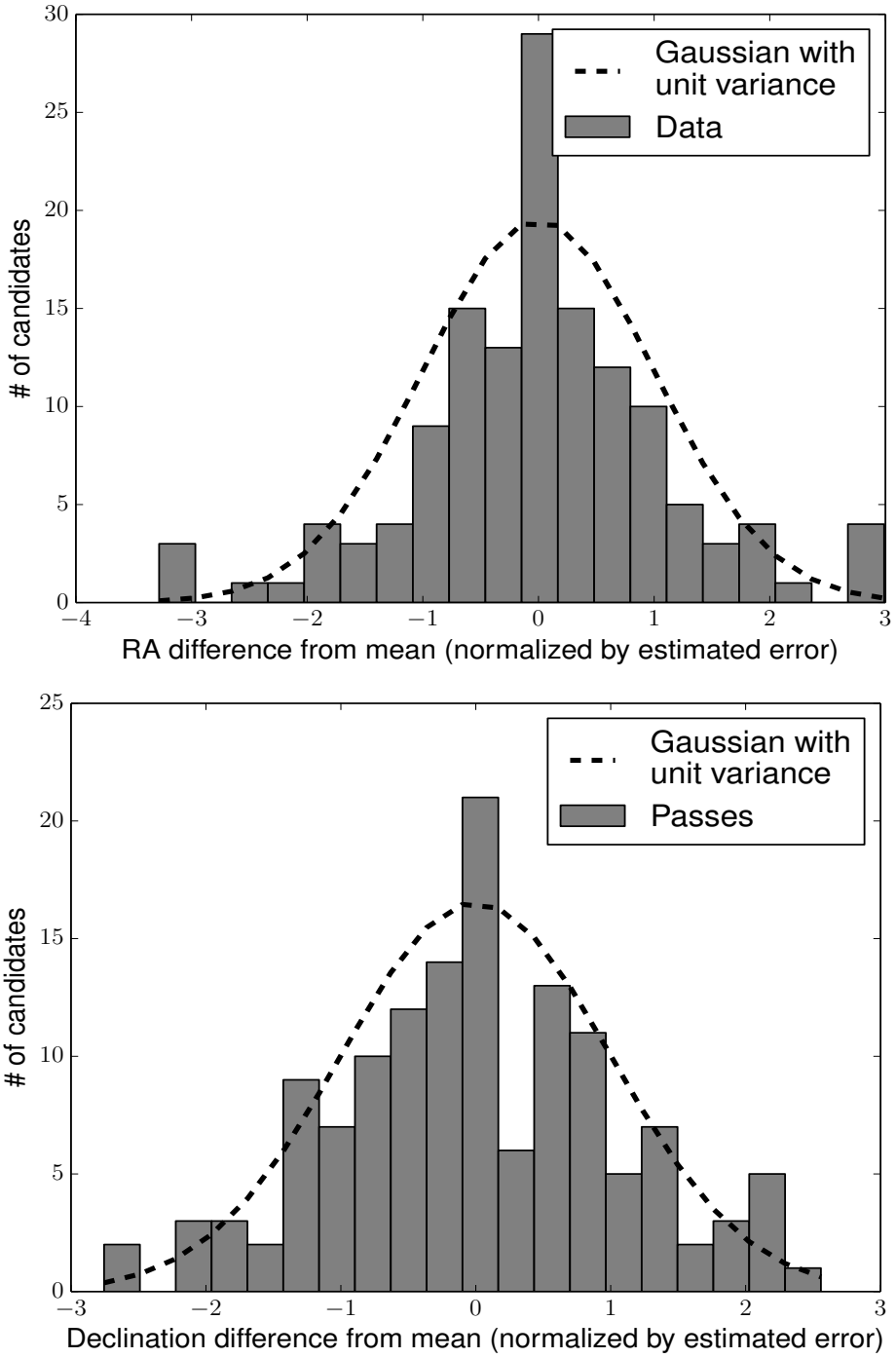

Figure 4.5: The distributions of offsets in position (right ascension (top) and declination (bottom)) from the mean for multiply-detected sources. For each source with 2 or more detections (that passed all tests), the mean-subtracted residuals of position for each detection were calculated. The residuals were normalized by the errors calculated from the Monte Carlo noise simulations (a correction was included for the error in the mean), and the resulting distributions are shown. The dashed lines are normal distributions with a variance of 1.0 and normalized to the total number of detections (no fitted free parameters). Both data distributions fairly closely follow the normal distribution (except for an unexplained peak at very small differences), indicating that the errors are well behaved and accurately estimated.

counterpart was removed in each case.

4.3 Polarized source catalog

The processing and selection steps described in the previous section resulted in a catalog of 102 polarized sources. One source matched the ATNF pulsar catalog [Manchester et al., 2005][5], and was removed from the main catalog. The 101 remaining sources are given in Table 4.1, and the pulsar is given in Table 4.2. Figure 4.6 shows the positions and Faraday depths of these sources; the total area covered is approximately 570 square degrees. The position, polarized intensity, and Faraday depth of each source were taken directly from the 3D fit parameters described previously, except for sources with multiple detections where the parameters from these detections were averaged as described above. The errors in each of these parameters were taken to be the noise errors calculated previously. No correction for polarization bias [Simmons & Stewart, 1985] was applied. The Faraday depth measurements, in addition to the reported random error, will have an additional systematic error introduced by the ionospheric Faraday rotation correction. The analysis above suggests that this error is about 0.05 rad m^{-2}, but Sotomayor-Beltran et al. [2013] suggest it may be between 0.1–0.3 rad m^{-2}.

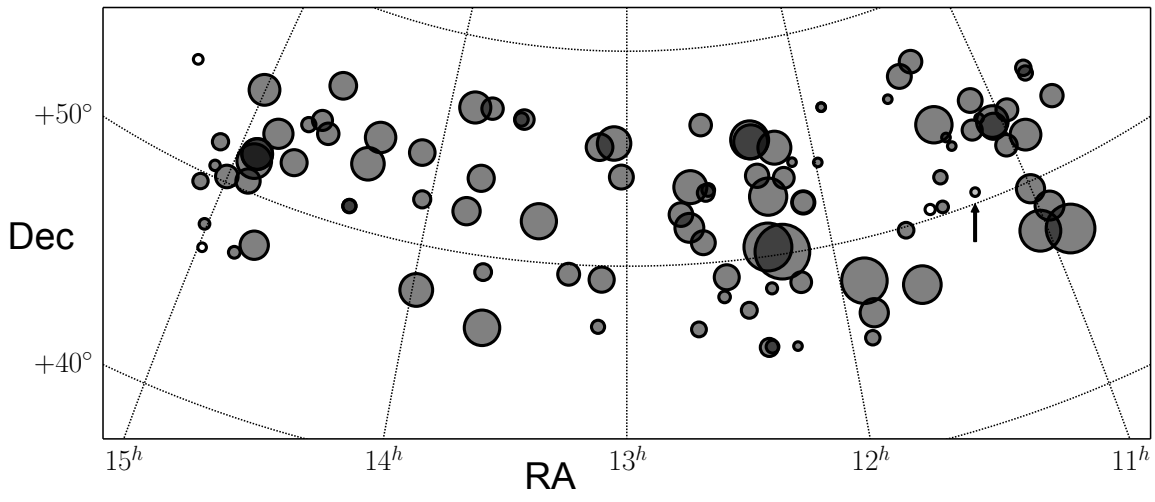

Figure 4.6: The positions and Faraday depths of all polarized sources in the catalog. The size of each symbol is proportional to the magnitude of Faraday depth (sources with $|\phi| < 3$ rad m^{-2} are set equal in size to 3 rad m^{-2}; the largest circle is 32 rad m^{-2}) while open and filled circles represent negative and positive Faraday depths respectively. The single pulsar (B1112+50) is marked with an arrow.

[5]http://www.atnf.csiro.au/people/pulsar/psrcat/

4.3.1 Comparison with NVSS rotation measures

To compare our low-frequency Faraday depth measurements to higher frequency measurements, we cross-matched our sources against those in the catalog of Taylor et al. [2009], which used 1.4 GHz observations. Their catalog had 910 sources in the same area as ours. Using a cross-matching limit of 1 arcminute, we identified 55 sources that appeared in both catalogs. The top panel of Figure 4.7 compares the measured Faraday depths between the catalogs. The two catalogs are in approximate agreement, with a large scatter. The bottom panel of Figure 4.7 shows the distribution of Faraday depths for all sources in the HETDEX region from each catalog. Our catalog has a much narrower distribution, likely due to the smaller errors on the Faraday depth measurements, and a notable absence of sources near 0 rad m^{-2}, which is due to candidate detections near to the instrumental leakage (typically between 0 and -2 rad m^{-2}, due to the ionospheric correction) being deliberately excluded in our analysis. As a result, our catalog is almost certainly incomplete, and biased against very low Faraday depths.

We performed a chi-squared test of the difference in Faraday depth between the two catalogs, and found a reduced chi-square statistic of 3.9 (indicating a root-mean square residual of about 2 σ_ϕ), suggesting that the scatter is significantly larger than we would expect from the errors. While there are some suggestions that the errors in the Taylor et al. [2009] catalog are underestimated [Stil et al., 2011], that is not expected to be significant enough to cause this. One plausible explanation is that many of these sources possess some Faraday-thick (by LOFAR standards) polarized emission, which would be strongly depolarized at LOFAR frequencies but could still contribute at 1.4 GHz. Many background polarized sources show this sort of broad Faraday structure, but it requires very broad bandwidth observations, including much higher frequencies, to measure such structure [Anderson et al., 2016].

4.4 Analysis

Below we consider a few calculations that can be made using the values from our catalog.

4.4.1 Polarized source counts

While our catalog is incomplete, due to the effects of the instrumental leakage and beam depolarization, we can still make an approximate estimate of the polarized source density. The total area covered by our observations, accounting for overlap between fields, is approximately 570 square degrees, with a typical 5-sigma sensitivity of 1 mJy PSF^{-1}. Therefore, without making any corrections for incompleteness, the 102 polarized sources (including the pulsar) in our catalog gives a polarized source density of 0.18±0.02 sources per square degree, or 1 source per 5.6 square degrees.

For comparison, Mulcahy et al. [2014] found 6 polarized sources in a single LOFAR observation, with an area of 17.3 square degrees, giving a polarized source density of 0.35±0.14 sources per square degree, or 1 source per 2.9 square degrees.[6] This value is significantly higher than ours,

[6] Mulcahy et al. [2014] give their source density as 1 per 1.7 square degrees, which is much higher. They may have made a correction due to the reduced sensitivity at the edges of the primary beam, but they do not describe how this was done.

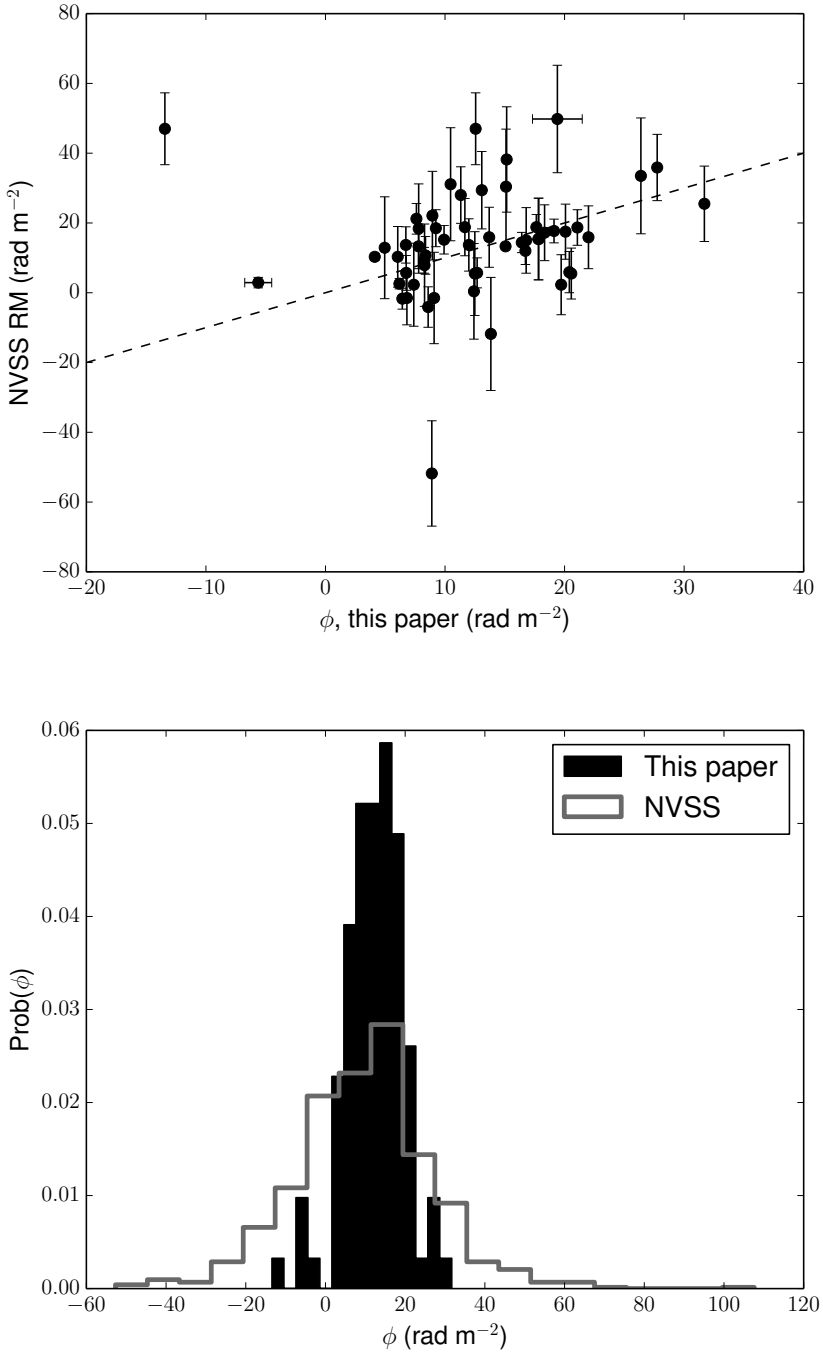

Figure 4.7: *Top:* A comparison of the measured Faraday depths between our catalog and the Taylor et al. [2009] catalog. The dashed line is the line of 1:1 correspondence. The errors in our measured Faraday depth are almost always much smaller than the symbol size. *Bottom:* The distribution of Faraday depths for our catalog and the Taylor et al. [2009] catalog. The absence of sources near 0 to -3 rad m^{-2} in our catalog is due to our procedure of ignoring the Faraday depths very close to the instrumental leakage.

but could be affected by small-number statistics. Bernardi et al. [2013] searched for polarized sources with the MWA at 189 MHz, and found 1 source in 2400 square degrees, but with a much higher flux threshold of 200 mJy PSF^{-1} (for comparison, we found no sources above this threshold). Bernardi et al. [2013] also calculated, from previously published 350 MHz polarized source detections, that the typical source density at 350 MHz is roughly 1 source per 4 square degrees at a sensitivity of 3–12 mJy PSF^{-1}. Our slightly lower source density could easily be due to wavelength dependent depolarization processes.

4.4.2 Average magnetic field

Subject to certain caveats, it is possible to estimate the average parallel magnetic field strength by using the relationship between the rotation measure/Faraday depth ($0.812 \int n_e B_\parallel dl$) and the dispersion measure (DM $= \int n_e dl$). Specifically, under the assumption that the magnetic field and the free electron density are statistically uncorrelated, the electron density-weighted average magnetic field is defined as $\langle B_\parallel \rangle = 1.232\,\phi/\mathrm{DM}$ [Sobey et al., 2010].

For the single pulsar, B1112+50, the reported DM is 9.18634±0.00026 pc cm^{-3}[Bilous et al., 2016], and the measured Faraday depth is +2.69±0.06 rad m^{-2},[7] giving an estimated $\langle B_\parallel \rangle$ of 0.36±0.02 μG. From the YMW16 electron density model [Yao et al., 2017], the estimated distance of this pulsar is 0.97 kpc.

For the remaining sources, no DM measurements are available, but it is possible to estimate the DM using Galactic electron density models. The YMW16 electron density model predicts DMs between 20 and 24 pc cm^{-3} for lines of sight in this region, integrating out to 30 kpc (we assume our sources are extragalactic, aside from the known pulsar, and that the DM contributions are negligible beyond 30 kpc). For comparison, the NE2001 model [Cordes & Lazio, 2002] predicts DMs between 28–31 pc cm^{-3}. We chose to take the typical (extragalactic) dispersion measure in this region as 25±5 pc cm^{-3}. The Faraday depth distribution of our polarized sources has a mean of 12 rad m^{-2} and a standard deviation of 7 rad m^{-2}. Combining these values, we estimate the average parallel magnetic field strength as 0.6±0.3 μG.

However, the assumption of statistical independence between the magnetic field and the electron density is probably not accurate, especially for a high Galactic latitude field like this. Both the free electron density and the magnetic field strength decrease with distance from the Galactic plane, which will result in a correlation even in the absence of any physical effects that might cause the two to be related. As a result, this magnetic field strength is likely most representative of regions of highest electron density, near the Galactic plane just beyond the Local Bubble. The higher average magnetic field strength calculated from the extragalactic sources, compared to the pulsar, may suggest the magnetic field is more aligned with the line of sight (and thus has a stronger parallel component) beyond 1 kpc compared to the magnetic field within 1 kpc, since the total magnetic field strength is expected to decrease away from the Galactic plane.

[7] We have incorporated a systematic error of 0.05 rad m^{-2} in addition to the measurement error of 0.01 rad m^{-2}, to account for uncertainty in the ionospheric correction.

4.4.3 Fractional polarization distribution

In addition to the comparison of Faraday depths between our catalog and the Taylor et al. [2009] catalog, a comparison of the polarized intensity or fractional polarization is also possible. We choose to use the fractional polarization (ratio of polarized intensity to Stokes I), as this measurement removes the effects of spectral index and allows us to probe the frequency-dependent depolarization. To calculate the fractional polarization, we took the ratio of the measured polarized intensity and the integrated flux from the TGSS catalog. The top panel of Figure 4.8 shows the resulting comparison.

Having polarization measurements at multiple wavelengths allows us to look at wavelength-dependent depolarization effects. Since the sources are unresolved in both catalogs, the dominant source of depolarization will be depth depolarization. In our observations, Faraday depth structures thicker than about 1 rad m^{-2} are strongly depolarized, leaving us sensitive to only the Faraday thin (<1 rad m^{-2}) components; the sensitivity of the Taylor et al. [2009] catalog to Faraday thickness is not well defined, as they did not use RM synthesis and had data at only two broadly-separated frequencies, but probably includes Faraday thicknesses up to approximately 50–70 rad m^{-2} (for a Burn slab [Burn, 1966], this is the Faraday thickness of the first null at 1.4 GHz). With the fractional polarizations at each frequency, we can compute the Faraday thin fraction of the polarized emission by taking the ratio of our 150 MHz fractional polarization (which will contain only emission Faraday-thinner than 1 rad m^{-2}) to the Taylor et al. [2009] 1.4 GHz fractional polarization (which will contain all polarization Faraday-thinner than roughly 70 rad m^{-2}).

In the bottom panel of Figure 4.8 we show the distribution of the Faraday thin fraction for our sample. The majority of sources have very low Faraday thin fractions, with 50% of polarized sources having less than 10% of their polarization as Faraday thin and 90% of sources having less than 40% of their polarization as Faraday thin. There is a small population, about 10% (6 sources out of 55), that are mostly Faraday thin. Due to the lack of sensitivity to very broad structures in Faraday depth in the 1.4 GHz measurements, these values are upper limits to the Faraday thin fraction, as there could be additional broad components not seen in either observation; such broad components have been observed in a few sources [Anderson et al., 2016].

One interpretation of these two populations in the Faraday thin fraction is that they could represent different types of sources. For example, pulsars are expected, naively (i.e., without considering the frequency-dependent polarization properties of pulsar emission mechanisms), to be almost perfectly Faraday thin (we were not able to find compatible 1.4 GHz polarization data for our pulsar, and could not confirm that with our data). Galaxies, both edge-on and face-on, are expected to have a high degree of Faraday complexity and correspondingly high degree of Faraday thickness, while large radio lobes may have lower internal Faraday rotation and a correspondingly higher fraction of Faraday thin emission. Further investigation into the nature of these sources may yield interesting results.

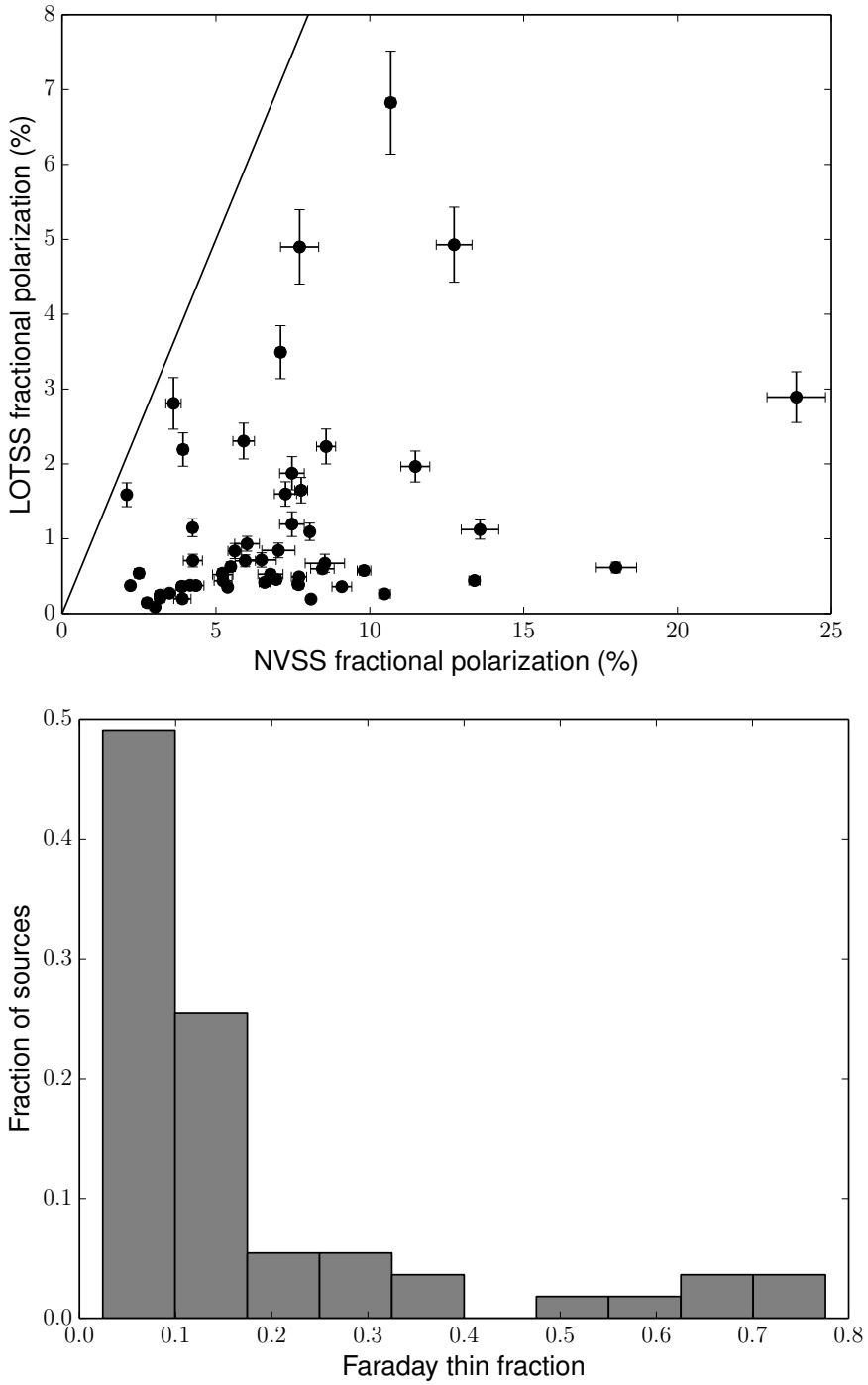

Figure 4.8: *Top:* Comparison of the fractional polarization (ratio of polarized intensity to total intensity) at 150 MHz (our catalog, vertical axis) and 1.4 GHz (Taylor et al. [2009] catalog, horizontal axis), for the 55 sources present in both catalogs. The black line marks 1:1 equivalence. All of the sources seen in the LOTSS data had lower fractional polarization than at 1.4 GHz, and most were less than 1% polarized at 150 MHz. *Bottom:* Histogram of the Faraday thin fraction, which is defined as the ratio of 150 MHz fractional polarization to 1.4 GHz fractional polarization, for the same sources. The majority of sources have low Faraday thin fractions, indicating that the majority of their emission is Faraday thick and is depolarized at low frequencies. However, there is a small population, about 10%, that show Faraday thin fractions above 50%, which indicates that they have much less internal Faraday rotation.

4.5 Discussion

The catalog presented here has shown that the LOTSS data is well suited for finding polarized sources. The full LOTSS will cover the full northern sky, with a total area approximately 37 times that of this test region, so we can expect the total polarized source count for this region to be of order 3700 sources. However, our catalog is almost certainly incomplete as described previously, so the source count for the full LOTSS would likely be higher.

4.5.1 Lessons for a larger LOTSS polarization survey

The polarization processing of this test region has highlighted a number of aspects in which the pipeline presented here could be improved. Here we summarize those aspects that we think would make the greatest improvement.

The single most limiting factor is the presence of the instrumental leakage. This puts a strong peak in the Faraday spectrum near zero, at the negative of the ionospheric leakage correction. While RM-CLEAN can strongly reduce the sidelobes from this peak, some residual contamination is still present (which we suspect is due to time-variability in the ionospheric correction), concentrated around 0 rad m^{-2} but extending all the way through the Faraday spectrum (this is reflected in the higher on-source noise). The ideal solution to this problem is to calibrate the visibilities for the polarization leakage, in the form of the so-called 'd-terms' in the interferometry measurement equation [Hamaker et al., 1996]. To date, there has been only limited work done on performing this calibration on LOFAR data.

If this calibration turns out to be impractical, alternative methods will need to be explored. One (highly speculative) possibility is to exploit the fact that the leakage is expected to be a perfect delta-function, shifted by (the negative of) the ionospheric correction and convolved with the RMSF. The time-variation in the ionospheric correction causes the leakage to be smeared out in Faraday depth, giving it structure that will not be properly removed by RM-CLEAN. It might be possible to determine the Faraday depth structure of the ionospheric correction, and convolve it with the RMSF (convolving it with the leakage delta-function is trivial) to predict the exact shape of the leakage in the Faraday spectrum. This shape could then be matched to the observed Faraday spectrum and subtracted off, in principle removing the leakage across the entire Faraday spectrum.

Another change that could significantly reduce the number of false detections would be to alter the imaging parameters to minimize the presence of the diffuse polarized emission. The parameters we used were optimized to maximize the sensitivity to diffuse polarized emission, which had the side-effect of making it more difficult to differentiate point sources from the diffuse foreground. The dominant effect of these parameters is the low image-plane resolution of our images. It should be possible to re-image at much higher resolution, to approximately 15–30 arcseconds using the data with only direction-independent calibration and perhaps even 5–10 arcseconds after direction-dependent calibration is complete (although at this time there have been no tests to see how direction-dependent calibration affects the polarization). Improving the resolution significantly should have three strongly beneficial effects. First, the diffuse polarization will become (relatively) much weaker, because the diffuse emission will be divided over many

more resolution elements while unresolved sources will still occupy only one resolution element. This will make it significantly easier to identify faint point sources at the same Faraday depths as the diffuse emission. Second, we expect a population of polarized sources with angular sizes between 4 arcminutes and 20 arcseconds [e.g. Orrù et al., 2015]; these sources likely suffer from significant beam depolarization due to different polarization angles across the source being averaged together. At higher resolution, gradients in the polarization may become resolved, removing part of the depolarization and resulting in a stronger polarized signal. Third, if the instrumental leakage cannot be removed (or is removed only incompletely), higher resolution should cause the leakage to be distributed over more resolution elements (as the instrumental leakage introduces an uncalibrated interferometric phase shift, resulting in on-source Stokes I emission becoming unfocused when leaking in Stokes Q and U), reducing the amount of on-source leakage in the Faraday spectrum.

To explore the data as deeply as possible, it would be advantageous to use a Stokes I source catalog made from the same observations as the polarization data. At the time of this work, such a catalog was not yet available, prompting our use of the TGSS-ADR1 catalog instead. This has the limitation that the TGSS-ADR1 catalog does not go as deep as our observations; during the manual inspection of the Faraday depth cubes a few possible polarized sources were found without TGSS-ADR1 counterparts. These were found to have Stokes I counterparts in the LOTSS data, but below the flux limits of the TGSS-ADR1. Using the same data for both the Stokes I and polarization catalogs would ensure that the sensitivity limits were more closely matched.

If the diffuse foreground and instrumental leakage can be reduced, the number of false detections should drop significantly and it should be possible to relax the pass/fail criteria on the source fit, or perhaps to even skip the source fitting step entirely. This would be very useful in retaining sources that deviate slightly from ideal point sources. These would include all sources that are resolved, which could be a significant population especially if the resolution is improved. While LOFAR observations are not sensitive to resolved structures in Faraday depth, it is possible to have multiple unresolved peaks in a single source. Several of these were observed in the manual inspection of the data, but none passed the pass/fail criteria. We suspect this is due to the presence of multiple peaks adjacent in Faraday depth affecting the Gaussian fit, perhaps causing it to create a fit broad enough in Faraday depth to cover both peaks, and then failing the σ_ϕ test. Being able to identify multiple-peaked sources would be an important improvement, as only low-frequency observations would have the Faraday depth resolution to study these sources.

While the processing of each observation independently allows us to compare the independent detections of sources and gives us a useful tool to verify our pipeline, it does not allow us to use the full sensitivity of the survey. By creating image mosaics from multiple observations, we could decrease the noise in the regions between pointing centers which would allow for faint sources, which might not be detectable in individual observations, to be identified.

The error analysis could also be improved, in the form of further developing the method of producing simulated noise as described in Section 4.2.3. This method should be properly investigated to ensure it produces reliable results and the unresolved issues described previously should be addressed.

4.6 Summary and proposed future analysis

We have used 60 observations from the LOFAR Two-Meter Sky Survey (LOTSS) HETDEX region to perform Faraday tomography and search for radio sources that are polarized at low-frequency. We developed a data reduction pipeline to produce polarization data products, with a correction for ionospheric Faraday rotation, from LOTSS observations, identify polarized sources, and differentiate between real polarized sources and instrumental leakage or diffuse foreground emission.

Our pipeline also incorporated a new error analysis, based on Monte Carlo simulation of noise with the same correlation properties as the true noise in the observations. While this method had some flaws that could not be resolved in the scope of this work, we were able to assess its effectiveness by using independent measurements of the same sources. We found that the resulting error estimates produced the expected statistical behaviour. Using the same multiple independent measurements, we have shown that the systematic uncertainty introduced by the ionospheric Faraday rotation correction is closer to 0.05 rad m^{-2}, which is smaller than previously predicted.

From these data we have produced a catalog of 102 low-frequency polarized radio sources, divided into 1 known pulsar and 101 unclassified sources (presumed to be background radio galaxies), covering a region of 570 square degrees.

We compared our measured Faraday depths against those observed at 1.4 GHz in the Taylor et al. [2009] catalog, finding 55 sources detected in both catalogs. There is a general correspondence between the measured Faraday depths in both catalogs, but with a large scatter that seems to be larger than can be explained by errors alone. This suggests that Faraday depth structure wider than 1 rad m^{-2} is likely present in many of these sources, which contributes to the observed polarization at 1.4 GHz but is depolarized at 150 MHz.

This is the first large catalog of polarized sources at such a low frequency; as such, there are many avenues of scientific investigation that can be explored with this data. We describe a few that build on the analysis in the previous section and give additional examples below.

We have compared our measured polarization fractions to those at 1.4 GHz, to investigate the wavelength dependent depolarization, which we interpret in terms of Faraday thin (non-depolarizing) and Faraday-thick (depolarizing) components. We found that most sources are strongly depolarized in our 150 MHz data compared to the 1.4 GHz data, but approximately 10% of sources are dominated by Faraday thin polarized emission. Further investigation into these objects, particularly their classification, will be useful in determining the origin of such Faraday thin emission.

We have found a source density of 1 source per 5.6 square degrees, which is lower than that found at higher frequencies [e.g. Brown et al., 2003], but have not calculated the (polarized) flux-dependent source counts. Such source counts are useful for studying the evolution of populations of radio sources; polarized source counts probe the evolution of magnetic fields. Comparing low-frequency source counts to higher-frequency source counts [e.g. Stil et al., 2014] could provide information on the evolution of depolarization in radio sources and in turn information on the evolution of the magnetic fields.

There may be unknown pulsars among our polarized sources. Pulsars are typically highly

polarized, with a steeply decreasing radio spectrum (making them brighter at low frequencies), and are guaranteed to be point sources at any reasonable resolution. Our catalog could be useful for identifying possible pulsar candidates, by cross-checking with other catalogs to obtain the spectral index and angular size of our sources. Pulsars may also have distinct properties in terms of the Faraday thin fraction, giving us an additional criteria on which to select candidates, but a larger sample is needed to check this possibility.

We have shown that the LOTSS data is well suited for searching for low-frequency polarized sources. The full survey will cover the entire sky above declination 0°; if we assume the polarized source density is the same as what we have found, we can expect to find approximately 3700 polarized sources in the full survey area. If our polarized pipeline can be improved, particularly by removing the instrumental leakage and by using the full resolution of the data, the source density should rise significantly. A more robust pipeline with the ability to classify sources with multiple peaks would also be very useful in studying the presence of Faraday complexity in these sources. We conclude that a full polarization processing of LOTSS would be very useful in advancing the study of magnetism in distant radio sources.

Acknowledgements
This work is part of the research programme 639.042.915, which is (partly) financed by the Netherlands Organisation for Scientific Research (NWO).

LOFAR, the Low Frequency Array designed and constructed by ASTRON, has facilities in several countries, that are owned by various parties (each with their own funding sources), and that are collectively operated by the International LOFAR Telescope (ILT) foundation under a joint scientific policy.

This research used ionospheric TEC maps produced by the Centre for Orbital Determination in Europe (CODE, http://aiuws.unibe.ch/ionosphere/).

This research made extensive use of Astropy, a community-developed core Python package for Astronomy [Astropy Collaboration et al., 2013]; SciPy [Jones et al., 2001–]; NumPy [van der Walt et al., 2011]; IPython [Pérez & Granger, 2007]; matplotlib [Hunter, 2007]; and the Common Astronomy Software Applications [CASA, McMullin et al., 2007].

4.A Catalogs

Table 4.1: Catalog of polarized point sources

ID	TGSS-ADR1 ID	RA (J2000) [h m s]	Dec (J2000) [° ′ ″]	Pol. Int. [mJy PSF^{-1}]	ϕ [rad m^{-2}]
1	J104221.7+530524	10 42 22.6 ± 0.9	+53 05 24.2 ± 09.4	3.63 ± 0.19	+12.92 ± 0.05
2	J104628.4+544944	10 46 30.1 ± 0.3	+54 49 38.1 ± 02.6	5.84 ± 0.13	+8.94 ± 0.03
3	J104641.0+543424	10 46 41.1 ± 0.2	+54 34 26.1 ± 01.6	24.66 ± 0.31	+8.29 ± 0.01
4	J105410.0+471441	10 54 12.0 ± 1.8	+47 14 53.9 ± 20.5	0.81 ± 0.12	+28.24 ± 0.14
5	J105500.7+520202	10 55 02.8 ± 0.6	+52 01 57.6 ± 06.0	8.81 ± 0.42	+17.82 ± 0.07
6	J105702.8+483652	10 57 02.9 ± 0.1	+48 36 42.7 ± 01.4	14.99 ± 0.14	+16.79 ± 0.01
7	J105706.7+532543	10 57 07.1 ± 0.3	+53 25 41.3 ± 01.9	37.82 ± 0.54	+12.69 ± 0.01
8	J110009.3+494022	11 00 10.5 ± 0.7	+49 40 36.8 ± 06.7	1.30 ± 0.06	+16.34 ± 0.06
9	J110137.7+515701	11 01 41.2 ± 0.8	+51 57 05.3 ± 06.5	1.63 ± 0.08	+12.45 ± 0.06
10	J110208.0+474328	11 02 10.3 ± 0.7	+47 43 32.2 ± 07.2	2.30 ± 0.10	+23.68 ± 0.04
11	J110249.5+531247	11 02 48.1 ± 1.2	+53 12 37.8 ± 08.9	6.15 ± 0.42	+18.33 ± 0.08
12	J110305.0+525940	11 03 04.7 ± 1.1	+52 59 29.0 ± 10.1	1.47 ± 0.13	+15.10 ± 0.14
13	J110614.9+533600	11 06 13.9 ± 1.0	+53 35 48.0 ± 07.6	7.95 ± 0.46	+4.37 ± 0.07
14	J110638.1+542951	11 06 40.7 ± 0.7	+54 30 02.1 ± 05.2	2.55 ± 0.09	+13.78 ± 0.03
15	J110941.6+531242	11 09 40.0 ± 0.7	+53 12 37.9 ± 06.4	2.29 ± 0.11	+11.66 ± 0.08
16	J111724.3+525155	11 17 25.6 ± 1.2	+52 52 01.7 ± 10.1	7.98 ± 0.66	+4.21 ± 0.11
17	J111811.8+531944	11 18 11.3 ± 0.9	+53 19 51.1 ± 09.5	12.41 ± 0.96	+4.12 ± 0.12
18	J112023.1+540427	11 20 23.9 ± 0.9	+54 04 30.0 ± 07.4	4.03 ± 0.26	+21.07 ± 0.08
19	J112026.4+571000	11 20 24.8 ± 0.4	+57 10 33.2 ± 02.9	14.17 ± 0.28	+13.07 ± 0.02
20	J112353.8+514148	11 23 53.9 ± 0.8	+51 41 42.2 ± 07.0	3.14 ± 0.14	+7.80 ± 0.04
21	J112542.0+564224	11 25 45.4 ± 1.1	+56 42 30.2 ± 06.4	3.12 ± 0.19	+13.83 ± 0.06
22	J112606.0+502217	11 26 04.7 ± 0.4	+50 21 57.5 ± 05.0	6.08 ± 0.19	+6.75 ± 0.04
23	J112947.8+502551	11 29 48.3 ± 1.4	+50 26 00.9 ± 16.7	4.81 ± 0.69	-5.91 ± 0.12
24	J113153.1+555244	11 31 55.4 ± 0.9	+55 52 48.4 ± 08.0	5.04 ± 0.32	+4.26 ± 0.10
25	J113756.1+471312	11 37 57.2 ± 3.5	+47 12 58.4 ± 36.6	1.20 ± 0.22	+21.82 ± 0.22
26	J113817.0+495023	11 38 15.7 ± 0.7	+49 50 34.1 ± 05.1	1.60 ± 0.07	+9.09 ± 0.06
27	J115231.6+463113	11 52 32.1 ± 1.4	+46 31 00.1 ± 20.3	1.32 ± 0.17	+16.36 ± 0.09
28	J115316.2+480358	11 53 15.9 ± 1.8	+48 03 56.8 ± 19.1	1.06 ± 0.15	+26.38 ± 0.16
29	J115405.8+562040	11 54 07.4 ± 1.1	+56 20 47.9 ± 06.6	13.87 ± 0.70	+2.86 ± 0.05
30	J115405.8+562040	11 54 09.9 ± 0.4	+56 21 08.5 ± 02.8	6.84 ± 0.14	-3.88 ± 0.02
31	J115420.7+452330	11 54 20.8 ± 0.1	+45 24 01.6 ± 01.1	83.99 ± 0.68	+8.37 ± 0.01
32	J115913.7+535307	11 59 14.0 ± 0.8	+53 53 10.6 ± 08.7	9.75 ± 0.59	+4.55 ± 0.06
33	J120607.9+521158	12 06 06.2 ± 1.3	+52 12 03.4 ± 10.5	2.76 ± 0.29	-13.43 ± 0.14
34	J120607.9+521158	12 06 06.5 ± 1.4	+52 12 17.9 ± 12.0	3.29 ± 0.30	+12.56 ± 0.10
35	J120714.1+540754	12 07 14.1 ± 1.0	+54 07 57.1 ± 06.7	8.13 ± 0.40	+4.68 ± 0.05
36	J121041.5+532907	12 10 40.5 ± 0.4	+53 29 02.7 ± 03.9	7.81 ± 0.20	+12.08 ± 0.02
37	J121043.5+483424	12 10 44.0 ± 0.6	+48 34 30.5 ± 05.7	2.49 ± 0.09	+11.99 ± 0.04
38	J121158.7+545602	12 11 59.0 ± 0.2	+54 56 10.6 ± 01.6	50.27 ± 0.55	+19.12 ± 0.01
39	J121415.5+454003	12 14 18.6 ± 0.6	+45 40 09.7 ± 04.7	6.14 ± 0.21	+4.95 ± 0.06
40	J121438.2+500646	12 14 40.4 ± 0.7	+50 06 55.2 ± 07.2	2.41 ± 0.14	+31.69 ± 0.08

ID	TGSS-ADR1 ID	RA (J2000) [h m s]	Dec (J2000) [° ′ ″]	Pol. Int. [mJy PSF^{-1}]	ϕ [rad m^{-2}]
41	J121622.7+524422	12 16 23.9 ± 0.8	+52 44 18.3 ± 07.3	4.41 ± 0.23	+21.58 ± 0.06
42	J121839.5+502549	12 18 38.9 ± 0.4	+50 25 40.5 ± 03.1	25.83 ± 0.54	+27.75 ± 0.02
43	J121849.8+534620	12 18 50.6 ± 0.4	+53 46 16.4 ± 04.4	4.10 ± 0.10	+13.49 ± 0.02
44	J121906.5+482956	12 19 06.0 ± 0.7	+48 29 59.6 ± 08.2	3.00 ± 0.17	+6.43 ± 0.08
45	J121916.1+552250	12 19 18.4 ± 0.5	+55 22 26.9 ± 03.6	5.17 ± 0.12	+19.72 ± 0.02
46	J121935.5+552828	12 19 33.6 ± 0.7	+55 28 20.9 ± 05.7	4.76 ± 0.21	+22.00 ± 0.06
47	J122106.2+454845	12 21 03.1 ± 1.4	+45 48 42.7 ± 10.2	2.32 ± 0.20	+7.39 ± 0.08
48	J122156.7+454738	12 21 55.2 ± 1.0	+45 47 46.7 ± 05.9	2.30 ± 0.15	+10.47 ± 0.08
49	J122607.8+473659	12 26 08.1 ± 0.8	+47 37 22.9 ± 09.2	3.74 ± 0.21	+9.23 ± 0.06
50	J123129.3+491539	12 31 28.2 ± 0.9	+49 15 35.9 ± 08.5	1.46 ± 0.09	+14.48 ± 0.06
51	J123234.7+482133	12 32 35.7 ± 0.5	+48 21 33.5 ± 04.2	4.05 ± 0.13	+6.72 ± 0.04
52	J123436.1+532225	12 34 34.5 ± 0.4	+53 22 44.2 ± 03.2	6.03 ± 0.16	+7.38 ± 0.03
53	J123506.6+562503	12 35 09.2 ± 0.7	+56 24 46.3 ± 07.3	2.77 ± 0.13	+12.49 ± 0.07
54	J123527.8+531457	12 35 25.6 ± 1.1	+53 15 11.5 ± 07.7	1.93 ± 0.13	+9.74 ± 0.08
55	J123723.7+505717	12 37 22.8 ± 0.5	+50 57 14.8 ± 04.2	3.63 ± 0.11	+13.85 ± 0.03
56	J124007.1+533429	12 40 05.0 ± 0.4	+53 34 27.6 ± 03.0	17.99 ± 0.41	+19.12 ± 0.03
57	J124022.0+465638	12 40 20.5 ± 0.3	+46 56 54.7 ± 03.2	9.68 ± 0.20	+8.59 ± 0.02
58	J124115.3+514126	12 41 12.8 ± 0.8	+51 41 23.4 ± 06.0	8.78 ± 0.37	+16.73 ± 0.05
59	J124331.0+521941	12 43 30.3 ± 0.9	+52 19 42.6 ± 07.0	3.68 ± 0.19	+13.70 ± 0.05
60	J130145.1+540844	13 01 43.2 ± 0.5	+54 08 37.8 ± 03.5	15.57 ± 0.39	+13.85 ± 0.02
61	J130414.2+554136	13 04 11.7 ± 4.8	+55 42 04.6 ± 40.3	3.11 ± 0.83	+19.40 ± 2.08
62	J130709.4+492140	13 07 10.6 ± 0.9	+49 21 41.7 ± 08.3	2.52 ± 0.13	+14.58 ± 0.07
63	J130748.6+471021	13 07 51.5 ± 0.3	+47 09 47.6 ± 03.5	7.78 ± 0.18	+7.61 ± 0.02
64	J130854.6+553047	13 08 56.7 ± 1.5	+55 30 58.0 ± 10.0	2.08 ± 0.19	+15.47 ± 0.09
65	J131634.4+493239	13 16 39.8 ± 1.2	+49 32 57.6 ± 09.8	1.21 ± 0.09	+12.69 ± 0.09
66	J132632.1+515413	13 26 32.4 ± 1.8	+51 54 16.2 ± 15.1	2.68 ± 0.27	+20.40 ± 0.11
67	J133437.2+563147	13 34 36.1 ± 0.3	+56 31 47.9 ± 02.1	17.10 ± 0.25	+11.32 ± 0.01
68	J133534.6+563114	13 35 34.0 ± 0.5	+56 31 09.8 ± 03.5	9.02 ± 0.26	+7.79 ± 0.04
69	J133922.6+464014	13 39 20.1 ± 0.5	+46 41 11.4 ± 04.7	12.68 ± 0.46	+20.56 ± 0.04
70	J134103.7+491532	13 41 04.5 ± 0.4	+49 15 26.4 ± 05.2	7.18 ± 0.18	+9.73 ± 0.02
71	J134545.3+533254	13 45 47.1 ± 0.9	+53 32 55.2 ± 06.8	8.65 ± 0.44	+15.16 ± 0.06
72	J134548.2+564931	13 45 48.1 ± 0.7	+56 49 30.5 ± 05.9	7.31 ± 0.30	+12.40 ± 0.05
73	J134835.2+515605	13 48 35.5 ± 0.9	+51 56 04.7 ± 05.7	2.27 ± 0.10	+15.82 ± 0.05
74	J135140.2+564437	13 51 39.8 ± 0.7	+56 44 33.8 ± 05.7	7.86 ± 0.29	+18.02 ± 0.04
75	J135849.3+475503	13 58 49.3 ± 0.7	+47 54 51.1 ± 06.6	4.73 ± 0.18	+18.99 ± 0.05
76	J140227.2+520431	14 02 27.7 ± 0.6	+52 04 49.4 ± 05.1	5.45 ± 0.18	+9.92 ± 0.04
77	J140539.5+541137	14 05 39.0 ± 0.5	+54 11 40.7 ± 04.1	8.06 ± 0.25	+14.82 ± 0.03
78	J141946.0+542314	14 19 46.7 ± 0.8	+54 23 08.6 ± 06.2	2.94 ± 0.14	+17.64 ± 0.06
79	J142118.5+530328	14 21 18.9 ± 1.0	+53 03 19.7 ± 10.3	3.22 ± 0.23	+18.87 ± 0.09

ID	TGSS-ADR1 ID	RA (J2000) [h m s]	Dec (J2000) [° ′ ″]	Pol. Int. [mJy PSF^{-1}]	ϕ [rad m^{-2}]
80	J142308.4+505640	14 23 09.4 ± 0.3	+50 56 42.9 ± 02.8	11.48 ± 0.22	+7.62 ± 0.02
81	J142314.0+505537	14 23 10.0 ± 0.3	+50 56 09.4 ± 05.2	15.83 ± 0.39	+7.73 ± 0.03
82	J143605.2+534920	14 36 03.7 ± 0.5	+53 48 53.2 ± 05.8	2.04 ± 0.07	+12.42 ± 0.04
83	J143642.3+560816	14 36 40.5 ± 1.1	+56 07 58.4 ± 09.7	1.61 ± 0.09	+15.45 ± 0.05
84	J143912.1+541829	14 39 14.4 ± 0.6	+54 18 21.9 ± 04.4	2.12 ± 0.06	+11.63 ± 0.03
85	J144248.0+535416	14 42 52.4 ± 0.7	+53 54 20.2 ± 04.9	3.57 ± 0.12	+8.26 ± 0.03
86	J144301.5+520136	14 43 01.3 ± 0.3	+52 01 37.9 ± 03.1	98.01 ± 2.24	+15.06 ± 0.02
87	J144542.5+474919	14 45 41.7 ± 0.8	+47 49 00.2 ± 08.6	5.97 ± 0.37	+16.42 ± 0.07
88	J145012.6+471046	14 50 11.9 ± 0.3	+47 10 46.5 ± 03.0	6.21 ± 0.13	+6.81 ± 0.02
89	J145046.1+530005	14 50 45.4 ± 0.5	+52 59 59.6 ± 05.1	7.53 ± 0.26	+16.92 ± 0.05
90	J145356.5+502731	14 53 56.1 ± 0.6	+50 27 26.5 ± 05.6	2.61 ± 0.10	+14.07 ± 0.04
91	J145426.6+514544	14 54 26.8 ± 0.7	+51 45 53.6 ± 06.5	3.58 ± 0.15	+17.81 ± 0.05
92	J145431.4+514537	14 54 27.5 ± 1.4	+51 45 46.2 ± 10.3	3.71 ± 0.34	+17.84 ± 0.11
93	J145427.4+512436	14 54 27.6 ± 1.0	+51 24 44.3 ± 09.6	2.40 ± 0.17	+20.08 ± 0.08
94	J145854.8+464917	14 58 57.5 ± 0.3	+46 49 20.2 ± 03.2	7.49 ± 0.16	-5.01 ± 0.02
95	J150013.4+501550	15 00 13.4 ± 0.8	+50 15 43.6 ± 06.7	2.46 ± 0.12	+13.08 ± 0.06
96	J150017.0+543605	15 00 19.0 ± 1.6	+54 36 03.9 ± 13.4	1.42 ± 0.15	+17.84 ± 0.11
97	J150048.7+475113	15 00 48.8 ± 0.5	+47 51 11.9 ± 05.0	6.42 ± 0.21	+6.18 ± 0.04
98	J150439.0+503005	15 04 42.9 ± 1.1	+50 30 03.0 ± 06.8	2.70 ± 0.15	+6.05 ± 0.08
99	J150609.8+513531	15 06 08.7 ± 0.5	+51 35 18.2 ± 04.4	3.30 ± 0.09	+9.41 ± 0.03
100	J150644.2+493355	15 06 43.7 ± 0.5	+49 33 51.9 ± 03.7	2.65 ± 0.07	+8.90 ± 0.03
101	J152405.3+542814	15 24 02.3 ± 3.3	+54 28 16.8 ± 26.3	19.37 ± 3.41	-5.62 ± 1.13

Table 4.2: Polarized pulsar.

Name	TGSS-ADR1 ID	RA (J2000) [h m s]	Dec (J2000) [° ′ ″]	Pol. Int. [mJy PSF^{-1}]	ϕ [rad m^{-2}]
B1112+50/J1115+5030	J111538.5+503024	11 15 37.5 ± 0.2	+50 30 09.7 ± 02.1	5.83 ± 0.07	+2.69 ± 0.01

Chapter 5

Diffuse polarized emission in the LOFAR Two-meter Sky Survey

C.L. Van Eck, M. Haverkorn, et al.

A&A, in preparation

Abstract

Faraday tomography offers a new method for analyzing diffuse polarized synchrotron emission from our Galaxy, and using it to interpret the magnetic field in the interstellar medium. We have applied Faraday tomography to 60 observations from the LOFAR Two-Meter Sky Survey (LOTSS) HETDEX test region. We have produced the first Faraday depth cube mosaic, covering 568 square degrees at high Galactic latitudes, at $4\farcm3$ image plane resolution and 1 rad m^{-2} Faraday depth resolution, with a typical sensitivity of 50–100 μJy PSF^{-1} RMSF^{-1}. While parts of the field are strongly contaminated by instrumental polarization, we observe diffuse polarized emission throughout most of the field, with typical brightness between 1 and 8 mJy PSF^{-1} RMSF^{-1}, and Faraday depths between -7 and $+25$ rad m^{-2}.

We observe many features in this emission, some up to 15 degrees in length. These include two regions with very uniformly structured, linear gradients in the Faraday depth; we measured the steepness of these gradients as 2.6 and 13 rad m^{-2} deg^{-1}. We find that the steeper gradient should be strongly depolarized, given previous beam depolarization models for such gradients; we propose a new beam depolarization model, based on the beam produced by uniform (u, v) coverage, that produces less depolarization for our observing parameters. We also observe a relationship between one of the gradients and an H I filament. Other ISM tracers were also checked for relationships with our polarization data, but very little signal was seen in most tracers. We conclude that the LOTSS data are very well suited for Faraday tomography, and that a full-scale survey with all the LOTSS data has the potential to reveal many new polarization features.

5.1 Introduction

Magnetic fields are present throughout interstellar space and play an important role in many aspects of the interstellar medium (ISM), such as cloud collapse in star formation [van Loo et al., 2012], energy transports and cascades in magnetohydrodynamic turbulence [Beresnyak & Lazarian, 2015], and pressure balance between different gas phases [Boulares & Cox, 1990].

Interstellar magnetic fields can be measured with radio polarization through two processes: synchrotron emission and Faraday rotation. Synchrotron emission is produced throughout interstellar space by cosmic ray electrons as they are deflected by interstellar magnetic fields, resulting in polarized radio emission. Faraday rotation occurs when polarized emission passes through magnetized plasma (which fills most of the volume of the ISM), which causes a frequency-dependent rotation of the polarization angle. The change in the polarization angle ($\Delta\tau$) is given by

$$\Delta\tau = \lambda^2\,\phi(d) = \lambda^2\,\left[0.812\ \mathrm{rad\,m^{-2}} \int_d^0 \left(\frac{n_\mathrm{e}}{\mathrm{cm^{-3}}}\right)\left(\frac{\vec{B}}{\mu\mathrm{G}}\right)\cdot\left(\frac{\vec{dl}}{\mathrm{pc}}\right)\right], \tag{5.1}$$

where $\phi(d)$ is the Faraday depth (sometimes called the Faraday rotation measure) which depends on the free electron density (n_e) and magnetic field ($\vec{B}$) integrated along the line of sight from the emission source at a distance d to the observer.

Polarized synchrotron emission occurs throughout the ISM, and then undergoes Faraday rotation as it propagates, and so when we observe along any line of sight we see the superposition of the emission at all distances and with correspondingly different Faraday depths. The rotation measure (RM) synthesis technique [Brentjens & de Bruyn, 2005] can be used to transform the observed wavelength-dependent polarization into the distribution of polarized emission as a function of Faraday depth. When applied to 3D image-frequency data this is called *Faraday tomography*, which produces Faraday depth cubes that map out the diffuse polarized emission as a function of position on the sky and Faraday depth. Such observations can be used to map magnetic fields in the ISM and study their properties [e.g. Van Eck et al., 2017; Lenc et al., 2016; Jelić et al., 2015].

The resolution in Faraday depth of Faraday tomography depends on the range of wavelength squared sampled by the observations, so low-frequency radio telescopes (which can produce very large wavelength squared coverage for the same fractional bandwidth) are capable of achieving much finer Faraday depth resolution than higher-frequency instruments. The newest generation of very low-frequency radio telescopes such as the Low Frequency Array [LOFAR, van Haarlem et al., 2013b] and the Murchison Widefield Array (MWA), which operate in the 100–200 MHz range, are capable of reaching Faraday depth resolutions around 1 rad m^{-2}, which is two orders of magnitude smaller than the resolution that can be achieved at 1.4 GHz or higher frequencies.

In recent years, there have been many studies using Faraday tomography to study diffuse polarization, each with different observations balancing tradeoffs between field-of-view, angular resolution, and Faraday depth resolution. Jelić et al. [2014], Jelić et al. [2015], and Van Eck et al. [2017] used LOFAR to observe single (approximately 20 square degree) fields with high Faraday depth resolution (≈1 rad m^{-2}) and modest angular resolution (a few arcminutes). Lenc et al. [2016] analyzed a large (625 square degree) field with high Faraday depth resolution (≈1 rad m^{-2}) and low angular resolution (54 arcminutes). Hill et al. [2017] used 1.3–1.8 GHz observations

from the Global Magneto-Ionic Medium Survey (GMIMS) to look at the Fan Region (which covers several hundred square degrees) with low Faraday depth resolution (150 rad m^{-2}) and low angular resolution (36 arcminutes). Iacobelli et al. [2013] used low-frequency observations from the Westerbork Synthesis Radio Telescope (WSRT) to look at a portion of the Fan Region (approximately 100 square degrees) at fairly high Faraday depth resolution (≈3 rad m^{-2}) and modest angular resolution (2 arcminutes). The observations with high angular resolution tend to have smaller fields of view, and vice versa, which makes it difficult to observe the full size of large polarization features (such as the filament in Jelić et al. [2015], which extends outside the field of view) while still minimizing the effects of beam depolarization (which limits the sensitivity of low-resolution observations).

In this paper we report on the polarization processing of 60 LOFAR observations from the LOFAR Two-meter Sky Survey (LOTSS) and present a Faraday depth mosaic covering an area of 570 square degrees. This is the first work to combine multiple LOFAR observations into a single Faraday depth cube, which allows us to take advantage of the high angular and Faraday depth resolution of LOFAR while still looking at large-scale features in the diffuse polarization. In Sec. 5.2 we present our data reduction and the production of Faraday depth cubes for each observation. In Sec. 5.3 we present a Faraday depth cube mosaic produced from these observations, and highlight the diffuse polarization features seen. In Sec. 5.4 we compare our mosaic against other tracers for components of the ISM, and in Sec. 5.5 we discuss possible causes for the diffuse polarization and its Faraday depth structure. In Sec. 5.6 we model the depolarization caused by Faraday rotation gradients and consider the implications for our observations and others. In Sec. 5.7 we summarize our results.

5.2 Data processing

We were given 63 calibrated observations from the LOFAR Two-meter Sky Survey; full details of the observational parameters and calibration methods can be found in Shimwell et al. [2017]. The polarization processed was done using the pipeline described in Van Eck et al. (in prep, Chapter 4); we summarize the key parameters and steps below.

The observations are from the LOTSS test region which covers the HETDEX field [Hill et al., 2008], a 420 square degree region near the Galactic north pole in the right ascension range 11 to 15 hours and declination range +45° to +55°. Each observation has a nominal duration of 8 hours and covers the frequency range 120–168 MHz with 488 channels. We received the observations after direction-independent amplitude and phase calibration with the LOTSS pipeline. Figure 5.1 shows the coverage of these observations in equatorial and Galactic coordinates.

Polarization calibration in the form of a correction for ionospheric Faraday rotation was performed prior to imaging. This was done using the RMextract package[1] written by Maaijke Mevius, combined with maps of the ionospheric total electron content from the Center for Orbital Determination in Europe (CODE)[2], to produce predictions for the ionospheric Faraday rotation. These predictions were used by the Black Board Selfcal software [BBS, Pandey et al., 2009] to

[1] https://github.com/maaijke/RMextract/
[2] http://aiuws.unibe.ch/ionosphere/

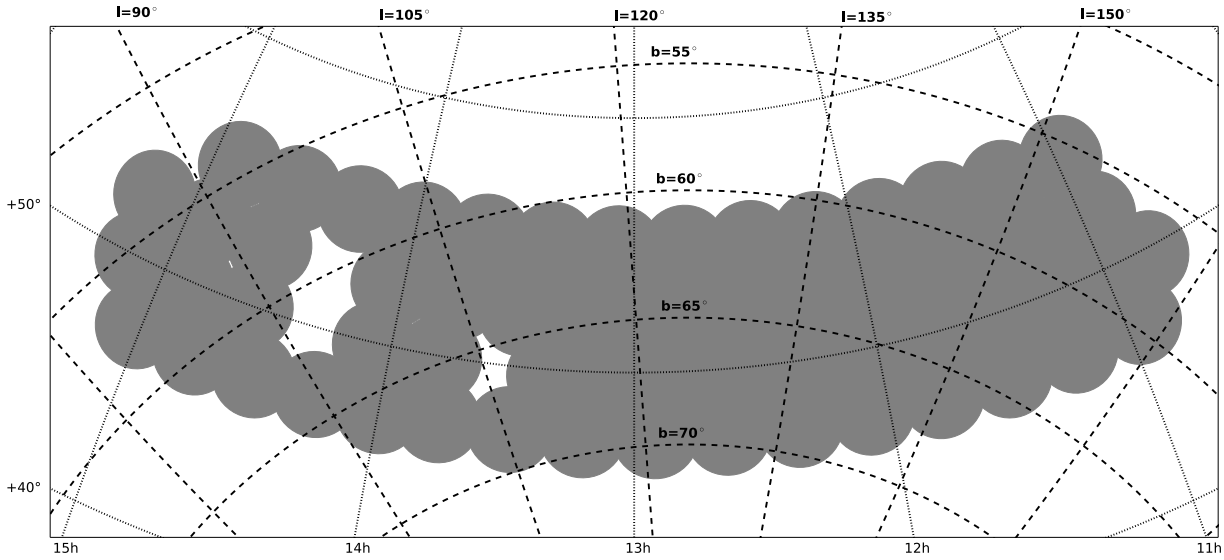

Figure 5.1: The locations of the LOTSS HETDEX observations, in both Equatorial (dotted lines) and Galactic (dashed lines) coordinates. Each grey circle covers the area inside the primary beam FWHM (3.4° diameter) for one observation, at the highest frequency (168 MHz). This image, and all that follow, are in an orthographic projection. The gaps are caused by the three fields that were removed for being very strongly affected by instrumental leakage.

derotate the polarization of the visibilities and thereby remove the ionospheric Faraday rotation. No correction for polarization leakage was performed, as no methods have yet been developed for performing leakage correction in LOFAR observations. The effects of polarization leakage on the results are discussed in Sec. 5.3.1.

Polarization imaging was performed independently for each channel using AWImager [Tasse et al., 2013b]. A baseline length upper limit of 800λ was applied, as this resulting in the synthesized beam (hereafter, point spread function or PSF) being more uniform across the band (V. Jelić, priv. comm.), giving a resolution of 4⁄3. The baselines between each pair of High-Band Antenna (HBA) substations (i.e.,CS*HBA0 and CS*HBA1) were removed, as these were known to often suffer from significant mutual interference. A robust weighting of 1.0 was used for imaging, and no CLEANing was performed, as the signal to noise ratio in individual channels was expected to be too low for CLEAN to be used successfully. By default AWimager produces images both with and without correction for the LOFAR primary beam; the images without correction were used for the quality control step described next, while the images with correction were used for producing Faraday depth cubes.

We found that a small fraction of the images were strongly affected by interference or calibration problems, which usually manifested as very strong patterns throughout the image. To identify these channels in an automated way, we calculated the standard deviation over all pixels in each of the images without primary beam correction (separately for Stokes Q and U). The channels affected by these problems stood out as having abnormally large standard deviations, but variations in the background noise across the band and between different observations made it difficult to assign a single threshold value for classifying images as bad. We chose to calculate,

for each channel, the median of the standard deviations of the images within 50 channels above or below in frequency; if the standard deviation (for either Q or U separately) in a channel was more than 1.5 times the median of these neighbouring channels then that channel was flagged as bad. Bad channels were removed before RM synthesis. During this process, three observations were found to have much higher noise levels than the others, which was found to be due to the presence of extremely bright radio sources; these observations were removed and not included in the following steps. After this step, the typical noise level in a single channel was 2–5 mJy PSF^{-1}.

RM synthesis was performed using pyrmsynth[3]. Channel weights were calculated using the inverse square of the standard deviation of each channel that was calculated in the previous step. If the standard deviation is dominated by the image noise, then this is equivalent to natural weighting in interferometry and should result in the lowest noise in the resulting Faraday depth cubes. For most observations, the weights were fairly uniform across the band, so this was not expected to produce any significant changes from uniform weighting. From the frequency coverage and weighting used, the resulting rotation measure spread function (RMSF) had a typical FWHM of 1.2 rad m^{-2}. From equation 61 of Brentjens & de Bruyn [2005], the theoretical FWHM (for uniform weighting) is 1.15 rad m^{-2}, so these values are consistent and show that the natural weighting has not significantly affected the Faraday depth resolution, as expected. From equations 62 and 63 of Brentjens & de Bruyn [2005], our observations are not sensitive to structures in Faraday depth wider than about 1.0 rad m^{-2}, and we have limited sensitivity to Faraday depths beyond 170 rad m^{-2}. As is typical for LOFAR observations, we are unable to resolve any features with Faraday thickness greater than the resolution, therefore we are only able to pick up unresolved features [or sharp edges of Faraday thick features, as described in Van Eck et al., 2017]. No spectral index correction was included in the RM synthesis step. Each RM cube covered Faraday depths from -100 to + 100 rad m^{-2} in steps of 0.5 rad m^{-2}. The RM-CLEAN algorithm [Heald et al., 2009] was applied to each Faraday depth cube, to a depth of 2 mJy PSF^{-1} RMSF^{-1}.

In order to combine the Faraday depth cubes from the different observations together, it was useful to estimate the position dependent noise in the cubes. We did this on a per-pixel basis by taking the distribution of polarized intensity values taken from the regions of the spectrum that were expected to be dominated by noise ($|\phi| > 20$ rad m^{-2}) and fitting a Rayleigh distribution (which is the expected distribution for polarized intensity in the absence of signal). The resulting Rayleigh σ parameter (which is equivalent to the Gaussian σ of the underlying Stokes Q and U distributions) was taken to be the noise in that pixel.

To combine the separate Faraday depth cubes together, we regridded them into a common pixel scheme. They were then averaged together using inverse-noise-squared weighting to produce a final mosaic covering the entire HETDEX region. Alternative weighting schemes, where each pixel used only the observation with the lowest noise or the observation with the nearest pointing center, were also tried but were found to produce significant artifacts in the overlap regions of adjacent pointings. However, these were useful for confirming the quality of the data and the suitability for mosaicing; we observed that many features in the cubes, such as depolarization canals, could be traced continuously across the boundaries between different observations.

[3]https://github.com/mrbell/pyrmsynth

5.3 HETDEX mosaic

The combined Faraday depth cube resulting from the processing described previously covers a total area of sky of 568 square degrees, with a typical noise level between 50–100 μJy PSF^{-1} RMSF^{-1}, with higher noise at the edges and near very bright Stokes I sources. Figures 5.2 through 5.7 show selected slices from the cube. These images give the polarized intensity in mJy PSF^{-1} RMSF^{-1}; the conversion to brightness temperature units is 0.8 K (mJy PSF^{-1})$^{-1}$. Figures 5.8 and 5.9 show a collapsed version of the cube where, per pixel, the highest polarized intensity was located and the polarized intensity and Faraday depth of the peak were used to determine the brightness and color, respectively. In the cube we see many diffuse polarized emission features, polarized point sources, and instrumental polarization leakage, which are discussed in detail below.

5.3.1 Instrumental polarization leakage

The instrumental polarization leakage for LOFAR, which causes emission from Stokes I to incorrectly appear in the other Stokes parameters, has the convenient property of being effectively independent of frequency. The result of this is that after RM synthesis, the leakage should appear only at Faraday depth 0 rad m^{-2}, which would allow astrophysical emission at other Faraday depths to be identified. However, the ionospheric Faraday rotation correction applies a frequency-dependent polarization angle rotation to the data, which shifts the leakage to the opposite Faraday depth as the correction (e.g. if the ionospheric Faraday rotation is +2 rad m^{-2}, the leakage will appear at −2 rad m^{-2} after the correction). Since the ionospheric correction varies with time, this also has the result of causing partial depolarization of the leakage, as the post-correction instrumental leakage will have different polarization angles at different times.

The net effect of the instrumental polarization leakage is to cause all Stokes I sources to appear in the Faraday depth cubes between −2 and 0 rad m^{-2} (as the ionospheric correction was typically between 0 and 2 rad m^{-2}). Since the different observations had different ionospheric conditions, the leakage sources appear at slightly different Faraday depths at different locations in the mosaic, and some regions also appear to have stronger or weaker leakage depending on how much depolarization the time-variability caused.

This describes the on-source polarization leakage, but in addition to this there is off-source polarization leakage, which is the dominant cause of the strong artifacts appearing widely distributed in Faraday depth around very bright sources such as 3C295 ($\alpha = 14^{\rm h}11^{\rm m}20^{\rm s}$, $\delta = +52°12'10''$, 74 Jy in Stokes I). The spurious polarization caused by the polarization leakage does not appear just at the location of the source, but is convolved with the synthesized beam/point spread function (PSF), just as the Stokes I and real polarized emission is. Since the locations and intensities of the sidelobes of the PSF vary with frequency, pixels near sources can pass in and out of sidelobes as a function of frequency. The result is a very complicated frequency-dependent spurious polarization signal that, when RM synthesis is applied, results in structure broadly distributed in Faraday depth. The net result of this is that while the on-source polarization leakage is usually confined to a single Faraday depth (determined by the ionosphere), the off-source leakage is present at most Faraday depths and covers larger areas around brighter sources.

In the HETDEX region mosaic, the off-source leakage of the two brightest sources occupies

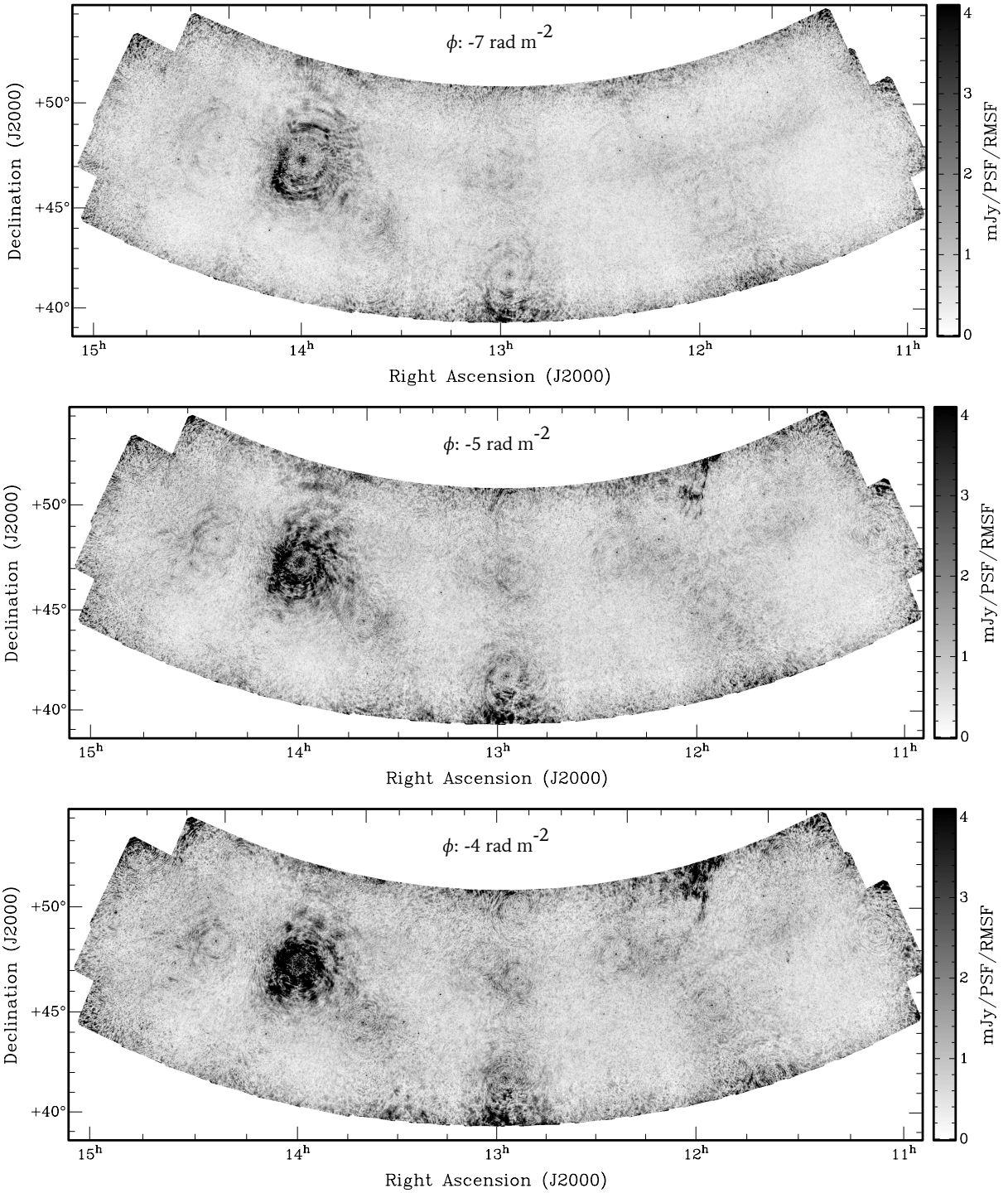

FIGURE 5.2: Selected slices from the Faraday depth cube mosaic, between -7 and -4 rad m^{-2}. The top panel shows a typical quiescent slice, with strong artifacts around 3C295. The lower two panels show diffuse polarized emission appearing in the top right.

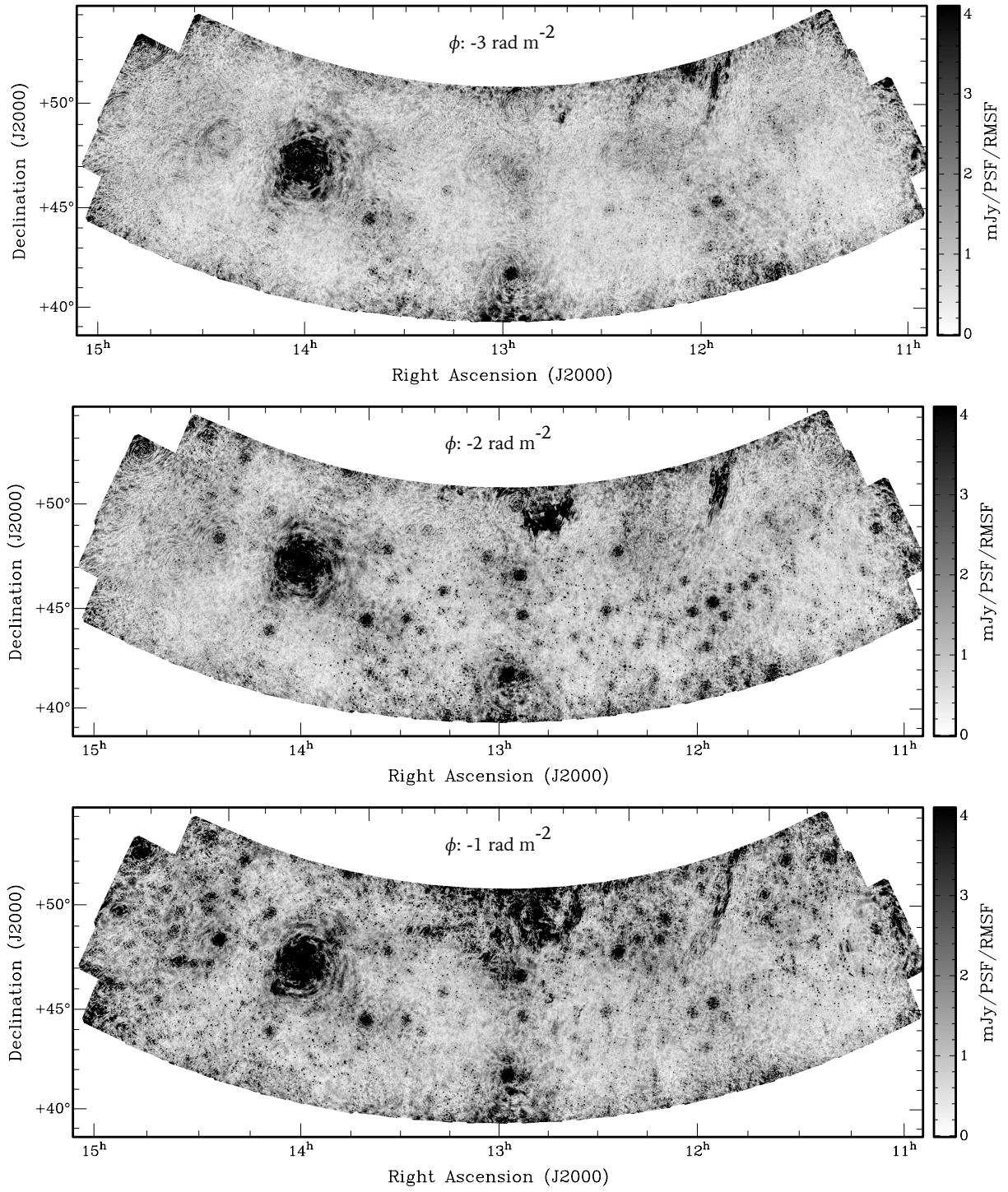

Figure 5.3: Selected slices from the Faraday depth cube mosaic, between -3 and -1 rad m^{-2}. The feature in the top right travels south-westward, and another feature appears in the top center and spreads outwards. The instrumental leakage from bright Stokes I sources also begins to appear strongly at -2 and -1 rad m^{-2}.

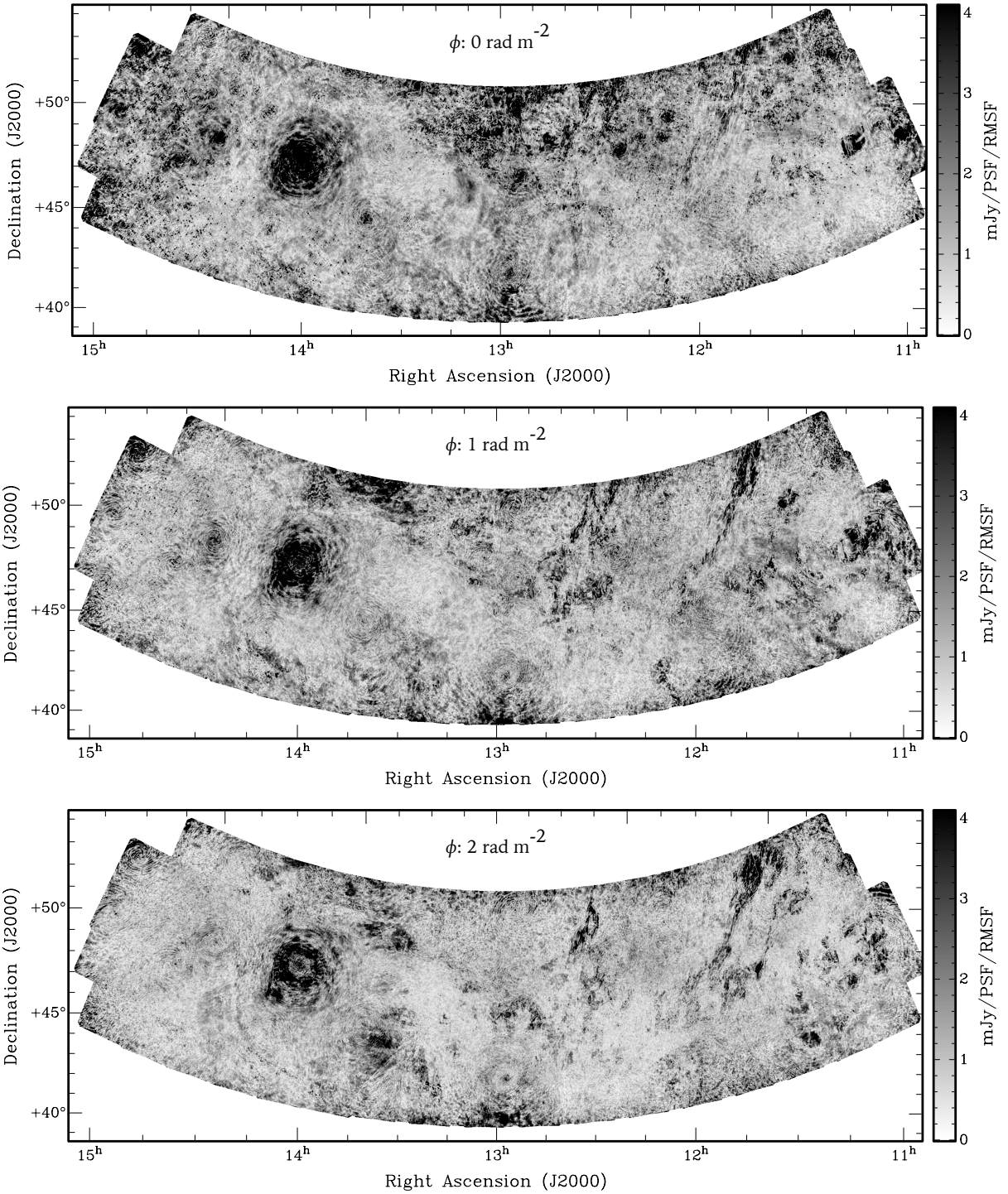

FIGURE 5.4: Selected slices from the Faraday depth cube mosaic, between 0 and 2 rad m^{-2}. The top-right feature continues to travel south-westward, becoming very filamentary-looking, while the top-center feature continues to expand outwards. Two more diffuse features appear in the lower right corner and lower left-of-center.

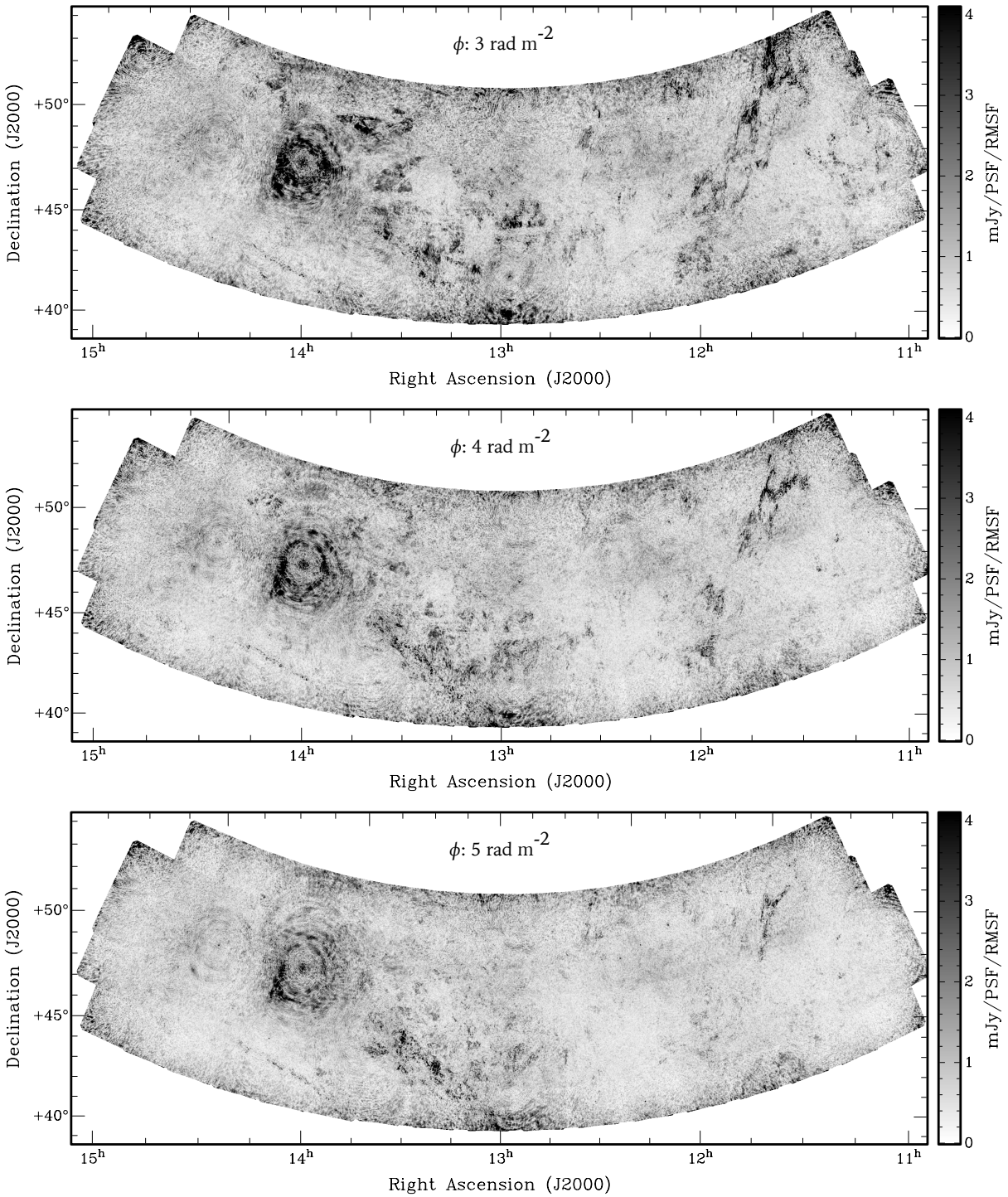

Figure 5.5: Selected slices from the Faraday depth cube mosaic, between 3 and 5 rad m^{-2}. The top right feature now appears as a very long filamentary structure spanning the height of the image, before fading away. The lower right feature also fades away at higher Faraday depths. The top center and lower left-of-center features now appear as a series of patches running south-westward just left of center. A faint, very straight filamentary feature appears in the bottom mid-left, slowly travelling upwards.

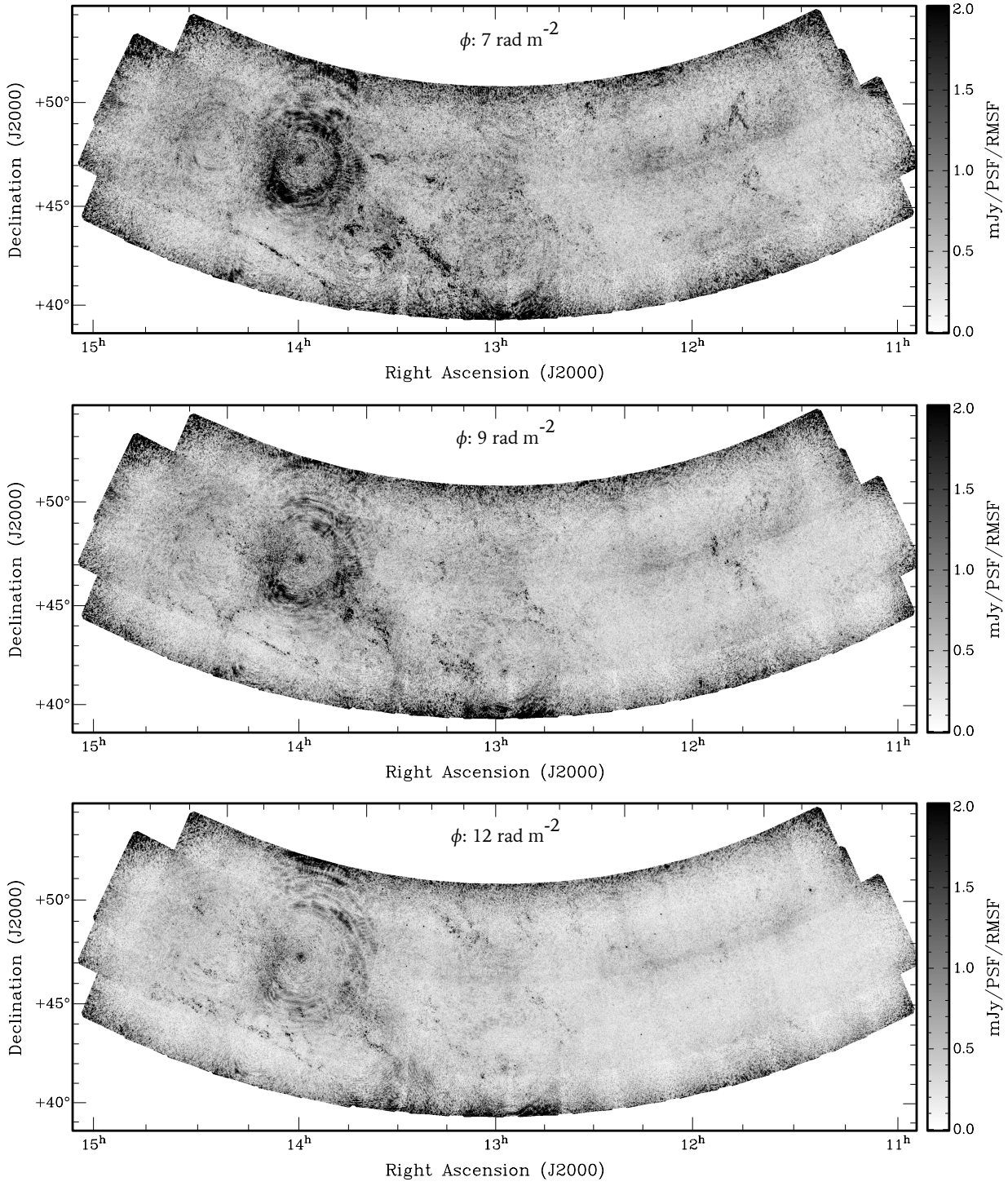

FIGURE 5.6: Selected slices from the Faraday depth cube mosaic, between 7 and 12 rad m^{-2}. Note that the intensity scale has been adjusted as the emission at these depths is much fainter. The top right and left-of-center features continue to fade out, while the faint very straight filament continues to travel upwards with new, thin features appearing above it.

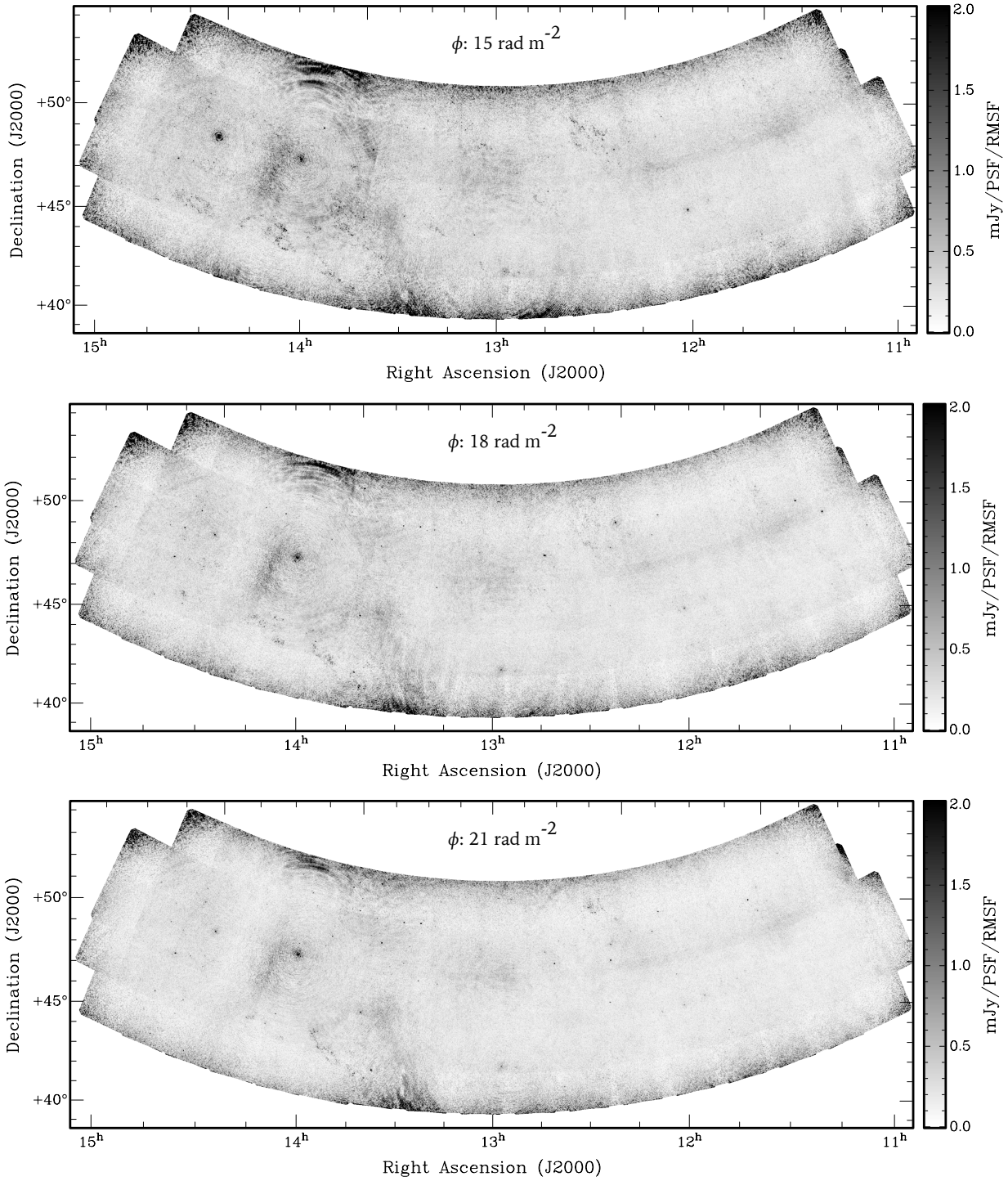

Figure 5.7: Selected slices from the Faraday depth cube mosaic, between 15 and 21 rad m^{-2}. The faint, straight filamentary features slowly converge and disappear. In the top panel, a very bright polarized source appears to the left of 3C295. Some emission appears to be present at the bottom of the image, just left of center, but it's not clear if this is real or caused by enhanced noise at the edge of the mosaic.

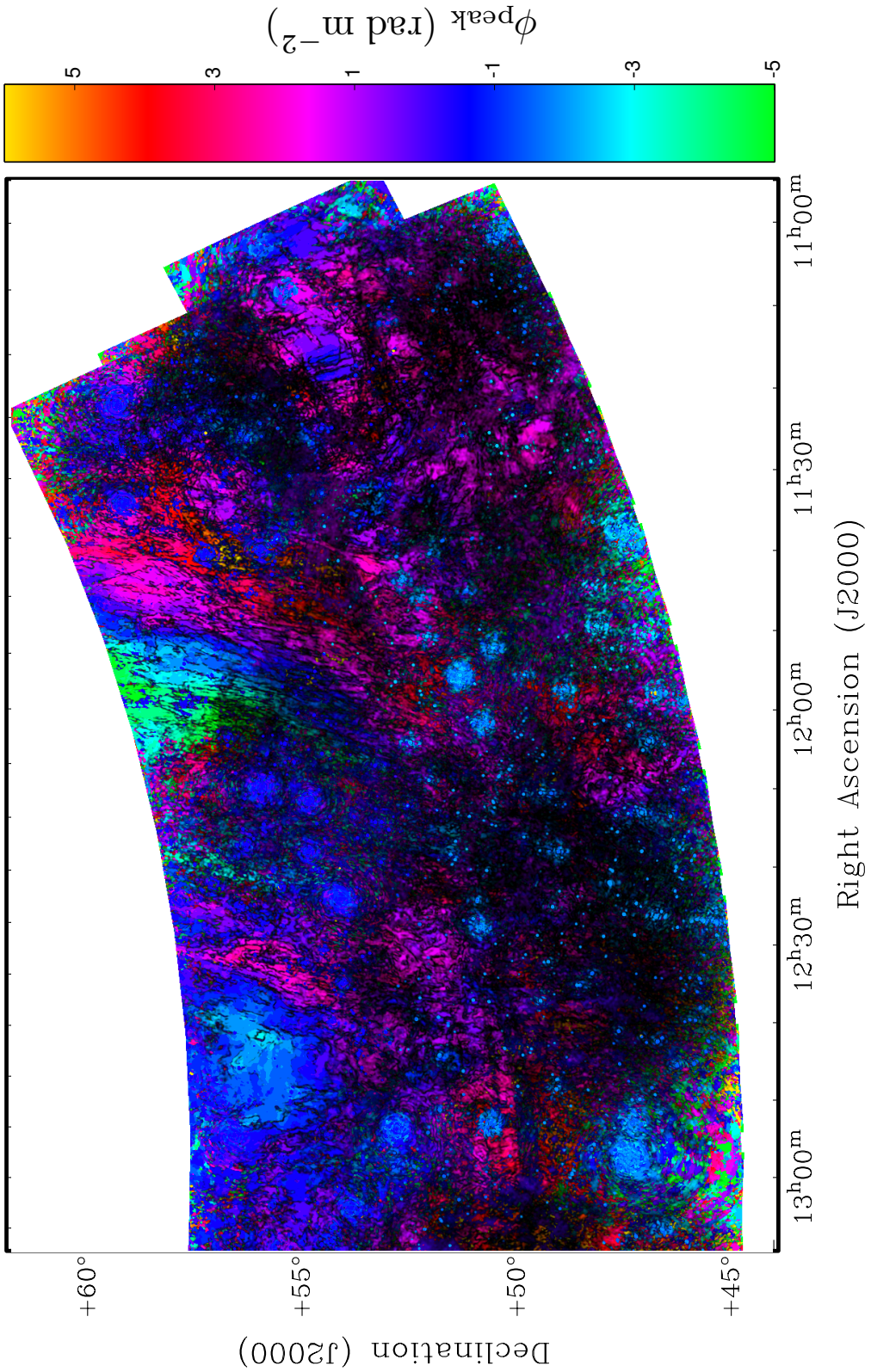

FIGURE 5.8: Collapsed view of the west half of the mosaic, where the polarized intensity and Faraday depth of the brightest emission per pixel were used to determine the brightness and color respectively. The features in the north west and north center can be clearly seen as sheets of polarized emission with Faraday rotation gradients, while the feature in the southwest shows much more patchy structure in polarized intensity. The instrumental leakage causes point sources to appear between -2 and 0 rad m^{-2}.

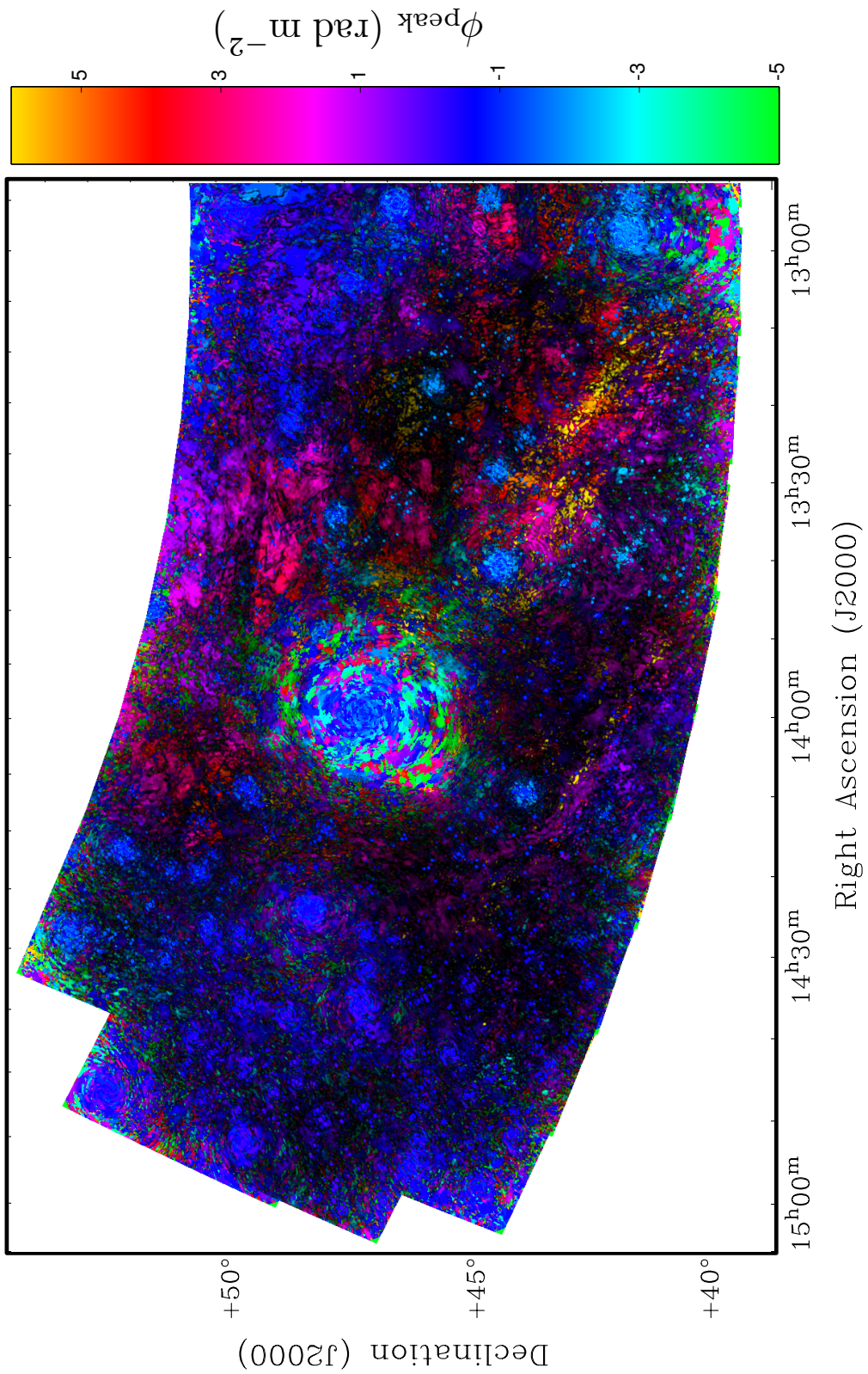

Figure 5.9: As Fig. 5.8, but for the east half of the mosaic. The instrumental leakage from 3C295 dominates this region, but diffuse features can still be seen: a gradient in Faraday depth is visible along the northern edge of the region, and the emission along the center region has a much more patchy appearance. The very faint linear 'filament' in the southeast is difficult to see because of its much lower polarized intensity.

a large portion of the field: 3C295 (74 Jy) is in the mid-left part of the mosaic, and 3C280 ($\alpha = 12^{\rm h}56^{\rm m}59^{\rm s}$ $\delta = +47°18'48''$, 25 Jy) is in the bottom center of the mosaic. The region around 3C295 is unusable for polarization analysis as a result, as the leakage is much brighter than the diffuse emission found in other parts of the field.

5.3.2 Point sources

In addition to diffuse Galactic polarized emission, polarized emission is also observed from some of the unresolved point sources. The identification, measurement, and analysis of these sources is done in a parallel paper (Chapter 4), and will not be discussed here. The majority of sources are found at Faraday depths between +10 and +25 rad m^{-2}, higher than most of the diffuse emission.

5.3.3 Diffuse emission

Diffuse polarized emission is seen through much of the mosaic, with polarized intensity levels ranging from 6–8 mJy PSF^{-1} RMSF^{-1} for the brighter features to 1 mJy PSF^{-1} RMSF^{-1} for the faintest identified features. The presence of polarization leakage has made quantitative analysis of the diffuse emission difficult, as it is not clear how to separate the diffuse emission from the off-source leakage. We have divided the diffuse emission into three regions, based on their morphologies and positions, and discuss each in turn below.

5.3.3.1 Bright northwest gradient and southwest patchy emission

This region occupies the field west of $12^{\rm h}$ right ascension, and is dominated by two bright features that appear connected. The most striking feature in Fig. 5.8, due to its brightness and range of colors, is a gradient in Faraday depth that occurs in the northwest (upper right) part of the field, from approximately $11^{\rm h}00^{\rm m}$ to $12^{\rm h}00^{\rm m}$ in right ascension and +53° to +57°30′ in declination. This emission feature appears at Faraday depths as low as −7 rad m^{-2} and can be traced as a single continuous sheet in the cube up to +7 rad m^{-2}, with typical brightness of 6–8 mJy PSF^{-1}RMSF^{-1}. Between −4 rad m^{-2} and +3 rad m^{-2}, this feature has the appearance of a 'travelling filament', caused by a very linear gradient in Faraday depth. We measured locations along the 'filament' at −3.5 rad m^{-2} and at +3 rad m^{-2}, and found that the separation between corresponding points was approximately 2.5°, resulting in a Faraday depth gradient of 2.6 rad m^{-2} deg^{-1}.

At Faraday depths around −1 rad m^{-2}, additional emission emerges from many locations in the west-most third of the field and expands with increasing Faraday depth. While this emission looks patchy and disconnected in individual slices (particularly at 0, +1, and +5 rad m^{-2}) and in Fig. 5.8, careful inspection of the full cube shows that the emission is a continuous sheet 'wrinkled' in Faraday depth, with many local minima and maxima in Faraday depth surrounded by a complex web of emission at intermediate Faraday depths. This is best seen at +3 rad m^{-2}, where many 'shells' of emission can be seen (surrounding the locations of local Faraday depth maxima/minima); this slice also best shows the extent of the emission, which extends the full height of the field.

Near the region occupied by the linear gradient, a second emission feature is also present at higher Faraday depths. It can be seen at +3 rad m^{-2} at the same location occupied by the first

feature at -5 rad m^{-2}. It is seen over a much smaller area than the first feature, but this may be due to the much lower brightness of this feature, 1–2 mJy PSF^{-1} $RMSF^{-1}$. It can be seen at Faraday depths up to +14 rad m^{-2}, and while it has some morphological similarities to the first feature (gradients and local maxima at similar locations), it also has some significant differences (a notable absence of emission in certain regions that are bright in the first feature).

5.3.3.2 Central sheet

The region between 12^h and 14^h right ascension is also dominated by a bright feature that appears to be a continuous sheet of emission distributed in Faraday depth between -3.5 and +14 rad m^{-2}, with several local maxima and minima at various locations and filamentary-looking emission, with a typical brightness of 3–4 mJy PSF^{-1} $RMSF^{-1}$. The brightest region occurs at the northern edge of the field, where emission appears at -3.5 rad $m^{-2}$and spread outwards in all directions with increasing Faraday depth, with a typical brightness of 6–8 mJy PSF^{-1} $RMSF^{-1}$.

There is also an emission feature present between -0.5 and +0.5 rad m^{-2} in much of this region, mostly clearly seen at 0 rad m^{-2} at 13^h10^m, 52° but covering much of the area from 13^h30^m, 50° to 12h30^m, 53°, which appears quite different from the previous features in that it is present only in a very narrow range of Faraday depths and it also appears to lack the depolarization canals that are prominent in all the other diffuse features. The absence of depolarization canals makes this feature look much less well defined and more difficult to identify by eye. The typical brightness of this feature is 2–4 mJy PSF^{-1} $RMSF^{-1}$. The large characteristic angular scale and low Faraday depth of this feature may indicate that it is a very local emission feature, possibly produced within the Local Bubble.

5.3.3.3 Southeast 'filament'

The third region is between 14^h and 15^h right ascension, and between +45° and +50° declination, and contains another continuous feature with a very linear Faraday depth gradient. The feature appears as a very long thin filament in Faraday depth slices from +1 rad m^{-2} to +11 rad m^{-2}, which in some slices can be seen to extend over 12° in length. As with the other features, when all Faraday depths are considered this can be seen as a continuous sheet of polarized emission. Around +9 rad m^{-2}, additional emission can be seen further north, and as Faraday depth increases these merge into the filaments towards several local maxima at Faraday depths between +19 and +25 rad m^{-2}. The typical brightness of this feature is 1–2 mJy PSF^{-1} $RMSF^{-1}$. The change in position of the filament was measured between +3 rad m^{-2} and +11 rad m^{-2}, and was found to be 0.6°, indicating a Faraday depth gradient of 13 rad m^{-2} deg^{-1}.

5.4 Comparison with other tracers

Previously published studies of Faraday depth cubes have looked at relating the observed diffuse polarization to tracers of other ISM components. Zaroubi et al. [2015] related Faraday depth structure observed in one LOFAR field to high frequency polarization maps, which trace dust emission, from the *Planck* mission, and found that the observed filaments in Faraday depth followed the magnetic field orientation inferred from the *Planck* polarization. Van Eck et al. [2017]

suggested that neutral clouds could act as sources of Faraday-thin polarized emission (which would not be strongly depolarized at low frequencies), and associated two observed polarization features with neutral clouds in the local ISM.

We investigated several ISM tracers for features similar to those we see in our Faraday depth cube. For each tracer, we regridded the data onto the same projection as our field, for ease of comparison. These tracers and their sources are:

- Hα, from Finkbeiner [2003], which used data from the Wisconsin Hα Mapper (WHAM) with a resolution of 1°.
- 408 MHz radio continuum, from Remazeilles et al. [2015], with a resolution of 56′.
- *Planck* thermal dust emission, with a resolution of 60′ (all *Planck* maps from Planck Collaboration et al. [2016]).
- *Planck* thermal dust polarization, with a resolution of 10′.
- *Planck* synchrotron, with a resolution of 60′.
- *Planck* synchrotron polarization, with a resolution of 40′.
- *Planck* CO(1-0), with a resolution of 60′.
- *Planck* free-free emission, with a resolution of 60′.
- integrated H I line emission from the Effelsberg-Bonn HI survey [EBHIS, Winkel et al., 2016], with a resolution of 11′.
- dust extinction, calculated from Green et al. [2015] as described below.

The maps of each of these tracers are shown in Figures 5.10 and 5.11. The *Planck* polarization maps were converted from Stokes Q and U into polarized intensity. The extinction maps were made by using the MWDUST package [Bovy et al., 2016] to get the optical extinction as a function of distance, taking the numerical derivative with respect to distance (which should serve as a proxy for dust density), and then integrating over selected distance ranges. The distance ranges were chosen to be 0–75 pc, 75–250 pc, and 250–1000 pc. The boundary at 75 pc was chosen as the Green et al. [2015] extinction model behaves differently for distances less than this, the boundary at 1000 pc was chosen as no significant extinction contribution was seen beyond this distance, and the boundary at 250 pc was chosen as the extinction behaviour appeared slightly different on both sides of this boundary. The extinction maps were observed to have a large scatter between adjacent pixels, so they were smoothed using a Gaussian kernel with a FWHM of 42′ (σ=18′) to produce the maps shown in Fig. 5.11.

The synchrotron intensity and polarization, radio continuum, Hα, free-free emission, and CO emission maps all show very little structure, so no comparisons with the low-frequency radio polarization were possible. The H I column density, thermal dust, dust polarization, and extinction between 75–250 pc all show similar structure, and the location of this structure does not appear to strongly correlate with the position of the polarized emission.

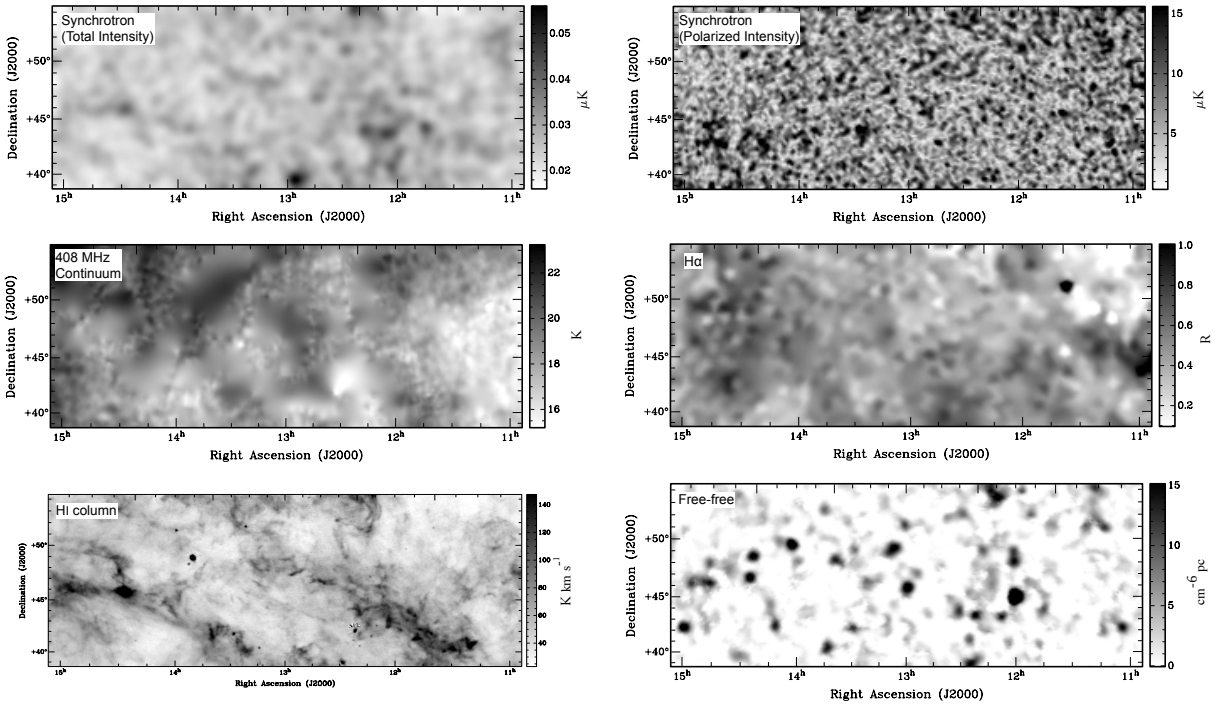

Figure 5.10: Selected ISM tracers, in the same coordinates and projection as the previous images. Only the H I shows any significant structure, and it does not correlate with anything seen in our Faraday depth cubes.

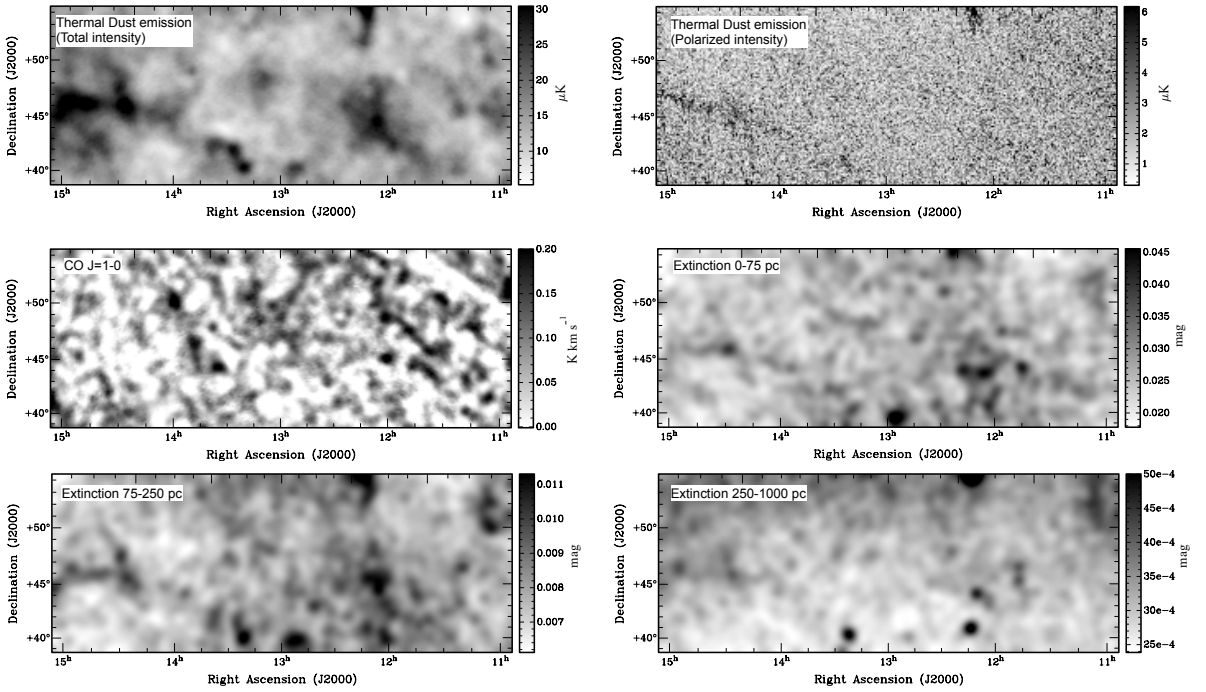

Figure 5.11: Continuation of figure 5.10, with additional tracers.

However, there is a very interesting relationship between the southeast gradient feature and the H I filament in the southeast part of our field. Figure 5.12 shows this region of the field, comparing a collapsed color figure (as Fig. 5.8, but with the color and intensity optimized to emphasize gradient and surrounding features) with contours made by integrating the H I data over the velocity range of the filament (-46 to -40 km s^{-1}). The H I filament has a sharp boundary with minimal emission (at any velocity) south of the lowest contour. The linear gradient in Faraday depth occurs south of the H I filament, and at the location of the filament the Faraday depth structure is more complex, with several local maxima, and the polarized intensity is more patchy. This transition from linear gradient to more complicated structure is very closely aligned with the boundary of the filament, including the slight bend around $\alpha = 14^{\rm h}30^{\rm m}$, $\delta = +47°20'$, which is strong evidence that this is not coincidental positioning. We discuss interpretations of this relationship in Sec. 5.5.3.

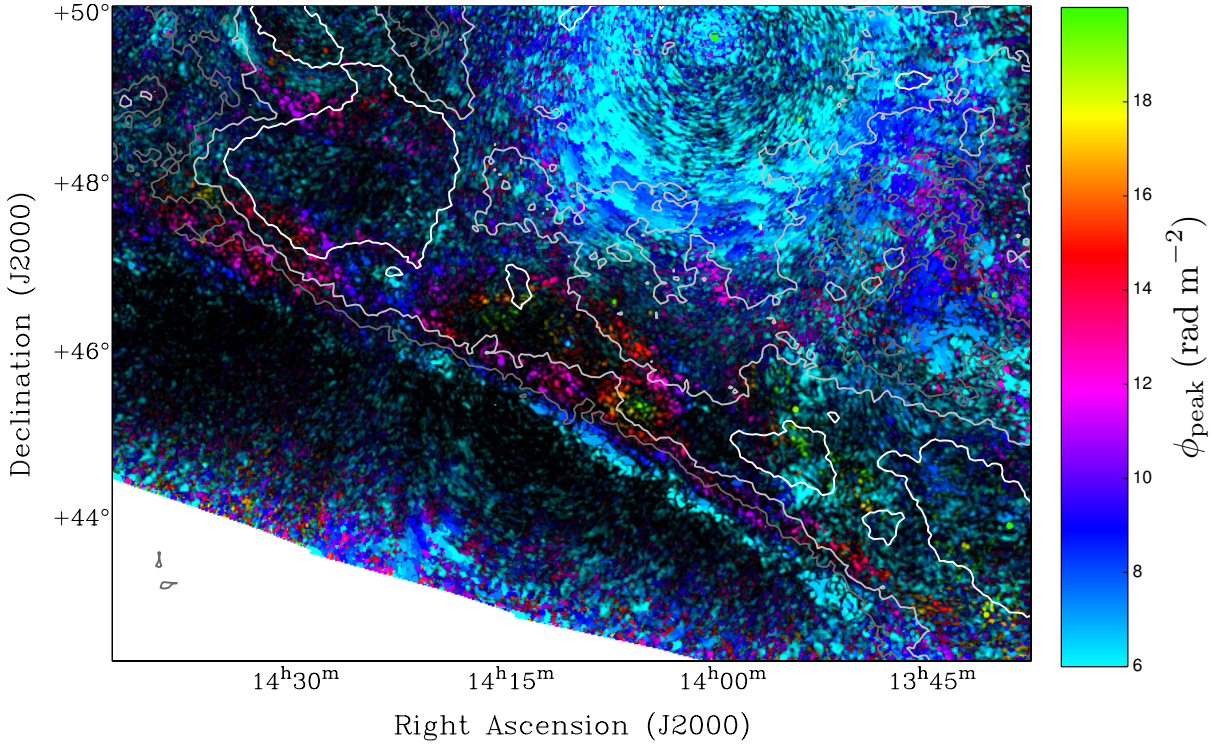

Figure 5.12: A comparison of the Faraday depth cube (background) with H I emission (contours). The background was made in the same way as Fig. 5.8, with the color and intensity scales optimized to emphasize the gradient feature and the emission northward of it. The contours are the H I intensity integrated over the velocity range of the filament, -46 to -40 km s^{-1}; the levels are 3, 5, and 8 K km s^{-1} for the dark grey, light grey, and white contours respectively. The smooth gradient in the Faraday depth is located below the H I filament, while inside the filament the Faraday depth behaviour is more complex.

We note that while the southeast gradient shows this clear alignment with an H I filament, this is not the case for the northwest gradient, which does also occur in a region of low H I emission

but has no H I features in the area where the gradient transitions to a more complex morphology.

In retrospect, it may not be surprising that many of the ISM tracers show very little signal or structure. The HETDEX field was originally selected for high-redshift cosmology observations in the optical, and it is likely that one of the requirements when selecting the location was minimal contamination from Galactic foregrounds. In this respect, the choice of initial region for LOTSS is somewhat unfortunate for Galactic foreground science, but it also suggests that future investigations using observations in other regions, particularly at lower Galactic latitudes, will probably have more visible ISM structure against which to compare the Faraday tomography observations.

5.5 Interpretation of diffuse emission

The lack of correlations between the polarized emission and the ISM tracers provides constraints on the source of the polarized emission. Below we consider separately the source of the polarized emission, and the Faraday rotation of that emission.

5.5.1 Emission source

Due to the frequency coverage of our observations, we are insensitive to polarized features with Faraday thickness greater than 1.0 rad m^{-2}. This places strong constraints on the ISM structures that we can observe; Van Eck et al. [2017] discussed what ISM conditions could cause Faraday-thin features. Here we consider which of those conditions are possible in the HETDEX field.

A localized enhancement in the perpendicular magnetic field, such as in a shock, could produce a Faraday-thin feature, but would also produce a synchrotron enhancement which should be seen in total intensity. An enhancement in the degree of order in the magnetic field could also produce such a feature, and could also be caused by a shock. There are also no obvious sources of shocks, such as supernova remnants, in this field, so both of these possibilities seem unlikely.

Strong localized enhancements or diminishments in the thermal electron density could also produce Faraday thin features. Enhancements would be associated with objects like shocks or H II regions, neither of which are observed in this field. Typical causes of low thermal electron density would be neutral clouds (associated with the warm neutral or cold neutral ISM phases) or regions of the hot ionized ISM phase. The tracers of neutral material (H I, thermal dust, extinction) don't show any correlation to the observed polarized emission, and the local ISM models of Lallement et al. [2014] don't show any clouds within the nearest few 100 pc in this direction. The Local Bubble is a volume of hot ionized medium (HIM) surrounding the Sun, and may (depending on the path length in this direction) produce a Faraday thin feature. However, this feature would not have any foreground to produce Faraday rotation, so the feature would appear at 0 rad m^{-2}. The Local Bubble could possibly be the source of the feature seen between ± 0.5 rad m^{-2} in the center part of the HETDEX field, but it could not be the source of the emission features seen. More distant regions of HIM could be the source of that emission, provided they are not so large as to become Faraday thick.

The final possibility is a region where the parallel component of the magnetic field is very small. If this occurs as a result of a reversal in the sign of the parallel magnetic field, this is called

a Faraday caustic [Bell et al., 2011], but lines of sight where the parallel component is very small in some volume but has the same sign in front and behind this volume are also possible. Such regions are possible in any phase of the ISM. Bell et al. [2011] showed that Faraday caustics can form sheets of Faraday-thin emission, covering the area of sky with the sign-reversal.

We propose that the most likely explanation for the sheets of Faraday-thin polarized emission we observe is Faraday caustics. All other explanations would produce signatures in one or more ISM tracer, and none of the tracers we have investigated show any correlation with the emission features we observe. Faraday caustics depend only on the magnetic field configuration, which presents the problem that, in the absence of any other constraints of the magnetic field configuration, any polarized feature can be explained by caustic. While Bell et al. [2011] show that Faraday caustics should have a distinctive one-sided tail in the parallel magnetic field, they also state that to resolve this structure requires that the ratio between the highest and lowest frequencies must be at least 1.5 (their equation 19), which is not satisfied for our observations. As a result, we cannot identify this characteristic feature of Faraday caustics. Since none of the other possible causes of Faraday thin emission are consistent with the ISM tracers for this region, we consider Faraday caustics as the only remaining explanation.

5.5.2 Faraday rotation

The Faraday depth structure seen in the diffuse emission shows a wealth of complex morphologies, such as the linear gradients and local minima/maxima previously described. A detailed analysis of all these features is beyond the scope of this work, but we do consider some possible causes of the Faraday depth gradients.

A gradient in Faraday depth can be caused by a gradient in the three factors that determine the Faraday depth: the free electron density, the parallel magnetic field, and the (physical) depth of the rotating volume. A gradient in the depth of the rotating region would naturally result if the emitting region was a sheet that was not perpendicular to the line of sight and the rotation occurred directly in front of the emitting region; if such an emitting sheet was reasonably flat the distance to the region, and the corresponding Faraday depth, could increase linearly with position. Gradients in the electron density might be expected on larger (kpc) scales, due to effects like the scale height of thermal electrons, but it is more difficult to produce smooth electron density gradients on the smaller (1–100 pc) scales that we expect to be probing.

The linear gradient in the northwest feature (Sec. 5.3.3.1) contains both negative and positive Faraday depths. The simplest explanation for this is a gradient in the parallel magnetic field that causes the sign to change from negative to positive. Alternative explanations would require two regions with oppositely directed magnetic fields and an electron density or distance gradient in one of the region, but then we would expect to see a Faraday caustic between these two regions and a corresponding emission feature. While there are many possible magnetic field configurations that would produce a gradient in the parallel component of the magnetic field, one possible configuration that would be consistent both with the observations and theoretical models [as discussed in Beck et al., 1996; Shukurov, 2004] is a magnetic filament bent into a loop through dynamo action [Zeldovich et al., 1983] such as is shown in Figure 5.13.

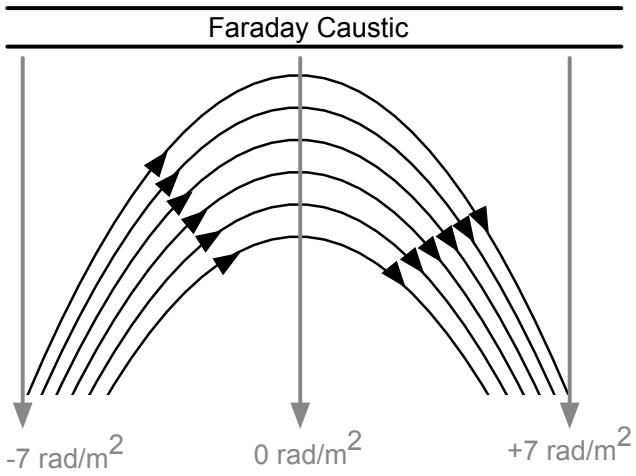

Figure 5.13: A magnetic field (black lines) configuration that would produce a gradient in Faraday depth. A magnetic loop like this could be produced through turbulent motion in the ISM [Zeldovich et al., 1983] and would produce a gradient in the parallel component of the magnetic field, which in turn creates a gradient in Faraday depth. The Faraday caustic further away provides the observed source of Faraday-thin polarized emission (grey lines).

5.5.3 Southwest gradient-HI correlation

The transition from a smooth linear gradient in Faraday depth outside of the H I filament to a more complicated morphology overlapping the filament is very intriguing. Since we are able to observe smooth transitions in the Faraday depth and polarized intensity in the filament region, we conclude that the H I filament is not associated with the source of the polarized emission (probably a caustic, per Sec. 5.5.1), and must lie in the foreground with the rest of the Faraday rotating structure. It is not clear, however, whether the filament is co-distant with the feature producing the Faraday depth gradient and disrupts the physical conditions producing the gradient, or if it is located in front of or behind the gradient, and produces an additional, more turbulent Faraday rotation contribution that distorts the shape of the gradient.

If we consider the filament as co-distant with the gradient feature, then one interpretation of the source of the gradient is in terms of a denser shell of ionized material surrounding the (predominantly neutral) H I filament, possibly material that is coalescing onto the filament (but still having a significant density of free electrons). If this is the case, then we expect to see a similar gradient on the other side of the filament; unfortunately that corresponds to the region where instrumental leakage from 3C295 overwhelms the real signal.

5.6 Depolarization by Faraday depth gradients

In addition to constraining possible magnetic field configurations, the Faraday depth gradients seen in this field are noteworthy in that they can be difficult to observe, requiring specific observational parameters. At higher frequencies, it is often the case that the Faraday depth resolution is so low that gradients in Faraday depth can only be measured in cases with very high signal-to-noise

ratios, which allows very accurate determination of the Faraday depth even with poor resolution. At lower frequencies, the image-plane resolution is often poorer, which can result in beam depolarization masking the polarized signal and making the gradients undetectable. Appendix 5.A describes this beam depolarization, and gives an approximate threshold for the conditions under which the depolarization becomes significant: polarization angle gradients shallower than 180° over the FWHM of the beam will not depolarize strongly.

We can use this threshold to determine the depolarization caused by the Faraday depth gradients in our observations. For our observations, with a FWHM of $4'$ and wavelengths between 1.9 m and 2.5 m, a polarization angle gradient of 180 deg FWHM^{-1} would be created by a Faraday depth gradient of 7.5–13 rad m^{-2} deg^{-1}. In the HETDEX field, we observed two very linear gradients in Faraday depth, with values of 2.6 and 13 rad m^{-2} deg^{-1}. The first is well inside the predicted range of minimal depolarization, but the second is at the upper limit of this range. This, combined with the lower polarized intensity of this gradient compared to the other polarized features in the data, suggests that this feature may be in the (narrow) regime of partial depolarization and may have a significantly higher intrinsic polarized intensity. It seems very plausible that the exact depolarization fraction depends significantly on the exact shape of the synthesized beam, so it is probably not reasonable to use the simple model of Appendix 5.A to predict the intrinsic polarized intensity.

We can also consider the detectability of Faraday depth gradients with other low-frequency radio observations. Lenc et al. [2016] observed faint diffuse emission with the MWA, at 154 MHz ($\lambda = 1.95$ m) with a resolution of $54'$. With the simple beam model of Appendix 5.A, the depolarization threshold corresponds to a Faraday depth gradient of 0.9 rad m^{-2} deg^{-1}. However, they also applied a Gaussian (u, v) taper to their data, which probably has the effect of making their beam more Gaussian-like and increasing the depolarization present. These observations are probably strongly effected by beam depolarization due to Faraday depth gradients; the majority of the structure seen in the HETDEX field could not be detected with these observational parameters.

There are plans to use the data from the Canadian H I Mapping Experiment (CHIME) to measure polarized foregrounds. CHIME will operate from 400–800 MHz, with a resolution of approximately $30'$. The Faraday depth gradient threshold for these parameters varies from 11–46 rad m^{-2} deg^{-1} from the bottom of the frequency band to the top, indicating these these observations should be less affected by gradient beam depolarization than our LOTSS observations.

We have not used the full resolution available with the LOTSS data, so a reprocessing of these data at higher resolution could improve the sensitivity to steeper Faraday depth gradients. At the same resolution as the LOTSS Stokes I data products, $25''$, the threshold for depolarization increases to 72–125 rad m^{-2} deg^{-1} at the bottom and top of the frequency band. However, the higher resolution results in a correspondingly lower sensitivity to diffuse emission, making it difficult to select a compromise between maximizing sensitivity to diffuse emission while preventing beam depolarization due to unresolved polarization angle gradients.

5.7 Conclusions

We have used 60 observations from the LOFAR Two-Meter Sky Survey to perform Faraday tomography covering the HETDEX region (right ascension from $10^{\rm h}30^{\rm m}$ to $15^{\rm h}30^{\rm h}$ and declination from 45° to 57°). We have produced a mosaic Faraday depth cube of this region at 4.′3 resolution, which shows polarized emission as a function of Faraday depth. The low-frequency nature of our data gives us a Faraday depth resolution of 1 rad m^{-2}, allowing us to probe very small variations in Faraday rotation. We achieve a typical sensitivity of 50–100 μJy PSF^{-1} RMSF^{-1}.

In our Faraday depth cube we see diffuse polarized emission across most of the region, at Faraday depths between -7 rad m^{-2} and +25 rad m^{-2}. This diffuse emission mostly takes the form of 'sheets', where the emission appears to be filamentary at any single Faraday depth but can be seen as a continuous feature distributed smoothly over Faraday depth. We are able to map out several of these sheets in different positions in the region. A few of these show very linear features, where emission over several square degrees has a smooth linear gradient in Faraday depth.

Motivated by the Faraday depth gradients seen in our observations, we considered the beam depolarization caused by the polarization angle gradients produced by such Faraday depth gradients. Many previous authors have considered the depolarization effects of a Gaussian PSF, which produces a very strong depolarization law, but other PSF shapes have not been studied. We have shown that an idealized PSF for an interferometer with uniform (u, v) coverage causes much weaker depolarization for some cases. We expect that most realistic observations will fall between these two cases, and suggest that Faraday depth gradients may be more likely to be detected than previously expected.

We have shown that the LOTSS data is well suited for Faraday tomography. However, the quality of the Faraday depth cubes could be improved significantly by developing a method to remove the instrumental polarization leakage. It may also be worthwhile to explore higher (image plane) resolution, as this could increase sensitivity to emission with stronger Faraday depth gradients. LOTSS will observe the entire sky north of declination zero, so a Faraday tomography survey, with excellent sensitivity and resolution (both image-plane and in Faraday depth), will soon be possible.

5.A Beam depolarization in a linear Faraday depth gradient

Gradients in Faraday depth with respect to position on the sky result in corresponding gradients in the polarization angle, which in turn produce beam depolarization when observed with a finite resolution. Here we consider the case of a uniform background emission source, with a (foreground) gradient in Faraday depth, corresponding to the sheets of emission and Faraday depth gradients we observe in our data. When a Gaussian beam is assumed, an analytical solution can be found, as described in Sokoloff et al. [1998]; Schnitzeler et al. [2015]. However, more realistic synthesized beams have not been considered in the literature, and below we show that this can make a significant difference in the expected depolarization.

Consider a gradient in Faraday depth with respect to a position variable x, $\frac{\mathrm{d}\phi}{\mathrm{d}x}$. The resulting intrinsic polarization, in the complex-polarization notation, is

$$\tilde{P}_{\mathrm{sky}}(x,\lambda) = \tilde{P}_0 \exp\left(2i\lambda^2 \frac{\mathrm{d}\phi}{\mathrm{d}x} x\right)$$

where λ is the observing wavelength and $\tilde{P}_0$ is the pre-Faraday rotation complex polarization. The observed polarization is the convolution of the intrinsic polarization with the telescope beam. In the case of a circular Gaussian beam ($\frac{1}{2\pi\sigma^2}\exp(-\frac{x^2+y^2}{2\sigma^2})$), the convolution integral can be solved analytically, resulting in the previously known result

$$\tilde{P}_{\mathrm{obs}}(x,\lambda) = \tilde{P}_0 \exp\left(2i\lambda^2 \frac{\mathrm{d}\phi}{\mathrm{d}x} x\right) \exp\left(-2\left(\lambda^2 \frac{\mathrm{d}\phi}{\mathrm{d}x}\sigma\right)^2\right). \tag{5.2}$$

The first part of this equation is identical to the intrinsic polarization and contains all the position dependence and the only complex terms, which means that the correct polarization angle, Faraday depth, and Faraday depth gradient are recovered, but the polarized intensity is modified by the later parts of the equation. The second part of the equation gives the depolarization, and shows that the depolarization is a very strong function of the wavelength, gradient, and beam size.

However, a Gaussian may not be the most accurate representation of the synthesized beam, particularly for diffuse emission where the CLEAN algorithm (and the corresponding Gaussian CLEAN beam) may not be applied. Previous calculations such as Tribble [1991], while not for the exact same model, have shown that Gaussian functions tend to cause much stronger depolarization than other functions. With this motivation, we have performed simulations of depolarization using a simple beam model based on uniform coverage in the (u,v) plane.

We considered the beam produced by an interferometer with uniform sensitivity in the (u,v) plane for $u-v$ distances less than some $\mathrm{UV}_{\mathrm{max}}$, which was a free parameter, and zero sensitivity for $u-v$ distances larger than this. The synthesized beam resulting from this (u,v) coverage is the Bessel function of the first kind of order one, which is the 2D analog of the sinc function which results from tophat sampling in a 1D Fourier transform. This beam model possesses sidelobes, which are not present in the Gaussian model and may affect the resulting measured polarized intensity.

This model also has an analytic solution, which can be found simply by exploiting properties of Fourier transforms. Since the observed polarization is the convolution of the intrinsic (sky) polarization with the telescope beam, we can move to the Fourier domain where the convolution becomes a multiplication and the beam becomes the (u,v) coverage:

$$\begin{aligned}
\mathcal{F}\{\tilde{P}_{\mathrm{obs}}(x,y)\} &= \mathcal{F}\{\tilde{P}_{\mathrm{sky}}(x) * \mathrm{Beam}(x,y)\} \\
&= \mathcal{F}\{\tilde{P}_{\mathrm{sky}}(x)\} \cdot \mathcal{F}\{\mathrm{Beam}(x,y)\} \\
&= \tilde{P}_0\, \delta\left(u - \frac{2\lambda^2}{2\pi}\frac{\mathrm{d}\phi}{\mathrm{d}x}\right) \cdot (W(u,v)) \\
\tilde{P}_{\mathrm{obs}}(x,y) &= \mathcal{F}^{-1}\{\tilde{P}_0\, \delta\left(u - \frac{2\lambda^2}{2\pi}\frac{\mathrm{d}\phi}{\mathrm{d}x}, v\right) \cdot (W(u,v))\} \\
&= \tilde{P}_0 \exp\left(2i\lambda^2 \frac{\mathrm{d}\phi}{\mathrm{d}x} x\right) W\left(\frac{2\lambda^2}{2\pi}\frac{\mathrm{d}\phi}{\mathrm{d}x}, 0\right).
\end{aligned}$$

where $W(u,v)$ is the sampling/weight function in the (u,v) plane. To this point, the result is general and works for any sampling function; using Gaussian weights gives the result from Eq. 5.2. For a weight function corresponding to uniform sensitivity out to a maximum baseline $\mathrm{UV}_{\mathrm{max}}$,

$$W(u,v) = \begin{cases} 1 \text{ for } & \sqrt{u^2+v^2} \leq \mathrm{UV}_{\mathrm{max}} \\ 0 \text{ for } & \sqrt{u^2+v^2} > \mathrm{UV}_{\mathrm{max}} \end{cases},$$

this produces a very interesting result that

$$\tilde{P}_{\mathrm{obs}}(x,y) = \begin{cases} \tilde{P}_{\mathrm{sky}}(x,\lambda) \text{ for } & \frac{2\lambda^2}{2\pi}\frac{\mathrm{d}\phi}{\mathrm{d}x} \leq \mathrm{UV}_{\mathrm{max}} \\ 0 \text{ for } & \frac{2\lambda^2}{2\pi}\frac{\mathrm{d}\phi}{\mathrm{d}x} > \mathrm{UV}_{\mathrm{max}} \end{cases}. \tag{5.3}$$

This model has three key parameters: the observing wavelength, λ, the longest baseline, $\mathrm{UV}_{\mathrm{max}}$, and the Faraday depth gradient, $\frac{\mathrm{d}\phi}{\mathrm{d}x}$. We found that we could reduce this to one parameter by converting our model into scale-free units: we replaced the $\mathrm{UV}_{\mathrm{max}}$ parameter with the synthesized beam full-width half max (FWHM), which is defined as FWHM$= \frac{\lambda}{\mathrm{UV}_{\mathrm{max}}}$; replaced the $\lambda^2\frac{\mathrm{d}\phi}{\mathrm{d}x}$ term in the intrinsic polarization with a single variable, the polarization angle gradient (with units of radians of rotation per beam FWHM); and expressed the position variable x in terms of the FWHM. The resulting condition for no depolarization is $\lambda^2\frac{\mathrm{d}\phi}{\mathrm{d}x}\,\mathrm{FWHM} < \pi$ rad.

The resulting model predicts the depolarization fraction (ratio of observed polarized intensity to intrinsic polarized intensity) as a function of the polarization angle gradient, as shown in Figure 5.14. The resulting depolarization behaviour is quite striking: while the Gaussian beam causes significant depolarization even for small polarization gradients, the uniform (u,v) coverage beam produces no depolarization for small polarization gradients, but depolarizes completely for gradients steeper than 180 degrees over the FWHM of the beam. This result shows that it is quite possible that polarization gradients could still be detected even when they were previously expected to be strongly depolarized. It may appear that this case is worse than the Gaussian for steep gradients, but at the threshold of 180° per FWHM the depolarization by the Gaussian beam would leave only $2.7\cdot10^{-9}$ of the original polarized flux, which would be undetectable under most observational conditions.

Most real observations probably fall in between these two cases. Our model assumes uniform sensitivity over the sampled region of the (u,v) plane, while real observations may use weighting or tapering profiles that cause the weight function, and thus the beam, to become closer to Gaussian shaped.

Acknowledgements
This work is part of the research programme 639.042.915, which is (partly) financed by the Netherlands Organisation for Scientific Research (NWO).

LOFAR, the Low Frequency Array designed and constructed by ASTRON, has facilities in several countries, that are owned by various parties (each with their own funding sources), and that are collectively operated by the International LOFAR Telescope (ILT) foundation under a joint scientific policy.

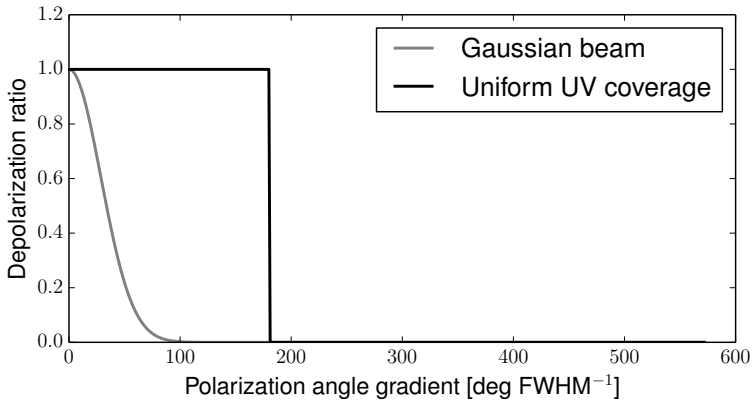

Figure 5.14: Predicted depolarization caused by a Gaussian beam or a beam resulting from uniform (u, v) coverage in a circle of radius $\mathrm{UV}_{\mathrm{max}}$, as a function of the polarization angle gradient. The Gaussian beam causes rapid depolarization, but the more realistic beam does not show any depolarization for gradients smaller than approximately 180° over the FWHM of the beam.

This research used ionospheric TEC maps produced by the Centre for Orbital Determination in Europe (CODE, http://aiuws.unibe.ch/ionosphere/). Some of the ISM tracer maps were downloaded from NASA's Legacy Archive for Microwave Background Data Analysis (LAMBDA)[4].

This research made extensive use of Astropy, a community-developed core Python package for Astronomy [Astropy Collaboration et al., 2013]; SciPy [Jones et al., 2001–]; NumPy [van der Walt et al., 2011]; IPython [Pérez & Granger, 2007]; matplotlib [Hunter, 2007]; the Common Astronomy Software Applications [CASA, McMullin et al., 2007]; and the Karma visualization tools [Gooch, 1996].

[4]https://lambda.gsfc.nasa.gov/product/foreground/f_products.cfm

Chapter 6

Conclusion

Magnetic fields in the interstellar medium remain mysterious in many respects, in large part due to the difficulty in measuring them. Most of the measurement techniques use polarization of electromagnetic waves, but produce measurements that are integrated or averaged over the whole line of sight. Faraday tomography is a new technique that allows for detected polarized radio emission to be separated by the amount of Faraday rotation, allowing for multiple polarized features along any line of sight to be identified and analyzed, which in turn gives us more information that can be used to constrain the magnetic field along the observed lines of sight.

This thesis has focused on further developing the use of Faraday tomography with low-frequency radio observations. In Chapter 2, I presented LOFAR observations of the nearby galaxy IC342, and used Faraday tomography to identify and study the diffuse polarized Galactic synchrotron emission present in that field. Two clear, overlapping features, with a small separation in Faraday depth ($\approx$8 rad m^{-2}) were identified. This demonstrated the value of low-frequency Faraday tomography: higher frequency (1 GHz and above) observations wouldn't have the Faraday depth resolution to separate and identify both features.

These two features were also shown to be necessarily Faraday thin (narrower than 1 rad m^{-2} in Faraday depth), which prompted me to consider and describe the physical conditions in the ISM that would lead to Faraday thin polarization features. Using maps of the local ISM structure, I identified the source of the two observed features as two regions of neutral gas located just outside the Local Bubble; this was the first time that diffuse polarization features seen with Faraday tomography were connected to specific ISM structures.

In Chapter 3, I tested the method used to correct for the effects of ionospheric Faraday rotation in LOFAR observations. I found that the method could be applied successfully to LOFAR data, and that the measured Faraday depth and polarized intensity changed as expected when the correction was applied. I tested two different sources for the TEC data used in the correction, CODE and ROB, and found, counterintuitively, that the data from CODE more accurately represented the behaviour of the data despite having lower spatial and temporal resolution than the data from ROB. I showed that we can successfully predict the time-variability in the ionosphere with an error of less than 0.1 rad m^{-2}, but the accuracy of the absolute value of the prediction remains unknown.

For Chapter 4 I developed a data processing pipeline to identify and characterize polarized point sources in LOFAR observations. This pipeline was developed with, and tested on, 60 observations from the LOFAR Two-Meter Sky Survey (LOTSS). The pipeline identifies candidate sources that stand out from the surrounding foreground emission, performs a fitting procedure, and evaluates the fit to determine if the source is real or a processing artifact. A new error estimation algorithm was developed, which generates random realizations of noise with correlation structure very similar to that expected in the real data and uses these noise realizations to perform Monte-Carlo simulations of the source fitting procedure and produce estimates of the uncertainties in the fitted parameters.

The result of applying this pipeline to the LOTSS test fields was a catalog of 102 low-frequency polarized sources, the first catalog of polarized sources at such a low frequency. Due to the large overlap between adjacent fields, many sources were detected several times, allowing for consistency checks between independent measurements. These checks found that the measured Faraday depths were usually consistent to better than 0.1 rad m^{-2}, and that the errors estimated using the correlated-noise Monte-Carlo method were accurate to within a few percent. The final catalog was compared against the higher-frequency Taylor et al. [2009] polarized source catalog, and was found to be generally consistent.

The same LOTSS observations were also used to probe the diffuse emission, which was described in Chapter 5. Faraday tomography was applied to all of the observations, and a combined Faraday depth cube was produced; this was the first time multiple LOFAR polarization observations have been combined. The resulting Faraday depth cube covered 570 square degrees with high image-plane and Faraday depth resolution and high sensitivity. Diffuse polarized emission was observed in most of the field, and several distinct features were observed in the emission and its Faraday depth distribution. This was the first time these features could be observed on scales larger than a single LOFAR observation, and proved that these features can have large sizes, more than 12 degrees across.

The most interesting of these features were two large linear gradients in Faraday depth, where the Faraday depth of emission varied smoothly across a large region, producing long, straight, lines of constant Faraday depth several degrees long. These gradients were remarkable for two reasons. First, they indicate that the Faraday rotation (and thus the magnetic field and free electron density) must be dominated by smooth, large-scale structures rather than the net sum of many random or turbulent contributions. Second, such gradients would be expected to be strongly affected by beam depolarization, especially if the synthesized beam is Gaussian-like. I have shown that other shapes of synthesized beams can cause much lower beam depolarization, which is necessary to explain the observed gradients.

6.1 Future directions

This work has only scratched the surface of what can be done with low-frequency Faraday tomography. Below I describe a number of directions in which this work could be continued, divided somewhat coarsely into technical developments and scientific questions.

6.1.1 Technical developments

While the data being produced by LOFAR, and by LOTSS specifically, is of excellent quality for Faraday tomography, there remain two main aspects of calibration that need to be further explored to get the most of the data. The first is the development of methods of direction-dependent calibration, which is required to achieve the full resolution possible with LOFAR while minimizing the amount of image artifacts; since this affects total intensity imaging as well, such methods have been in development for several years [e.g. van Weeren et al., 2016]. However, the effects of these calibration methods on the observed polarized emission has not yet been thoroughly tested. Second, a method of removing the polarization leakage needs to be developed. The polarization leakage is the primary source of image artifacts in the current Faraday depth cubes, especially at the lower resolution used to study diffuse emission, and is the primary problem preventing quantitative statistical analysis of LOFAR polarization data. Some work has been done on this problem (e.g. using the SAGECAL software package, Yatawatta et al. [2008]), but a general, computationally efficient method has not yet been developed.

Another area where some investigation could be very beneficial is in the visualization of Faraday depth cubes. To date, the typical method of visualizing these cubes is to consider sequences of individual slices (as in Chapters 2 and 5) in combination with Faraday spectra of selected positions (as in Chapters 2 and 4). Various method of collapsing cubes into colour images have been attempted (as in Chapters 2 and 5), but are usually not able to fully present the complexity present in the data. The use of 3D visualization techniques, such as those developed to look at H I position-velocity cubes [e.g. Kent, 2013; Rosen et al., 2017], may be very useful in the interpretation and presentation of Faraday depth cubes but very little work has been done on adapting these methods to such data.

Much of the work behind Chapters 4 and 5 was the development of prototype data processing pipelines to produce Faraday depth cubes from LOTSS data. These pipelines have been shown to be effective, and the resulting Faraday depth cubes are of excellent quality. LOTSS is expected to observe the entire sky north of declination 0°, and by incorporating the polarization pipelines into the LOTSS data processing, it will be possible to produce a parallel Faraday tomography survey, covering the entire northern sky. There are aspects of the pipelines that can be improved to maximize the final data quality, such as methods of calibrating for the polarization leakage as described previously, but in principle the prototype pipelines could be run as-is with a low manpower requirement. Such a survey would be useful not just for diffuse polarization studies and polarized source catalogs, but also for investigating polarization and magnetic field structure in other objects, including nearby galaxies, galaxy clusters, and radio relics.

6.1.2 Scientific questions

There are a number of avenues available for further analysis of LOFAR Faraday tomography data. If the data artifacts caused by instrumental polarization leakage can be solved, many new quantitative methods can be applied. For example, statistical analysis of polarization fluctuations can be used to explore the turbulent properties of the magnetic field, including the key turbulent scales, the degree of order, anisotropy in the turbulence, and magnetic helicity [Iacobelli et al., 2013; Lazarian & Pogosyan, 2015].

An interesting area for further investigation is relating polarized emission and Faraday depth features to structures in the ISM observed with other tracers, as this would give us additional information (such as distances) that is very useful in constraining magnetic field models. It may also be possible to map out the magnetic fields in objects like supernova remnants, taking advantage of the very high Faraday depth resolution offered by low-frequency observations. The LOTSS pointings near the Galactic plane may be well suited for such investigations, as much more ISM structure is expected at small distance from the Galactic midplane.

The exploration of Faraday complexity, the presence of multiple Faraday-thin or -thick components, in unresolved polarized sources is still in early stages. There has been some work on this at higher frequencies [Anderson et al., 2016], and some evidence for multiple-component sources in LOFAR data (Chapter 4), but relatively little is known about the number and nature of such sources.

A related, but more theoretical, direction for future development is investigating simulated Faraday depth spectra made from detailed ISM simulations. Relatively little is known about the expected features in Faraday depth spectra caused by the ISM; for example, while there is some evidence that Faraday caustics produced by the large-scale magnetic field exist in large sheets [Bell et al., 2011], it is not clear what the topology of a turbulent magnetic field Faraday caustic would be and how this would appear in Faraday depth cubes. It would be very useful to generate synthetic Faraday depth cubes using detailed, multi-phase simulations of the ISM, to check which ISM features are observable (and whether this matches qualitative predictions, such as those in Chapter 2) and to identify specific signatures of different features. There has been some very promising initial work in this direction [e.g. Ideguchi et al., 2017], but this has largely focused on integrated polarization of galaxies, and the effects of limited resolution and Faraday thickness sensitivity have not be considered.

To summarize, the interpretation of Faraday depth cubes, and especially of diffuse features caused by the interstellar medium, is still in an early stage, and a great deal more work needs to be done before we fully understand how to interpret and analyze these data. However, there is a great detail of information on the structure, behaviour, and evolution of magnetic fields in the ISM hidden inside these observations, making the effort to unlock this information a worthwhile exercise.

Bibliography

F. Aharonian, A. Akhperjanian, M. Beilicke, et al., 2004. *ApJ*, 614:897–913.

C. S. Anderson, B. M. Gaensler, & I. J. Feain, 2016. *ApJ*, 825:59.

Astropy Collaboration, T. P. Robitaille, E. J. Tollerud, et al., 2013. *A&A*, 558:A33.

R Beck, 2007. *Astronomy*, 556:539–556.

R. Beck, A. Brandenburg, D. Moss, et al., 1996. *ARA&A*, 34:155–206.

R. Beck, P. Frick, R. Stepanov, et al., 2012. *A&A*, 543:A113.

R. Beck & M. Krause, 2005. *Astronomische Nachrichten*, 326:414–427.

M. R. Bell, H. Junklewitz, & T. A. Enßlin, 2011. *A&A*, 535:A85.

A. Beresnyak & A. Lazarian, 2015. In *Magnetic Fields in Diffuse Media*, editors A. Lazarian, E. M. de Gouveia Dal Pino, & C. Melioli, volume 407 of *Astrophysics and Space Science Library*, page 163.

Bergeot, Nicolas, Chevalier, Jean-Marie, Bruyninx, Carine, et al., 2014. *J. Space Weather Space Clim.*, 4:A31.

G. Bernardi, L. J. Greenhill, D. A. Mitchell, et al., 2013. *ApJ*, 771:105.

A. V. Bilous, V. I. Kondratiev, M. Kramer, et al., 2016. *A&A*, 591:A134.

A. Boulares & D. P. Cox, 1990. *ApJ*, 365:544–558.

J. Bovy, H.-W. Rix, G. M. Green, et al., 2016. *ApJ*, 818:130.

A. Brandenburg, 2015. In *Magnetic Fields in Diffuse Media*, editors A. Lazarian, E. M. de Gouveia Dal Pino, & C. Melioli, volume 407 of *Astrophysics and Space Science Library*, page 529.

M. A. Brentjens, 2011. *A&A*, 526:A9.

M. A. Brentjens & A. G. de Bruyn, 2005. *A&A*, 441:1217–1228.

W. N. Brouw & T. A. T. Spoelstra, 1976. *A&AS*, 26:129.

J. C. Brown, M. Haverkorn, B. M. Gaensler, et al., 2007. *ApJ*, 663:258–266.

J. C. Brown & A. R. Taylor, 2001. *ApJ*, 563:L31–L34.

J. C. Brown, A. R. Taylor, & B. J. Jackel, 2003. *ApJS*, 145:213–223.

B. J. Burn, 1966. *MNRAS*, 133:67.

A. R. Choudhuri, 1998. *The physics of fluids and plasmas : an introduction for astrophysicists /*. Cambridge University Press.

J. J. Condon, W. D. Cotton, E. W. Greisen, et al., 1998. *AJ*, 115:1693–1716.

J. M. Cordes & T. J. W. Lazio, 2002. *ArXiv Astrophysics e-prints*.

R. M. Crutcher, 2015. In *Magnetic Fields in Diffuse Media*, editors A. Lazarian, E. M. de Gouveia Dal Pino, & C. Melioli, volume 407 of *Astrophysics and Space Science Library*, page 445.

A. G. de Bruyn & M. A. Brentjens, 2005. *A&A*, 441:931–947.

B. T. Draine, 2011. *Physics of the Interstellar and Intergalactic Medium*. Princeton University Press.

J. S. Farnes, S. P. O'Sullivan, M. E. Corrigan, et al., 2014. *ApJ*, 795:63.

G. R. Farrar, 2016. *IAU Focus Meeting*, 29:723–726.

K. M. Ferrière, 2001. *Reviews of Modern Physics*, 73:1031–1066.

D. P. Finkbeiner, 2003. *ApJS*, 146:407–415.

X. Y. Gao, W. Reich, P. Reich, et al., 2015. *A&A*, 578:A24.

R. Gießübel, G. Heald, R. Beck, et al., 2013. *A&A*, 559:A27.

R. Gooch, 1996. In *Astronomical Data Analysis Software and Systems V*, editors G. H. Jacoby & J. Barnes, volume 101 of *Astronomical Society of the Pacific Conference Series*, page 80.

A. D. Gray, T. L. Landecker, P. E. Dewdney, et al., 1998. *Nature*, 393:660–662.

G. M. Green, E. F. Schlafly, D. P. Finkbeiner, et al., 2015. *ApJ*, 810:25.

D. A. Gurnett & A. Bhattacharjee, 2005. *Introduction to Plasma Physics*. Cambridge University Press.

D. A. Gurnett, W. S. Kurth, D. L. Kirchner, et al., 2004. *Space Sci. Rev.*, 114:395–463.

J. P. Hamaker, J. D. Bregman, & R. J. Sault, 1996. *Astronomy and Astrophysics Supplement Series*, 117:137–147.

M. Haverkorn, J. C. Brown, B. M. Gaensler, et al., 2008. *ApJ*, 680:362–370.

M Haverkorn, P Katgert, & a. G de Bruyn, 2004. *A&A*, 427:12.

G. Heald, R. Braun, & R. Edmonds, 2009. *A&A*, 503:409–435.

G. H. Heald, R. F. Pizzo, E. Orrú, et al., 2015. *A&A*, 582:A123.

E. Hecht, 2001. *Optics 4th edition*. Pearson.

A. S. Hill, T. L. Landecker, E. Carretti, et al., 2017. *ArXiv e-prints*.

G. J. Hill, K. Gebhardt, E. Komatsu, et al., 2008. In *Panoramic Views of Galaxy Formation and Evolution*, editors T. Kodama, T. Yamada, & K. Aoki, volume 399 of *Astronomical Society of the Pacific Conference Series*, page 115.

J. D. Hunter, 2007. *Computing In Science & Engineering*, 9(3):90–95.

M. Iacobelli, M. Haverkorn, & P. Katgert, 2013. *A&A*, 549:A56.

M. Iacobelli, Marijke Haverkorn, E. Orrú, et al., 2013. *Astronomy and Astrophysics*, 558:A72.

S. Ideguchi, Y. Tashiro, T. Akahori, et al., 2017. *ArXiv e-prints*.

H. T. Intema, P. Jagannathan, K. P. Mooley, et al., 2016. *ArXiv e-prints*.

J. D. Jackson, 1998. *Classical Electrodynamics, 3rd Edition*. Wiley.

T. R. Jaffe, J. P. Leahy, A. J. Banday, et al., 2010. *MNRAS*, 401:1013–1028.

R. Jansson & G. R. Farrar, 2012. *ApJ*, 757:14.

G. Jee, H.-B. Lee, Y. H. Kim, et al., 2010. *Journal of Geophysical Research: Space Physics*, 115(A10):n/a–n/a. A10319.

V. Jelić, A. G. de Bruyn, M. Mevius, et al., 2014. *A&A*, 568:A101.

V. Jelić, A. G. de Bruyn, V. N. Pandey, et al., 2015. *A&A*, 583:A137.

E. B. Jenkins, 2013. *ApJ*, 764:25.

Eric Jones, Travis Oliphant, Pearu Peterson, et al., 2001–. "SciPy: Open source scientific tools for Python." [Online: www.scipy.org].

B. R. Kent, 2013. *PASP*, 125:731.

R. Lallement, J.-L. Vergely, B. Valette, et al., 2014. *A&A*, 561:A91.

T. L. Landecker & R. Wielebinski, 1970. *Australian Journal of Physics Astrophysical Supplement*, 16:1.

W. M. Lane, W. D. Cotton, S. van Velzen, et al., 2014. *MNRAS*, 440:327–338.

a Lazarian & D Pogosyan, 2015. *ArXiv*, (2003):1 – 23.

E. Lenc, B. M. Gaensler, X. H. Sun, et al., 2016. *ApJ*, 830:38.

R. N. Manchester, 1972. *ApJ*, 172:43.

R. N. Manchester, G. B. Hobbs, A. Teoh, et al., 2005. *AJ*, 129:1993–2006.

S. A. Mao, N. M. McClure-Griffiths, B. M. Gaensler, et al., 2012. *ApJ*, 755:21.

S. A. Mao, E. Zweibel, A. Fletcher, et al., 2015. *ApJ*, 800:92.

J. P. McMullin, B. Waters, D. Schiebel, et al., 2007. In *Astronomical Data Analysis Software and Systems XVI*, editors R. A. Shaw, F. Hill, & D. J. Bell, volume 376 of *Astronomical Society of the Pacific Conference Series*, page 127.

M. Moscibrodzka, J. Dexter, J. Davelaar, et al., 2017. *ArXiv e-prints*.

D. D. Mulcahy, A. Horneffer, R. Beck, et al., 2014. *A&A*, 568:A74.

M. E. Nord, P. A. Henning, R. J. Rand, et al., 2006. *AJ*, 132:242–252.

A. R. Offringa, J. J. van de Gronde, & J. B. T. M. Roerdink, 2012. *A&A*, 539:A95.

N. Oppermann, H. Junklewitz, M. Greiner, et al., 2014. *A&A*, pages 1–33.

E. Orrù, S. van Velzen, R. F. Pizzo, et al., 2015. *A&A*, 584:A112.

S. P. O'Sullivan, S. Brown, T. Robishaw, et al., 2012. *MNRAS*, 421:3300–3315.

A. G. Pacholczyk, 1970. *Radio astrophysics. Nonthermal processes in galactic and extragalactic sources*. W. H. Freeman.

V. N. Pandey, J. E. van Zwieten, A. G. de Bruyn, et al., 2009. In *The Low-Frequency Radio Universe*, editors D. J. Saikia, D. A. Green, Y. Gupta, et al., volume 407 of *Astronomical Society of the Pacific Conference Series*, page 384.

Fernando Pérez & Brian E. Granger, 2007. *Computing in Science and Engineering*, 9(3):21–29.

R F Pizzo, A G De Bruyn, G Bernardi, et al., 2011. *A&A*, 104:1–23.

Planck Collaboration, R. Adam, P. A. R. Ade, et al., 2016. *A&A*, 594:A10.

L. Pratley & M. Johnston-Hollitt, 2016. *MNRAS*, 462:3483–3501.

R. J. Rand & A. G. Lyne, 1994. *MNRAS*, 268:497.

M. Remazeilles, C. Dickinson, A. J. Banday, et al., 2015. *MNRAS*, 451:4311–4327.

R. B. Rengelink, Y. Tang, A. G. de Bruyn, et al., 1997. *A&AS*, 124:259–280.

P. Rosen, B. Wang, A. Seth, et al., 2017. *ArXiv e-prints*.

A. Rovira-Garcia, J. M. Juan, J. Sanz, et al., 2016. *Journal of Geodesy*, 90(3):229–240.

G. B. Rybicki & A. P. Lightman, 1985. *Radiative processes in astrophysics.* John Wiley & Sons.

A. M. M. Scaife & G. H. Heald, 2012. *MNRAS*, 423:L30–L34.

D. H. F. M. Schnitzeler, J. K. Banfield, & K. J. Lee, 2015. *MNRAS*, 450:3579–3596.

T. W. Shimwell, H. J. A. Röttgering, P. N. Best, et al., 2017. *A&A*, 598:A104.

A. Shukurov, 2004. *ArXiv Astrophysics e-prints*.

J. F. L. Simmons & B. G. Stewart, 1985. *A&A*, 142:100–106.

C. Sobey, A. Noutsos, & M. Kramer, 2010. In *25th Texas Symposium on Relativistic Astrophysics*, page 234.

D. D. Sokoloff, A. A. Bykov, A. Shukurov, et al., 1998. *MNRAS*, 299:189–206.

C. Sotomayor-Beltran, C. Sobey, J. W. T. Hessels, et al., 2013. *A&A*, 552:A58.

S. R. Spangler, 2009. *Space Sci. Rev.*, 143:277–290.

J. M. Stil, B. W. Keller, S. J. George, et al., 2014. *ApJ*, 787:99.

J. M. Stil, A. R. Taylor, & C. Sunstrum, 2011. *ApJ*, 726:4.

C. Tasse, S. van der Tol, J. van Zwieten, et al., 2013a. *A&A*, 553:A105.

C. Tasse, S. van der Tol, J. van Zwieten, et al., 2013b. *A&A*, 553:A105.

A. R. Taylor, J. M. Stil, & C. Sunstrum, 2009. *ApJ*, 702:1230–1236.

A. G. G. M. Tielens, 2010. *The Physics and Chemistry of the Interstellar Medium*. Cambridge University Press.

P. C. Tribble, 1991. *MNRAS*, 250:726–736.

S. . van der Tol, B. D. Jeffs, & A.-J. . van der Veen, 2007. *IEEE Transactions on Signal Processing*, 55:4497–4510.

C. L. Van Eck, J. C. Brown, J. M. Stil, et al., 2011. *ApJ*, 728:97.

C. L. Van Eck, M. Haverkorn, M. I. R. Alves, et al., 2017. *A&A*, 597:A98.

M. P. van Haarlem, M. W. Wise, A. W. Gunst, et al., 2013a. *A&A*, 556:A2.

M. P. van Haarlem, M. W. Wise, A. W. Gunst, et al., 2013b. *A&A*, 556:A2.

S. van Loo, T. W. Hartquist, & S. A. E. G. Falle, 2012. *Astronomy and Geophysics*, 53(5):5.31–5.36.

R. J. van Weeren, W. L. Williams, M. J. Hardcastle, et al., 2016. *ApJS*, 223:2.

J.-L. Vergely, B. Valette, R. Lallement, et al., 2010. *A&A*, 518:A31.

Stéfan van der Walt, S. Chris Colbert, & Gaël Varoquaux, 2011. *Computing in Science & Engineering*, 13(2):22–30.

M. H. Wieringa, A. G. de Bruyn, D. Jansen, et al., 1993. *A&A*, 268:215–229.

B. Winkel, J. Kerp, L. Flöer, et al., 2016. *A&A*, 585:A41.

M. G. Wolfire, D. Hollenbach, C. F. McKee, et al., 1995. *ApJ*, 443:152–168.

M. Wolleben, A. Fletcher, T. L. Landecker, et al., 2010. *ApJ*, 724:L48–L52.

J.˜M. J.M. Wrobel & R.˜C. R.C. Walker, 1999. In *Synthesis Imaging in Radio Astronomy II*, editors G.˜B. Taylor, C.˜L. Carilli, & R.˜A. Perley, volume 180 of *Astronomical Society of the Pacific Conference Series*, page 171.

J. M. Yao, R. N. Manchester, & N. Wang, 2017. *ApJ*, 835:29.

S. Yatawatta, S. Zaroubi, G. de Bruyn, et al., 2008. *ArXiv e-prints*.

S. Zaroubi, V. Jelić, A. G. de Bruyn, et al., 2015. *MNRAS*, 454:L46–L50.

I. B. Zeldovich, A. A. Ruzmaikin, & D. D. Sokolov, editors, 1983. *Magnetic fields in astrophysics*, volume 3.

Summary

While most people think of the space between stars as being completely empty (perhaps in large part due to the expression "the vacuum of space"), interstellar space is filled with tenuous material. This interstellar medium (ISM) occupies most of the volume of our Galaxy, and consists of matter in many states, including atomic and molecular gas, plasma, dust particles, and highly energetic atomic and subatomic particles (cosmic rays). This material is responsible for such astrophysical phenomena as the birth of new stars, the dark dust lanes seen in the Milky Way, and many nebulae.

Interstellar space is also threaded with magnetic fields. These magnetic fields are generated by the motion of the plasma in the ISM, through dynamo processes similar to those that generate the Earth's magnetic field in its molten core. The magnetic fields in turn guide the motion of the ISM, pulling it into filamentary structures and sometimes supporting it against gravity.

Magnetic fields in the ISM are difficult to study, because they don't produce any light for us to observe. Instead we must observe how light[1] from other astrophysical sources is altered by the presence of the magnetic fields. Most of the physical processes by which magnetic fields alter light involve the polarization of light, a property that the human eye (mostly) cannot see. The magnetic fields in the ISM affect how the ISM material interacts with light, producing a change in the polarization properties that we can measure and use to infer the properties of the magnetic field causing the change.

One of these processes is Faraday rotation, where the polarization of light is altered when it passes through certain magnetized materials, such as the plasma in the ISM. By measuring the resulting polarization afterwards, we can infer properties of the magnetized plasma responsible for the Faraday rotation, and in turn learn about the magnetic fields in the ISM. The strength of Faraday rotation in magnetized plasma depends on the wavelength of the polarized light, with longer wavelengths being much more strongly affected. For typical conditions in the ISM, it is necessary to use radio waves to measure Faraday rotation, as they have long enough wavelengths for the effect to become strong enough to measure.

As a result, the study of interstellar magnetic fields through Faraday rotation involves three

[1] By light, I mean all electromagnetic waves, from radio waves through optical light (which our eyes see) to gamma rays.

different physical phenomena that are invisible to the human eye (or other senses): we look at the *polarization* properties of *radio waves* to infer the presence of a *magnetic field*.

Observing astrophysical radio waves requires a radio telescope. The Low Frequency Array, LOFAR, is a new European radio telescope designed to operate at very long wavelengths. LOFAR is a 'software telescope', with no moving parts; it consists of many radio antennas and the signals from all the antennas are combined using signal processing techniques to focus on different locations in the sky. The long wavelengths that LOFAR observes gives it a unique advantage for Faraday rotation studies, as Faraday rotation is very strong at these wavelengths allowing for high precision measurements.

This thesis

The work in this thesis focused on testing the ability of LOFAR to measure polarized signals and Faraday rotation, and in turn probe the magnetic field in the local region of the ISM. If successful, the goal was to identify and study small structures in the magnetic field that could not be seen by previous generations of radio telescopes.

This work began, in Chapter 1, with the processing of a single LOFAR observation to see if polarized emission could be observed. This field was centered on the nearby galaxy IC342, but the goal was to observe polarized emission and Faraday rotation from within our own Galaxy. I successfully observed bright polarized radio emission, and identified two clear, separate features in the Faraday rotation of this emission. These features had very small differences in their Faraday rotation, which could not have been observed using a higher frequency radio telescope; this showed that low frequency data can be very useful in identifying these kind of subtle features in the polarization. These two features were matched to two clouds of neutral gas known to exist in the local ISM; this matching gave additional information on the distance and source of these features, and allowed us to further constrain the properties of the magnetic field.

Accurate calibration is essential for reliable polarization measurements. In Chapter 2, I tested software for calibrating and correcting for the polarization-altering effects of the Earth's ionosphere, a layer of plasma in the upper regions of the atmosphere. This correction is required to ensure that the Faraday rotation caused by the ionosphere is not included when measuring astrophysical Faraday rotation. I tested two different sources of data used to determine the correction, to determine which one was more effective, and measured how accurate the software was in predicting variations in the correction over time spans of several hours. These tests were essential in evaluating the quality of the calibration, and in turn the resulting measurements, for all the other chapters in the thesis.

With the successful results from the first observation, the next step was to expand to larger regions of the sky. The LOFAR Two-meter Sky Survey, LOTSS, is a project that will map out the entire northern sky using LOFAR. I developed a data processing pipeline for LOTSS data that performs the necessary calibration and processing steps for polarization analysis. This pipeline was used to analyze the first 60 fields of LOTSS. The results of this are in Chapters 3 and 4.

Chapter 3 focuses on the analysis of bright extra-galactic polarized radio sources. These are distant objects, like radio-bright galaxies, that produce polarized radio waves. They are interesting for two reasons: first, the Faraday rotation of their emission can be used to study magnetic fields in

our Galaxy; second, the polarization can also give us information on the properties of the magnetic fields in the source, allowing us to study magnetic fields in distant radio galaxies. The polarization properties of these sources at LOFAR frequencies have not been widely studied to date; there have been a few studies involving a handful of objects, but not enough for detailed statistical analysis. From the LOTSS data, I was able to find 102 extragalactic polarized radio sources, plus one polarized pulsar (which is inside our Galaxy). Most of these had already been observed at higher frequencies, but this was the first low frequency measurement of their polarization. My measurements are mostly consistent with the higher frequency data, but show some differences that hint at some interesting properties of the magnetic fields; more analysis is needed to interpret this and to determine the nature of these sources. A large part of this work was also to test different methods of measuring the polarization from the LOTSS data, with the intention of using these results to guide the design of software to analyze the polarization all of the future LOTSS data.

Chapter 4 focuses on the diffuse polarized emission from our own Galaxy, applying the analysis techniques from Chapter 1 to the LOTSS data. Similarly to the IC342 field, I found polarized emission from our own Galaxy, rich in different structures and behaviours (as can be seen on the cover of this thesis). Many of these structures were larger than had ever been observed before, over 15 degrees in length (for reference, the handle of the Big Dipper is roughly 15 degrees across), and could not have been seen in previous observations with smaller fields-of-view. In particular, I found two very straight features with smooth gradients in the Faraday rotation; the existence of these smooth structures is very interesting, as they could not come from magnetic fields that are strongly turbulent and chaotic; the magnetic field responsible for these must be similarly smooth. I looked at how the polarization features I observed compared to other aspects of the ISM and found an interesting connection: one of the straight, smooth gradients that I found was connected to the edge of a cloud of neutral hydrogen gas. The two did not overlap, but the edge of the hydrogen cloud traced out the edge of the polarization feature; the hydrogen cloud must be shaping the properties of the Faraday rotation in the region around it. This again shows that with this kind of data it is possible to relate features in the polarization to the behaviour of the ISM.

Together, this work has shown that this sort of analysis with LOFAR data can yield new and exciting information on magnetic fields in the local interstellar medium. The LOTSS survey will eventually observe the entire northern sky (the work in this thesis covers only 3% of that area), so there is the potential to expand this work to include all of that data as it is observed, eventually producing a high-quality map of the low-frequency polarization for half of the full sky. This work has also shown how this data can be linked to other measurements of the structure of the ISM, allowing us to better understand how the magnetic field is tied to its environment.

Samenvatting

Hoewel de meeste mensen aannemen dat de ruimte tussen de sterren leeg is, is deze zogenaamde *interstellaire ruimte* gevuld met ijl materiaal. Deze interstellaire materie (ISM) neemt het grootste deel van het volume in onze Melkweg in en bestaat uit materie in vele toestanden, zoals atomair en moleculair gas, plasma, stofdeeltjes en hoog-energetische atomaire en subatomaire deeltjes (kosmische straling). Dit materiaal is verantwoordelijk voor astrofysische fenomenen zoals de geboorte van nieuwe sterren, donkere stofbanen die gezien worden in de Melkweg en vele nevels.

De ruimte tussen de sterren is ook vergeven van magneetvelden. Deze magneetvelden worden gemaakt door de beweging van het plasma in het ISM, door dynamo-processen die lijken op de processen die het aardmagnetisch veld maken in de gesmolten aardkern. De magneetvelden op hun beurt beïnvloeden de beweging van het ISM, trekken het tot lange draden of ondersteunen het tegen zwaartekracht.

Magneetvelden in het ISM zijn moeilijk te bestuderen, vooral omdat ze geen straling produceren, die voor ons zichtbaar is. In plaats van directe straling te meten zullen we moeten bestuderen hoe licht[2] van andere astrofysische bronnen verandert door de aanwezigheid van magneetvelden. De meeste fysische processen rond het veranderen van licht door magneetvelden draaien om polarisatie van licht, een eigenschap van licht dat (voor het grootste deel) niet met het blote oog waargenomen kan worden. De magneetvelden in het ISM beïnvloeden hoe het ISM materiaal reageert met licht, zoals het veranderen van de polarisatie-eigenschappen die we kunnen meten. De verandering van deze eigenschappen kunnen we gebruiken om meer te weten te komen over de magneetvelden die deze veranderingen veroorzaken.

Een van deze processen is Faradaydraaiing. Hier wordt de polarisatie van het licht veranderd terwijl het licht door bepaalde gemagnetiseerde materialen beweegt, zoals plasma in het ISM. Door de resulterende polarisatie te meten kunnen we de eigenschappen van de gemagnetiseerde materialen verantwoordelijk voor de Faradaydraaii'ng achterhalen en hierdoor meer leren over de magneetvelden in dit ISM. De sterkte van de Faradaydraaiing in een gemagnetiseerd plasma is afhankelijk van de golflengte van het gepolariseerde licht. Langere golflengtes worden hierbij sterker beïnvloed. Voor gemiddelde omstandigheden in het ISM moeten radiogolven gebruikt

[2]Met licht worden hier alle vormen van electromagnetische straling bedoeld, van radiogolven naar optisch licht (wat onze ogen kunnen zien) tot gamma straling

worden om de Faradaydraaiing te meten: de golflengten van radiostraling zijn lang genoeg om een, voor ons, meetbaar resultaat te produceren.

De studie van de interstellaire magneetvelden via Faradaydraaiing betreft drie verschillende fysische fenomenen die onzichtbaar zijn voor het menselijk oog (en de andere zintuigen). Namelijk, we kijken naar *polarisatie*-eigenschappen van *radiogolven* om de aanwezigheid van *magneetvelden* af te leiden.

Voor het waarnemen van radiogolven is een radiotelescoop nodig. De Low Frequency Array, of LOFAR, is een Europese radiotelescoop en is ontwikkeld om de lange golflengten nodig voor dit onderzoek op te vangen. LOFAR is een 'software telescoop' zonder bewegende delen. De telescoop bestaat uit vele radio-antennes en de signalen van al deze antennes worden zodanig gecombineerd, dat er naar verschillende locaties aan de hemel gekeken kan worden. De lange golflengten die worden gemeten door LOFAR zijn bij uitstek geschikt voor het bestuderen van Faradaydraaiing: bij deze golflengten is de Faradaydraaiing erg sterk en kunnen we dit fenomeen met hoge precisie bestuderen.

Dit proefschrift

Het werk in dit proefschrift richt zich op het testen van de mogelijkheid om deze polarisatiesignalen en Faradaydraaiing te meten met LOFAR en hierdoor de magneetvelden in het ISM in het nabije deel van de Melkweg te testen. Indien succesvol is het doel om kleine structuren in het magneetveld te identificeren, aangezien deze niet gezien konden worden met de vorige generatie telescopen.

Dit werk begon, in hoofdstuk 1, met de verwerking van een enkele LOFAR observatie, met als doel te bepalen of de gepolariseerde straling waargenomen kon worden. Dit waargenomen veld was gecentreerd op het nabije sterrenstelsel IC342, maar het doel van de waarneming was de gepolariseerde straling en Faradaydraaiing binnen ons eigen sterrenstelsel meten. Het is mij gelukt om heldere gepolariseerde radiostraling te meten en kon twee duidelijke gepolariseerde-stralingsgebieden onderscheiden met verschillende Faradaydraaiing. Deze stralingsgebieden hadden kleine verschillen in hun Faradaydraaiing die niet met bij een hogere frequentie van elkaar onderscheiden hadden kunnen worden: hieruit blijkt duidelijk het nut van observaties op deze lage frequenties. De twee gebieden corresponderen duidelijk met twee wolken neutraal gas waarvan het bestaan in het lokale ISM bekend was. Hierdoor konden we meer informatie over de stralingsgebieden afleiden, zoals de afstand en de bron van de polarisatie, en konden we de parameters van het magneetveld verder inperken.

Nauwkeurige calibratie is essentieel voor betrouwbare polarisatiemetingen. In hoofdstuk 2 heb ik de software getest voor de calibratie en het corrigeren van de invloed van de ionosfeer van de Aarde op de polarisatie. Deze ionosfeer is een laag plasma in de hoge regionen van de atmosfeer. Deze correctie is nodig om zeker te zijn dat de Faradaydraaiing die door deze ionosfeer wordt veroorzaakt onze metingen niet beïnvloedt. Ik heb van twee onafhankelijke bronnen data ontvangen over de toestand van de ionosfeer. Beide heb ik gebruikt om de nodige correctie te berekenen, dit was belangrijk om te bepalen welke van de twee correcties effectiever zou zijn en hoe nauwkeurig de software was in het voorspellen van variaties in de correcties over een periode van een paar uur. Deze tests waren essentieel voor het bepalen van kwaliteit van de calibratie en de resulterende metingen, zoals ze gebruikt worden in de resterende hoofdstukken.

Na de succesvolle resultaten van de eerste observatie was de volgende stap het uitbreiden van ons observatiegebied. De LOFAR Two-meter Sky Survey, LOTSS, is een project dat de gehele noordelijke hemel in kaart gaat brengen met behulp van LOFAR. Ik heb een dataverwerkingsprogramma ontwikkeld voor de LOTSS data die de dataverwerking realiseert voor een polarisatieanalyse. Dit programma is gebruikt om 60 velden in de LOTSS te verwerken. De resultaten hiervan zijn te vinden in hoofdstukken 3 en 4.

Hoofdstuk 3 richt zich op de analyse van heldere, extra-galactische, gepolariseerde radiobronnen. Dit zijn objecten die ver weg staan, zoals sterrenstelsels die helder schijnen in radiostraling en gepolariseerde radiostraling produceren. Om twee redenen zijn deze objecten interessant: ten eerste kan de Faradaydraaiing van hun straling gebruikt worden om magneetvelden in onze Melkweg te bestuderen; ten tweede kan de polarisatie ons ook informatie geven over de eigenschappen van de magneetvelden in deze objecten, waardoor we deze kunnen onderzoeken. De polarisatie-eigenschappen van deze bronnen zijn nog niet goed bestudeerd op de LOFAR-frequenties, met maar een handvol bestudeerde objecten is er niet genoeg data om een fatsoenlijke statistische analyse te doen. Uit de LOTSS data kon ik 102 extra-galactische gepolariseerde radiobronnen halen, plus een gepolariseerde pulsar (die niet extra-galactisch is). De meeste van deze bronnen zijn reeds waargenomen op hogere frequenties, maar dit was de eerste meting van hun polarisatie op lage frequenties. Mijn metingen zijn over het algemeen consistent met data op hogere frequenties, maar laten wat verschillen zien die interessante eigenschappen van de magneetvelden suggereren. Meer analysewerk is nodig om deze verschillen te interpreteren en de aard van de bronnen te bepalen. Een groot deel van dit werk op de LOTSS data was ook om verschillende meetmethoden voor polarisatie te testen, met als doel de geschreven software geschikt te maken voor de analyse van polarisatie van toekomstige LOTSS data.

Hoofdstuk 4 richt zich op de diffuse gepolariseerde straling van onze eigen Melkweg, waarvoor de analysetechnieken uit hoofdstuk 1 gebruikt worden op de LOTSS data. Zoals bij het IC342 gebied vind ik hier ook gepolariseerde straling vanuit onze eigen Melkweg, rijk in verschillende structuren en gedragingen (zoals te zien is op de omslag van dit proefschrift). Veel van deze structuren zijn groter dan ooit gezien, meer dan 15 graden in lengte (ter referentie, het handvat van sterrenbeeld 'de Steelpan', beter bekend als 'De Grote Beer' is ruwweg 15 graden groot), en konden niet gezien worden in de afzonderlijke observaties die een kleiner oppervlak aan de hemel besloegen. In het bijzonder heb ik twee zeer lange, rechte gebieden van gepolariseerde straling gevonden met een gladde gradiënt in de Faradaydraaiing. Het bestaan van dit soort gebieden is erg interessant, deze kunnen namelijk niet gemaakt worden door magneetvelden die heel turbulent en chaotisch zijn. Het magneetveld dat hiervoor verantwoordelijk is, moet net zo glad zijn als de gradiënt die we observeren. Ik heb de gevonden polarisatiekenmerken vergeleken met andere aspecten van het ISM en vond hierbij een interessant verband: een van de rechte gladde gradiënten lijkt overeen te komen met de rand van een wolk van neutraal waterstofgas. Deze twee overlappen niet, maar de rand van de waterstofwolk komt goed overeen met de rand van het polarisatiegebied. Deze waterstofwolk moet dus een invloed uitoefenen op de eigenschappen van de Faradaydraaiing in deze regio. Dit laat wederom zien dat het met dit soort data mogelijk is om kenmerken van de polarisatiedata te koppelen aan processen in het ISM.

Samenvattend heeft dit werk laten zien dat dit soort analyse van LOFAR data een uitstekende

bron is voor informatie over magneetvelden in het lokale interstellaire medium. Het LOTSS project zal uiteindelijk de hele noordelijke hemel waarnemen (het werk in dit proefschrift beslaat ongeveer 3% van dat gebied), dus er bestaat de mogelijkheid om het hier gepresenteerde werk met nieuwe observaties uit te breiden. Zo kan uiteindelijk een gedetailleerde kaart gemaakt worden voor de polarisatie op lage frequenties voor de hele noordelijke hemel. Dit werk heeft ook laten zien hoe de lage-frequentiedata gekoppeld kan worden aan andere metingen van de structuur van het ISM, waardoor we beter gaan begrijpen hoe het magneetveld is verbonden aan zijn omgeving.

Curriculum vitæ

Cameron was born in Lethbridge, Alberta, Canada, but grew up near Barrhead, Alberta. He completed his highschool education by correspondence, graduating from the Alberta Distance Learning Centre in 2005. He attended the University of Calgary from 2005 to 2012, and graduated with a Bachelor of Science (Honors) in Astrophysics and Physics, First Class in 2010 and a Master of Science in Astrophysics in 2012. During his time at the UofC he was heavily involved in several volunteer tutoring programs and in astronomy public outreach at the Rothney Astrophysical Observatory. His Bachelor and Master thesis work was done with Dr. Jo-Anne Brown, and involved processing of VLA observations, development of Galactic magnetic field models, and a meta-analysis of observations of magnetic fields in nearby galaxies. Both projects led to publications.

In January 2013 Cameron moved to Nijmegen to begin his PhD with Dr. Marijke Haverkorn. His PhD work concentrated on the use of polarization data from the Low Frequency Array as a tool for probing magnetism in the local interstellar medium. During his time in Nijmegen he served as teaching assistant for the interstellar medium, cosmic magnetism, and programing for scientists I and II courses, enabled access for Radboud PhD students to the 40 cm robotic telescope at the Rothney Astrophysical Observatory in Canada, took part in many outreach activities including the development of a 1-day radio astronomy exercise for highschool students, participated in several LOFAR 'Busy Day' meetings, and served as the Astronomy department PhD student representative. He claims partial credit for the softening of the 'five paper rule' and for starting the idea of the Friday hospital lunch.

Since April 2017 Cameron has moved back to Canada and is continuing to search for a post-doctoral research position.

List of Publications

Refereed Publications

- **C.L. Van Eck**, M. Haverkorn, M.I.R. Alves, R. Beck, P.N. Best, E. Carretti, K.T. Chyży, J.S. Farnes, K. Ferrière, G. Heald, C. Horellou, M. Iacobelli, V. Jelić, D.D. Mulcahy, I.M. Polderman, W. Reich, H.J.A. Röttgering, D.H.F.M. Schnitzeler, C. Sobey, V. Vacca, J. Vink, G.J. White. *"Polarized point sources in the LOFAR Two-meter Sky Survey"*. in prep.

- **C.L. Van Eck**, M. Haverkorn, et al. *"Diffuse polarized emission in the LOFAR Two-meter Sky Survey"*. in prep.

- **C.L. Van Eck**, M. Haverkorn, M.I.R. Alves, R. Beck, A.G. de Bruyn, T. Enßlin, J.S. Farnes, K. Ferrière, G. Heald, C. Horellou, A. Horneffer, M. Iacobelli, V. Jelić, I. Martí-Vidal, D.D. Mulcahy, W. Reich, H.J.A. Röttgering, A.M.M Scaife, D.H.F.M. Schnitzeler, C. Sobey, S.S. Sridhar. *"Faraday Tomography of the Local Interstellar Medium with LOFAR: Galactic Foregrounds Towards IC342"*. Astronomy & Astrophysics, Volume 597, id.A98, 17 pp. published January 2017.

- J. S. Farnes, G. Heald, H. Junklewitz, D. D. Mulcahy, M. Haverkorn, **C. L. Van Eck**, C. Riseley, M. Brentjens, C. Horellou, V. Vacca, D. I. Jones, A. Horneffer, R. Paladino. *"Source Finding in Linear Polarization for LOFAR, and SKA Predecessor Surveys, using Faraday Moments"*. Submitted to Monthly Notices of the Astronomical Society, September 14, 2016, submission number MN-16-3205-MJ.

- Coppejans, D.L., Koerding, E.G., Knigge, C., Pretorius, M.L., Woudt, P.A., Groot, P.J., **Van Eck, C.L.**, Drake, A.J. *"Statistical Properties of Dwarf Novae-type Cataclysmic Variables: The Outburst Catalogue"*. 16 pages. Monthly Notices of the Royal Astronomical Society, Volume 456 Issue 4, p 4441-4454. published January 2016.

- **Van Eck, C. L.**, Brown, J. C., Shukurov, A., Fletcher, A. *"Magnetic Fields in a Sample of Nearby Spiral Galaxies"* Astrophysical Journal, Volume 799, Issue 1, article 35, 19 pp. published January 2015.

- Mao, S. A., McClure-Griffiths, N. M., Gaensler, B. M., Brown, J. C., **van Eck, C. L.**, Haverkorn, M., Kronberg, P. P., Stil, J. M., Shukurov, A., and Taylor, A. R. *"New Constraints on the Galactic Halo Magnetic Field Using Rotation Measures of Extragalactic Sources toward the Outer Galaxy"*. Astrophysical Journal, Volume 755, Issue 1, article 21, 15 pp. published July 2012.

- Oppermann, N., Junklewitz, H., Robbers, G., Bell, M. R., Enğlin, T. A., Bonafede, A., Braun, R., Brown, J. C., Clarke, T. E., Feain, I. J., Gaensler, B. M., Hammond, A., Harvey-Smith, L., Heald, G., Johnston-Hollitt, M., Klein, U., Kronberg, P. P., Mao, S. A., McClure-Griffiths, N. M., O'Sullivan, S. P., Pratley, L., Robishaw, T., Roy, S., Schnitzeler, D. H. F. M., Sotomayor-Beltran, C., Stevens, J., Stil, J. M., Sunstrum, C., Tanna, A., Taylor, A. R., and **Van Eck, C. L**. *"An improved map of the Galactic Faraday sky"*. Astronomy & Astrophysics, Volume 542, article A93, 14 pp. published June 2012.

- **Van Eck, C. L.**, Brown, J. C., Stil, J. M., Rae, K., Mao, S. A., Gaensler, B. M., Shukurov, A., Taylor, A. R., Haverkorn, M., Kronberg, P. P., McClure-Griffiths, N. M., *"Modeling The Magnetic Field In The Galactic Disk Using New Rotation Measure Observations From The Very Large Array"*. Astrophysical Journal, Volume 728 Number 2, article 97, 14 pp. published January 2011.

- Dehghany, M., Afshari, M., Abusara, Z., **Van Eck, C.**, & Moazzen-Ahmadi, N., *"Isotope effects in the infrared spectra of the polar and nonpolar isomers of N2O dimer"*. Journal of Molecular Spectroscopy, Volume 247, Issue 2, p. 123-127. Published February 2007.

Proceedings

- **Cameron Van Eck** and Jo-Anne Brown *"Modeling the Galactic Magnetic Field using Rotation Measure Observations in the Galactic Disk from the CGPS, SGPS, and the VLA"*, The Dynamic Interstellar Medium: a Celebration of the Canadian Galactic Plane Survey, eds. R. Kothes, T.L. Landecker, and A.G. Willis, ASP Conference series, vol 438, p. 236, 7 pp. published Dec 2010.

Acknowledgments

I have no doubt that I would not have made it this far without the help and support of many people. I'm happy to have this chance to thank some of those people here.

Top billing of course goes to Marijke. I couldn't have asked for a better supervisor: patient when things were going slowly, encouraging when things were going badly, persistent when I was slacking off, and engaged when I was struggling with something new. I honestly don't think I could have finished this PhD with a different supervisor.

All of my office mates have had a lot of impact on me, and deserve individual thanks. David, for keeping an eye on me when we travelled to (other) strange countries. Sally, for setting the tone that our office was infamous for. Andrei, for all the statistics jokes and whiteboard arguments. Payaswini, for being a perpetual ray of sunshine (critical for surviving Dutch winters!). Deanne, for too much to list. You and I have very similar neurotic stresses; helping you helped me. Rocco (who spent enough time in our office to be an office mate, despite not having a desk), for being someone to vent with. Michael, for all our radio astronomy and CASA discussions. And Irene, for being a fantastic kōhai; I'm always happiest when I get the chance to help someone.

I couldn't have done this work without the firm grounding in radio astronomy and polarization that I got in Calgary. Credit for that goes to Jo-Anne, for drilling the fundamentals firmly into my head. Also, thanks to Jeroen, for always treating me like a colleague instead of a student, even if it meant a lot of 'drinking from a firehose' knowledge transfer.

I also want to thank all the members of the LOFAR Magnetism Key Science Project, for being an energetic and welcoming group of colleagues. I hope that circumstances allow me to work with you again in the future. Special thanks to Jamie, for our very satisfying Faraday rotation discussions.

The positive social environment of the department was also a great help in keeping me balanced. A lot of thanks go to my fellow students who helped me indulge my nerdy side: Jan, Christiaan, Thomas B., Jordy, Emilio, and Ellert. Not only did I get to realize my dream of commanding a U-boat, but I got to own one as well. Thanks as well to Marja, Esther, Cisca, Helma, and Monique, for helping me navigate university and Dutch bureaucracy. Thank you as well to Laura, for organizing hospital lunches and bowling.

On the more technical side of things, I owe a lot to Pim S. and Ben Polman, for their dedicated support of the Coma cluster, and Martin, for his work on the incredibly easy-to-use thesis template. This work could not have been completed without the use of many public software packages, which I'm trying to give proper credit to in all my future papers beginning with Chapter 2. Thank you to Gieljan for your indirect assistance in translation, as well as for the D&D tips.

And finally, my parents, for a lot of things, not least of which for being an island of sanity I could escape to as needed.